Visual Topography and Perceptual Learning in the Primate Visual System

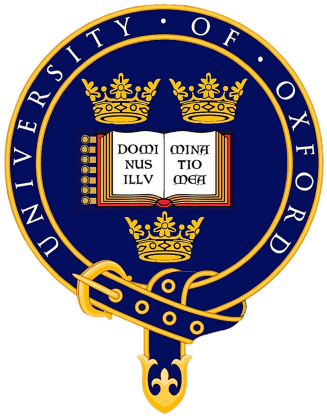

Kimmy Tang-Wright

Worcester College

University of Oxford

A thesis submitted for the degree of

Doctor of Philosophy in Physiology, Anatomy and Genetics

Trinity 2016

Acknowledgements

First and foremost, I would like to express my deepest gratitude to my supervisors Prof. Kristine Krug and Prof. Andrew Parker for their invaluable guidance, motivation and academic inspiration. I am likewise extremely indebted to Dr. Jackson Smith who always found the time and patience to talk with me through any questions or difficulties I encountered. His positive attitude towards science and his willingness to pass on his knowledge was truly inspiring. I have learnt so much from these academic figures, and their influence has made all the difference to my work.

I would also like to thank all the fantastic people I have known throughout my years at Oxford, Richard Edmondson, Daniel O'Connor, Imogen Large, Sophie Hall, Nick Talbot, Yatu Yoga, Hugh Smith, Paul Davies, Matt Smith and Jamie Rolfe. They have all had a special influence on me, and I am forever grateful for their support and friendship.

Finally, I would also like to thank my family who have been with me throughout my entire academic journey and whose unwavering support and kindness are the most impressive things I know of.

Abstract

The primate visual system is organised and wired in a topological manner. From the eye well into extrastriate visual cortex, a preserved spatial representation of the visual world is maintained across many levels of processing. Diffusion-weighted imaging (DWI), together with probabilistic tractography, is a non-invasive technique for mapping connectivity within the brain. In this thesis I probed the sensitivity and accuracy of DWI and probabilistic tractography by quantifying its capacity to detect topological connectivity in the *post mortem* macaque brain, between the lateral geniculate nucleus (LGN) and primary visual cortex (V1). The results were validated against electrophysiological and histological data from previous studies. Using the methodology developed in this thesis, it was possible to segment the LGN reliably into distinct subregions based on its structural connectivity to different parts of the visual field represented in V1. Quantitative differences in connectivity from magno- and parvocellular subcomponents of the LGN to different parts of V1 could be replicated with this method in *post mortem* brains. The topological corticocortical connectivity between extrastriate visual area V5/MT and V1 could also be mapped in the *post mortem* macaque. *In vivo* DWI scans previously obtained from the same brains have lower resolution and signal-to-noise because of the shorter scan times. Nevertheless, in many cases, these yielded topological maps similar to the *post mortem* maps. These results indicate that the preserved topology of connection between LGN to V1, and V5/MT to V1, can be revealed using non-invasive measures of diffusion-weighted imaging and tractography *in vivo*. In a preliminary investigation using Human Connectome data obtained *in vivo,* I was not able to segment the retinotopic map in LGN based on connections to V1. This may be because information about the topological connectivity is not carried in the much lower resolution human diffusion data, or because of other methodological limitations. I also investigated the mechanisms of perceptual learning by developing a novel task-irrelevant perceptual learning paradigm designed to adapt neuronal elements early on in visual processing in a certain region of the visual field. There is evidence, although not clear-cut, to suggest that the paradigm elicits task-irrelevant perceptual learning, but that these effects only emerge when practice-related effects are accounted for. When orientation and location specific effects on perceptual performance are examined, the largest improvement occurs at the trained location,

however, there is also significant improvement at one other 'untrained' location, and there is also a significant improvement in performance for a control group that did not receive any training at any location. The work highlights inherent difficulties in investigating perceptual learning, which relate to the fact that learning likely takes place at both lower and higher levels of processing, however, the paradigm provides a good starting point for comprehensively investigating the complex mechanisms underlying perceptual learning.

Contents

Chapter 1

Introduction

1.1 The primate visual system

A principal feature of the primate visual system is that it is organized topographically, with a coherent spatial representation of the visual field maintained throughout many stages of processing along the visual pathway. Visual information from the left visual hemifield falls onto the nasal retina of the left eye and the temporal retina of the right eye, and following a crossing over of the nasal fibres at the optic chiasm, information from the left half of the visual world becomes represented in the right half of the brain (Fig. 1.1). Ganglion cell axons from the retina terminate in the lateral geniculate nucleus (LGN) in an ordered way, such that neighbouring regions of visual space are represented by neighbouring neurons within each lamina of the LGN. This retinotopic organization is furthermore preserved in the topographic order of the LGN projection to the primary visual cortex (V1). Within V1, the fovea is represented in the posterior part of the cortex, while more peripheral visual field regions are represented in progressively more anterior regions. The upper visual field is mapped below the calcarine sulcus, and the lower visual field above it. Visual field maps in which the spatial representation of image features is preserved are prevalent and repeated many times over within the cortex (Wandell et al., 2007), and likely reflect the

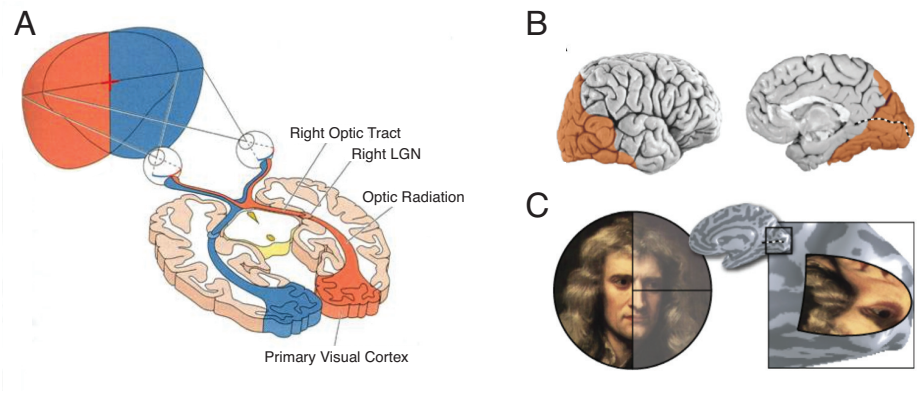

Figure 1.1: **(A)** Illustration of the primate visual system. The optic nerve leads from the eye to the optic chiasm. The nasal fibres cross at the optic chiasm, and the optic tract proceeds from the optic chiasm to the lateral geniculate nucleus (LGN). The optic radiation leads from the LGN to primary visual cortex (V1). The right half of the brain receives information from the left visual field. The projections from the retinal ganglion cells are retinotopic and registered so that a visual field map is preserved in the LGN. **(B)** The human visual cortex, shown in orange, occupies approximately 20% of the cerebral cortex and is located in the occipital lobe and the posterior parts of the parietal and temporal lobes. Primary visual cortex (V1) is located in and around the calcarine sulcus (dotted line). **(C)** The visual field map in V1. The image on the left is a portrait of Sir Isaac Newton, and the image on the right illustrates how the visual field (left) is transformed and represented on the V1 cortical surface (right) using a mathematical description proposed by Schwartz (1977). The left visual field stimulates V1 in the right hemisphere; the image representation is inverted and the centre of the visual field, near the eye, is greatly expanded (cortical magnification). Adapted from Wandell et al. (2007, Fig. 1).

critical importance of the spatial arrangement of visual scenes. Visual field maps have been identified in V1 (Fishman, 1997; Holmes 1918), V2 (Talbot & Marshall, 1941), V4, V5/MT (Allman & Kaas, 1971), lateral occipital areas (Larsson & Heeger, 2006), and posterior parietal regions (Press et al., 2001; Schluppeck et al., 2005; Sereno et al., 2001).

As Figure 1.1B&C illustrates, the scale within the visual field maps can vary considerably, with certain visual field regions disproportionately represented in terms of millimetres of cortex devoted to representing the given visual region. Analogous to the way the fingers and mouth representations are overrepresented in the somatosensory topographic map of the post central gyrus, there is a marked overemphasis on central vision in many of the

topographic representations in the visual system. This emphasis on the central visual field representation in the striate cortex is called the cortical magnification factor (M), and is defined as the linear extent of cortex corresponding to 1° of visual angle (Daniel & Whitteridge, 1961). In the macaque monkey, M varies from between 9 – 13 mm/deg at the fovea, to about 0.05 mm/deg at 80° eccentricity (Daniel & Whitteridge, 1961; Dow et al., 1981; Azzopardi & Cowey, 1996), with similar values of cortical magnification reported for humans (Cowey & Rolls, 1974; Cowey & Rolls, 1975). In teams of area, this means that the fovea, which samples the central 1° radius of the visual field, is represented by about 0.01 – 0.025% of the retinal area, and approximately 8% of the striate cortex (Talbot & Marshall, 1941; Daniel & Whitteridge, 1961; Cowey, 1964).

The emphasis on central vision is evident within the retina itself, where there are large regional differences in the density of retinal ganglion cells. Ganglion cell density determines visual sensitivity, and it is therefore not surprising that visual acuity is best at the fovea and deteriorates markedly at the periphery. It was previously a matter of some debate as to whether the overrepresentation of central vision in the LGN and V1 was merely a recapitulation of the uneven ganglion cell distribution in the retina (peripheral scaling hypothesis: Hubel & Wiesel, 1974; Schein & de Monasterio, 1987; Malpeli et al., 1996), or whether the cortical magnification factor (M) actually exceeds the amount predicted by ganglion cell densities, implying that peripheral scaling is not a general principle of cortical organization (expansion hypothesis: Rolls & Cowey, 1970; Connolly & Van Essen, 1984; Van Essen, Newsome & Maunsell, 1984; Azzopardi & Cowey, 1993). The latter view has been extensively supported by evidence that some aspects of vision, such as vernier acuity, are far better at the fovea than would be predicted solely on the basis of ganglion cell density (Westheimer, 1975). The resolution at which subjects can discern a disalignment between two line segments exceeds that predicted by the spacing of individual photoreceptors. The expansion view is also supported by direct anatomical evidence from retrograde, trans-neuronal tracer studies showing that there is more cortex per ganglion cell near the fovea than in the peripheral retina (Azzopardi & Cowey, 1993; Azzopardi &

Cowey, 1996). Furthermore, the expansion of the central representation was shown to occur in two steps - between the retina and LGN, and between the LGN and visual cortex. The purpose of discussing these studies here is to illustrate the importance of having accurate descriptions of how the visual field (or any sensory field) is represented in different cortical and subcortical areas. Such information allows one to determine what transformations in the sensory representation take place along the sensory pathway (Van Essen et al., 1984). The mapping of topography in sensory structures also allows us to make important cross-species comparisons - a point of particular interest given that psychophysical evidence can be more readily obtained in humans than in primates, but that detailed anatomical investigations in humans are far more challenging than they are in primates.

1.2 Mapping topography

The connectivity and retinotopy of cortical and subcortical sensory structures is usually defined in non-human primates (NHPs) using histological (Zeki, 1976; Connolly & Van Essen, 1984;) and electrophysiological techniques (Gur et al., 1997; Malpeli & Baker, 1975; Malpeli et al., 1996; Merigan & Maunsell, 1990; Nealey & Maunsell, 1994). However, these 'gold standard' techniques have their disadvantages. For example, histological techniques are unsuitable for *in vivo* or intact brain preparations, while *in vivo* electrophysiology is both challenging and invasive. Furthermore, these techniques are often unable to visualise the gross anatomical trajectories of sensory white-matter pathways.

Diffusion-weighted imaging (DWI) is an MRI-based technique that allows the non-invasive estimation of white-matter pathways for *in vivo* or intact brain preparations (Le Bihan et al., 1986; Basser et al., 1994; Mori et al., 1999; Jones et al., 1999). Tractography is the post-imaging reconstruction of fibre pathways from DWI data and can be used to produce a range of information about brain anatomy and connectivity, including the visualization of white-matter pathway trajectories (Catani & Thiebaut de Schotten, 2008; Glasser &

Rilling, 2008) and the subdivision (parcellation/segmentation) of grey mater regions based on tractography-derived connectivity profiles (Behrens et al., 2003; Johansen-Berg et al., 2004; Rushworth et al., 2006; Mars et al., 2011). The process of DWI and the tractographic reconstruction of fibre pathways from DWI data will be elaborated on in the following chapters. The point being made here is that DWI represents an important and useful tool for establishing connectivity between regions. Since a key principle of systems neuroscience is that that structural connectivity of a region is linked to its function, the function and topographic organization of regions can be inferred from its connections to another area using DWI information. Previously, tractography has been used to identify functionally meaningful subdivisions of the thalamic grey matter from thalamocortical connections (Behrens et al., 2003a). The questions then become, what is the upper limit of DWI in predicting topography? Is DWI capable of detecting topographic maps within areas? Is it achievable in small subcortical regions? How strong or large does the white-matter pathway have to be? Is it possible with *in vivo* data? If so, how much is the accuracy dependent on the resolution and the signal-to-noise ratio (SNR) of the DWI data? These are the questions the chapters of this thesis will address.

1.3 Aim and scope of thesis

Tractography is an indirect measure of connectivity and therefore various methodological confounds can introduce noise and/or bias (Jbabdi & Johansen-Berg, 2011; Jones et al., 2013; Van Essen et al., 2014). The first part of this thesis is concerned with developing a sound methodology and appropriate tractography parameters suited for detecting realistic connectivity. The investigation first looks at whether the visual topological pattern of connections in the Rhesus macaque (*Macaca mulatta*) between the LGN and V1 can be detected using DWI and probabilistic tractography. This connection is suitable for testing as the optic radiation is large, and both regions have a well-known retinotopic organisation. Since brain structure is linked to function, regions in the LGN and V1 with the same

visual field representation should be preferentially connected. Such a mapping has not been previously achieved non-invasively with DWI due to its inherent limitations (Basser et al., 2000, Jones, 2010, Jones et al., 2013). These limitations relate to the fact that DWI is an indirect measure of axonal connectivity, and therefore poor SNR and voxel resolution increase its inability to resolve aspects of axonal pathways, such as crossing-fibres and sharply-turning narrow tracts, and increase the presence of partial volume effects. Partial volume effects occur when a voxel volume comprises a number of different tissue substances, or different fibre orientations, meaning the voxel anisotropy value represents some average of these properties. Low SNR and voxels resolutions therefore mean that the DWI acquired data carry less of the ground-truth data. These limitations are first overcome here by using DWI obtained from *post mortem* preparations with a high resolution and high signal-to-noise ratio (Dyrby et al., 2011). The use of *post mortem* macaque data is critical for the qualitative and quantitative validation of tractography against the gold-standard data from electrophysiological and histological tracer studies of the macaque LGN and visual cortex. Extending this quantitative validation further, this thesis goes on to investigate whether quantifiable predictions of connectivity can be made in order to compare the ratio of magno- and parvocellular LGN subcomponent connectivity across different visual field representations in V1. The following chapters investigate whether DWI and probabilistic tractography are able to uncover topographic connections across multiple brains, for different seed regions (LGN and V5/MT), different types of topographic map (eccentricity and elevation), and for *in vivo* macaque and human datasets. Probing the capabilities of DWI and pushing it to its limits is important for fully understanding how the technology may be best utilized in future. Better maps of the brain's areas and their connectivity are crucial in furthering our understanding of the healthy brain, and for improving our knowledge and treatment of neuropsychological and psychiatric disorders.

As previously described, a key principle of neuroscience is that human perception is determined by the properties of brain circuitry. Although not directly related to the work on diffusion imaging, the last part of this thesis is concerned with the next logical step of map-

ping visual field representations, which is in investigating human perception through psychophysical studies. In particular, the thesis investigates the specificity of task-irrelevant perceptual learning (TIPL) to location and orientation, in order to establish a biological basis for the phenomenon, and to what extent it is similar to, or differs from, task-relevant perceptual learning. Ultimately, these two strands of investigation, DWI and perceptual psychophysics, could be used in the future, in concert, to explore the precise within-area locus of neural changes associated with perceptual learning. For example, if a given visual field location can be reliably shown to be represented in a given part of LGN, or a given part of the optic radiation, subsequent MR-related studies can begin to look at the neuronal or axonal changes that occur in response to learning that is specific to that visual field location. While the LGN has traditionally been viewed simply as a relay station for visual information, only 5-10% of the input to the LGN derives from the retina. The rest are modulatory inputs and derived from local inhibitory inputs, descending inputs from layer 6 of the visual cortex, and ascending inputs from the brainstem (Steriade et al., 1997; Chen & Regehr, 2003; Liu et al., 2015). These modulatory inputs control many aspects of retinogeniculate transmission, such as the response mode of relay cells (burst or tonic), which relates to attentional demands of the system. Thus, understanding the structural and functional organization of the LGN has important implications in understanding factors that influence perception. Indeed, the same concept of combining topographic map knowledge with psychophysics could just as easily be translated to explore the locus of neuronal changes for any given sensory region with a topographic map.

Chapter 2

Methods: Diffusion-weighted imaging and probabilistic tractography

2.1 Introduction

Diffusion-weighted imaging (DWI) is an MRI-based technique that allows the non-invasive estimation of brain connectivity for *in vivo* or intact brain preparations (Le Bihan et al., 1986; Basser et al., 1994; Mori et al., 1999; Jones et al., 1999). DWI weights different parts of the brain according to how water diffuses within the brain. By taking advantage of the preferential diffusion of water-molecules along axons (the axonal membrane inhibits perpendicular movement), an estimate of white matter fibre orientation can be achieved (LeBihan et al., 1986; Basser et al., 1994; Johansen-Berg & Rushworth, 2009). Quantifying the magnitude and direction of water molecule diffusion allows fibre-tracking algorithms, such as probabilistic tractography (Behrens et al., 2003), to use this information to reproduce visualisations of 3D fibre tracts (Basser et al., 2000), as well as measures of the probability of connectivity between regions.

This chapter outlines the data acquisition and processing stages involved in the analysis of

the DWI datasets. DWI analysis is still in its relative infancy when compared with the more established histological tract-tracing techniques that are considered the 'gold standard' for estimating white matter pathways in the brain. As such, there is considerable variation in how DWI data are processed and how tractography is carried out. This thesis develops and utilizes several novel approaches to diffusion imaging analysis, such as the normalization of biases in tractography, use of white-matter targets, quantitative comparison of predicted maps to atlases, and the statistical analysis of the distance between the centres of gravity for clusters of voxels classified through tractography. The diffusion imaging data analysed in this thesis take three different forms: *post mortem* macaque DWI, *in vivo* macaque DWI, and *in vivo* human DWI data. The data collection and analysis procedures involved for *post mortem* and *in vivo* macaque datasets will be described first, followed by those for *in vivo* human datasets wherever the procedures differ from those already described.

The *post mortem* and *in vivo* macaque experiments described in this chapter were carried out in collaboration with Dr. Tim Dyrby (Danish Research Centre for Magnetic Resonance – DRCMR), Dr. Kristine Krug (Oxford), Dr. Bashir Ahmed (Oxford), and Dr. Jackson Smith (Oxford). Dr. Ahmed and Dr. Krug performed the *post mortem* brain removal and preparation at the Biomedical Sciences Building, Oxford (Ahmed et al., 2012. The preparations were transported to Tim Dyrby's lab (DRCMR, Copenhagen, Denmark), by Dr. Ahmed, Dr. Smith, Dr. Krug, and myself, for magnetic resonance (MR) scanning and data acquisition using the protocols Dr. Dyrby had developed (Dyrby et al., 2011). Dr. Kristine Krug, and Dr. Bashir Ahmed performed the *in vivo* macaque scanning procedures. *In vivo* human data were provided by the Human Connectome Project (HCP), WU-Minn Consortium (http://www.humanconnectome.org/).

2.2 Methods

2.2.1 *Post mortem* and *in vivo* macaque

2.2.1.1 Animals

Six adult macaques (*Macaca mulatta*) yielding 12 hemispheres were included in this study – three females (M124, M128, and M129) and three males (M126, M127, and M130). Mean age at sacrifice was 7.8 years (range = 3.9-12.4 years, standard deviation [SD] ± 4.0 years, weight range = 5.20-14.07 kg). All animal procedures were carried out and approved under authority of personal and project licenses in accordance with the UK Scientific Procedures (Animals) Act (1986), and the European Council Directive of 22 September 2010 (Directive 2010/63/EU).

2.2.1.2 Tissue fixation and storage for *post mortem* scanning

Animals were sedated with an intramuscular injection of ketamine (20mg/kg), given an intravenous injection of Euthatal (pentobarbitone) (65mg/kg/hr) and perfusion-fixated transcardially using phosphate-buffered saline (PBS), followed by 4% paraformaldehyde (PFA) in 0.1 mol/l PBS (pH 7.4). The brains were removed and stored in 4% PFA at 4°C. Preparation for *post mortem* imaging followed the imaging setup described in Dyrby et al. (2011). In brief, one week prior to scanning the PFA was washed out with PBS to increase the T2-weighted signal. Free, unreacted aldehyde fixative solution alters the T2 relaxation properties of tissues and reduces the SNR (Shepherd et al., 2005). Before scanning, the brain was placed in a plastic bag with minimal PBS and stabilised to room temperature for at least 6 hours in order to minimize heat conduction while scanning. On placement in the scanner, the brain was mechanically stabilised using soft foam wrapped around the brain to fix its position within the scanner. Air-conditioned flow around the tissue was used to stabilise temperature during scanning. Time-varying artefacts can occur as a result of

scanner instabilities such as temporal drifts in the main magnetic field (b0 drift), heating up of the gradient coils and other scanner hardware, and heat conduction from the tissue and scanner environment (Dyrby et al., 2011). To minimise these short-term instabilities in diffusion MRI data, a four-hour dummy scan was acquired prior to the actual diffusion MRI dataset acquisition.

2.2.1.3 MR data acquisition

Post mortem data were acquired with an experimental 4.7T Agilent pre-clinical MR scanner with a maximum gradient strength of 600 mT/m. Diffusion-weighted imaging (DWI) was collected using a quadrature volume primate head RF coil and a 2D single spin-echo sequence with single-line read-out. The DWI dataset included three b = 0 s/mm^2 and single shell with 61 gradient directions (Jones, 2004) using b = 4310 s/mm^2 (Gradient strength, G = 100 mT/m, δ = 27 ms and Δ = 33.5 ms). Whole-brain DWI volumes were collected at 0.5 mm x 0.5 mm x 0.5 mm resolution (FOV = 64 mm x 128 mm, image matrix = 128 x 256) as 128 interleaved axial slices using TR = 5100 ms and TE = 45 ms. Scan time for each DWI dataset was 12 hours and was repeated four times, giving an approximate total scan time of 48 hours for each macaque brain (excluding the dummy scan).

In vivo data were acquired from five of the same brains used in the *post mortem* scanning (M124, M126, M127, M128 and M129). Animals were induced using intramuscular injections of ketamine (10 mg/kg), xylazine (0.125-0.25 mg/kg) and midazolam (0.1 mg/kg). Injections of atropine (0.05 mg/kg, i.m.) and meloxicam (0.2 mg/kg, i.v) were given. Local anaesthetics (5% lidocaine/prilocaine cream on the skin and, in some experiments, 2.5% bupivacaine injected subcutaneously around the ears to prevent stimulation by the stereotactic head-frame) were also administered at least 15 minutes before scanning as advised. During the scans, anaesthesia was maintained using sevoflurane (2-3% by inhalation), and depth was assessed using continuous, automated monitoring of physiological parameters

(heart rate, blood oxygenation, blood pressure, expired CO_2, and core temperature). The animals were placed in an MRI-compatible stereotaxic frame and were usually maintained with intermittent positive pressure ventilation to ensure a constant respiration rate during the scanning session. Respiration rate, inspired-expired CO_2 and sevoflurane concentration were monitored using VitalMonitor (Vetronic Services Ltd.).

In vivo data were acquired with a 3T human clinical MRI scanner, using a four-channel phased-array coil (H. Kolster, Windmiller Kolster Scientific, Fresno, CA), and a twice-refocused spin-echo (TRSE) sequence. The second refocusing pulse in TRSE allows better image SNR at no cost in scanning efficiency or effectiveness (Reese et al., 2003). The DWI dataset included three b = 0 s/mm^2 and single shell with 61 gradient directions using b = 1000 s/mm^2. Whole-brain DWI volumes were collected at 1 mm x 1 mm x 1 mm resolution (FOV = 112 mm x 112 mm, image matrix 112 x 112) as 56 interleaved axial slices using TR = 10,000 ms and TE = 103 ms.

Each 61-direction, diffusion-weighted imaging (DWI) scan took 13 minutes, and was repeated 12 times in each animal for subsequent averaging to improve SNR. EPI images suffer from susceptibility-induced geometric distortions due to magnetic field inhomogeneities, particularly in basal brain regions. To minimise these distortions, the phase encode direction was reversed on each repetition scan (Right-Left and Left-Right reversal). This method exploits the fact that images with opposite polarities show opposite distortions (Andersson et al., 2003). In total, at least 12 DWI scan runs were collected on each animal. Compared to the *post mortem* data, *in vivo* scans had weaker signal strengths (b = 4310 s/mm^2 for *post mortem* vs b = 1000 s/mm^2 for *in vivo*), lower resolution (0.5 mm^3 for *post mortem* vs 1 mm^3 for *in vivo*), and contained physiological noise (Walker et al., 2011). Motion artefacts were reduced by placing the anaesthetised animals in a MRI compatible stereotaxic frame.

For each animal, five high-resolution (0.5 mm x 0.5 mm x 0.5 mm) T1-weighted structural images were also acquired using a 3D magnetisation-prepared rapid-acquisition gradient

echo (MPRAGE) sequence with the following parameters: 128 interleaved sagittal slices (no gap), 0.5 mm slice thickness, TR = 2500 ms, TE = 4 ms, TI = 1100 ms, flip angle = 7°, FOV = 128 mm x 128 mm, image matrix = 256 x 256. The total scan time for the structural and diffusion weighted protocols combined was approximately 4 hours.

2.2.1.4 *Post mortem* data pre-processing

Visual inspection of the acquired *post mortem* DWI dataset revealed no motion or other known *in vivo* related artefacts requiring retrospective correction. Therefore, the four repeat acquisitions were averaged for each brain. The average of all non-diffusion-weighted volumes (referred to as the 'b0 average' image) was used to provide an anatomical image to define masks and register results onto a standard atlas. This image was used alongside the average of all diffusion-weighted volumes (the 'b4K average' image) to define a tight, whole-brain binary mask that excluded areas outside the brain and large fluid-filled ventricles and sulci. Image intensity thresholds were separately chosen and applied to the b0 and b4K average images to remove brain tissue in the b0 image, and fluid-filled spaces in the b4k image. This is because the contrast in image intensities for brain tissue vs non-brain tissue is greatest in the b0 image, but fluid-filled spaces are more distinct in the b4k image. Together, masks can be created from each of these images and combined to keep tractography within brain tissue. The resulting brain mask was checked by eye and corrected by hand to fill in any gaps. Image processing and analysis were performed using tools developed at the Centre for Functional Magnetic Resonance Imaging of the Brain (FMRIB Centre, University of Oxford). These are incorporated into the FMRIB Software Library (FSL, FMRIB Software Library v3.1, FSLBet, FSLMaths, and FSLView; www.fmrib.ox.ac.uk/fsl; Woolrich et al., 2009; Smith et al., 2004; Jenkinson et al., 2012).

2.2.1.5 *In vivo* data pre-processing

Brain masks were also created for the *in vivo* diffusion-weighted images using a combination of thresholding the b0-averaged image, and subsequent manual corrections to fill in gaps in the mask. To reduce the distortions from magnetic field inhomogeneities, the two sets of DWI with opposite phase encoding polarity were combined using FSL's 'TopUp' tool (Andersson et al., 2003). Distortions from eddy currents in the gradient coils were reduced both through the use of a twice-refocused DWI sequence (Reese et al., 2003) and using the FSL eddy correction software. In a final step, diffusion-weighted images with the same gradient direction were averaged together, to improve the signal-to-noise ratio.

After pre-processing, four out of the five brains scanned had *in vivo* scans of sufficient image quality and signal strength to be used for tractography, summarised by measuring the average fractional anisotropy (FA) of the corpus callosum (excluded brain = 0.55 [SD ± 0.15]; included brains = 0.70 [0.13]). According to Tim Dyrby, the FA of the corpus callosum should be 0.6 or higher for datasets of this nature, and values lower than this indicate a substantial loss of SNR (personal communication, January 22, 2014). The excluded brain (M126) also had considerable signal dropout in the occipital lobe, which is another reason for its exclusion. In two brains (M127 and M128), linear registration (FLIRT, FSL) was successfully used to transform a set of DWI scans taken on one day onto the set from another. The two sets were then averaged together following registration to improve SNR for a total of 24 averaged repeats. The measured FA values of the corpus callosum for these brains were subsequently above 0.6.

2.2.1.6 Probabilistic tractography

Probabilistic tractography was performed on the diffusion-weighted images using the implementation in FSL (BedpostX and ProbtrackX2, Behrens et al., 2003a; Behrens et al., 2007). BedpostX stands for Bayesian Estimation of Diffusion Parameters Obtained using

Sampling Techniques, the X stands for modelling Crossing fibres. BedpostX is first run on the 4D diffusion imaging data to estimate fibre orientations. It uses Markov Chain - Monte Carlo (MCMC) sampling to build up distributions on diffusion parameters at each voxel, and uses the Ball & Sticks model for voxel-wise fitting of fibre orientation distributions (FOD). Using a Ball & Sticks model as opposed to a simple tensor model allows the modelling of multiple fibre orientations (rather than just one), and therefore importantly allows the modelling of crossing fibres within each voxel (Behrens et al., 2003b).

Probabilistic tractography is performed by sampling the fitted FODs (Probtrackx2 function, Behrens et al. 2003a, Behrens et al., 2003b; Behrens et al., 2007) to generate virtual processes, called *streamlines*, which propagate from voxels in a seed region, through white-matter pathways, to a target region. At each propagation step, the Probtrackx2 algorithm chooses randomly an orientation from the underlying distribution. When multiple fibre orientations exist in a voxel, it chooses the one that is most compatible with the incoming trajectory (Behrens et al., 2003b).

Thus, probabilistic tractography is a two-step process, the first step uses DWI data and a model to infer a fibre orientation and its uncertainty in each voxel, the second step uses the estimates and the uncertainty to build a path probability map from one designated region of interest to another. Ultimately, it assesses how reproducible the results are and how robust it is against noise/uncertainty, but it does not quantify how strong a connection is.

Probtrackx2 was executed using modified Euler integration. The optimal number of steps, step size and curvature threshold parameter values used were determined at a later stage (see Chapter 3). For *post mortem* tractography, 3×10^5 streamlines were generated per seed voxel. For *in vivo* tractography, 2.4×10^6 streamlines were generated per seed voxel; the increased sample count maintained the same density of streamlines for the *in vivo* tractography, which had larger voxels (1 mm^3 *in vivo* vs. 0.125 mm^3 *post mortem*). Default FSL settings were used for all other parameters. These parameters are displayed in Table 2.1.

Parameter	Setting
Loopcheck	Yes
Use modified Euler streaming	Yes
Use anisotropy to contrain tracking	No
Use distance correction	No
Subsidiary fibre volume fraction threshold	0.01
Minimum length threshold (mm)	0.0
Seed sphere sampling (mm)	0.0

Table 2.1: Table of the default FSL parameter settings which were used in this study.

2.2.1.7 Tractographic regions of interest

Post mortem region of interest (ROI) masks were manually delineated with reference to a standard atlas (Saleem & Logothetis, 2012) and to myelin stained histological sections of the individual *post mortem* brain. The masks were drawn onto the b0 average for each hemisphere in all brains using FSLView (v3.1). Three kinds of masks were used to guide probabilistic tracking: Seed, Target, and Exclusion masks.

Seed Masks: Seed masks were created for the lateral geniculate nucleus (LGN), including separate masks for the magnocellular and parvocellular subcomponents (Fig. 2.1A), and for the extrastriate visual area V5/MT, located in the superior temporal sulcus of the macaque (Fig. 2.1B). Previously, the left hemisphere of each brain had been processed histologically and sections stained for myelin (Ahmed et al., 2012). The sections were 50 μm thick microtome-cut sections with one-in-five stained for myelin (Gallyas, 1979). This allowed a hand-drawn custom V5/MT mask for each brain in the left hemisphere that matched the area of myelin identified as V5/MT. The manual delineation of V5/MT is important in accounting for the high inter-subject variation in the size and location of V5/MT (Van Essen et al., 1981). Non-linear registration (FSL, FNIRT) was used to align

a mirrored copy of the brain onto the original image, in order to produce a V5/MT mask for the right hemisphere of the same brain. It may be possible in future studies to define highly myelinated areas like V5/MT from MR images, instead (Glasser & Van Essen, 2011; Large et al., 2016).

Target Masks: Two pairs of target masks were defined as subregions of the primary visual cortex (V1) with different topological representations of the visual field in each hemisphere, according to Van Essen et al.'s (1984) study on visual field representation in macaques. The first pair was based on visual field eccentricity, with one mask defining the central 0-11° eccentricity of the visual field (Central V1), and the other defining the peripheral (≥12°) eccentricity of the visual field (Peripheral V1). The second pair was based on visual field elevation, with one mask defining the lower visual field (Inferior V1), and the other subserving the upper visual field (Superior V1) (Fig. 2.2A).

Exclusion Masks: Exclusion masks were used to stop streamlines from running through the sulci, ventricles, or into the contralateral hemisphere.

Although the same brain was scanned both *in vivo* and *post mortem*, in some cases the *in vivo* brain image differed in shape from the *post mortem* brain image. This might have occurred due to physical deformations on removal of the *post mortem* brain from the skull, or due to distortions caused by the MR scanning process. Thus, *in vivo* fractional anisotropy (FA) images were registered to the corresponding *post mortem* FA images using non-linear registration (FSL FNIRT; Anderson et al., 2010). The resulting non-linear transform was then used to map *post mortem* ROI masks onto the *in vivo* DWI space, followed by manual corrections.

2.2.1.8 Extended target masks

In some cases it was difficult for a sufficient number of streamlines to reach the V1 cortical targets. This may result from the inherent path-length dependency bias of probabilistic tractography (Liptrot et al., 2014). For example, there was a strong negative correlation between the distance of a voxel from the seed (along the streamline pathway) and the number of streamlines that passed through it (average Spearman's correlation coefficient = -0.79, SD ± 0.15; *post mortem*, 12 hemispheres, 8 seeds/target combinations, n = 96; all coefficients $p < 0.02$). Additionally, it may have been due to the premature termination of streamlines as they traverse the narrow and sharply turning tracts of white matter that lead towards parts of central V1. Lastly, there was also greater ambiguity, across all *post mortem* brains, in the diffusion direction of the white matter voxels neighbouring cortical ROIs, indicated by lower mean FA values in voxels neighbouring cortical ROIs (mean FA: V5/MT = 0.40 [SD ± 0.11]; central V1 = 0.47 [0.10]; peripheral V1 = 0.57 [0.10]; superior V1 = 0.51 [0.10]; inferior V1 = 0.52 [0.10]) in comparison with a pure tract of white matter (corpus callosum = 0.80 [0.01]). There were stronger diffusion signals in the white matter next to LGN than near V5/MT from the same hemisphere (mean FA LGN = 0.53 [0.06]; mean paired difference = 0.13, t-test, $p < 0.001$).

These problems were addressed by defining extended target masks using a simplified version of the algorithm employed by Liptrot et al. (2014). The assumption underlying Liptrot et al's algorithm, and the approach employed in this study, is that if a streamline travelling from a seed to a target reaches an intermediate voxel with a high probability of connection to the target, then we may consider the streamline as having reached the target. Therefore, extended target masks were created comprising of white matter voxels that were highly connected and close to the V1 cortical masks. White matter connection strength was determined by seeding the cortical V1 masks in separate tractography sessions (5,000 samples per seed voxel, maximal curvature ±90°, step size 0.5 mm, maximum number of steps = 24). No target was provided, but the standard exclusion masks were still used.

A short maximum streamline length (12 mm) sampled only voxels that were close to the cortical V1 seed. The number of streamlines was counted in voxels exterior to any V1 cortical mask – and voxels with greater than the median number of streamlines were used to define a new white matter target mask. The resulting masks extended approximately 2-4 mm on average from V1, reaching at most 7 mm from V1. The original cortical masks were subtracted from these masks, and the resulting masks then served as the extended V1 targets for subsequent tractography analysis (Fig. 2.2B). Their intended purpose was to permit more streamlines seeded in V5/MT to reach the especially central V1 targets, and to amplify the number of streamlines reaching V1 from LGN (see Results in Chapter 3 for analysis of their effect on the tractography results).

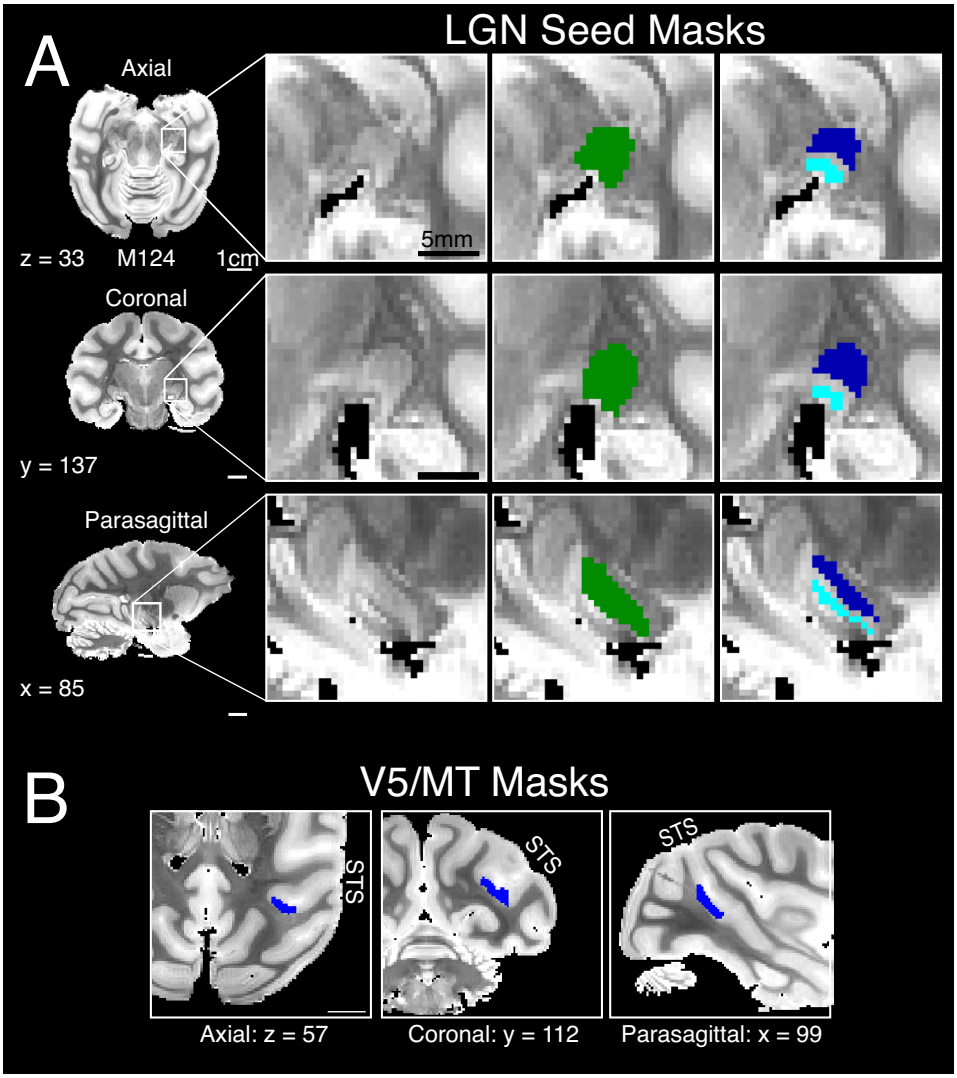

Figure 2.1: **Tractography seed masks.** **(A)** Axial (top row), coronal (middle), and sagittal (bottom) b0 image slices of the LGN from one animal (M124, left column), with magnification of the region of interest (right columns). Tractography was seeded from either all of LGN (green) or from the magnocellular (light blue) and parvocellular (dark blue) layers separately. **(B)** V5/MT seed mask (blue) in the superior temporal sulcus (STS) labelled. White scale bars are 1 cm, black scale bars are 5 mm.

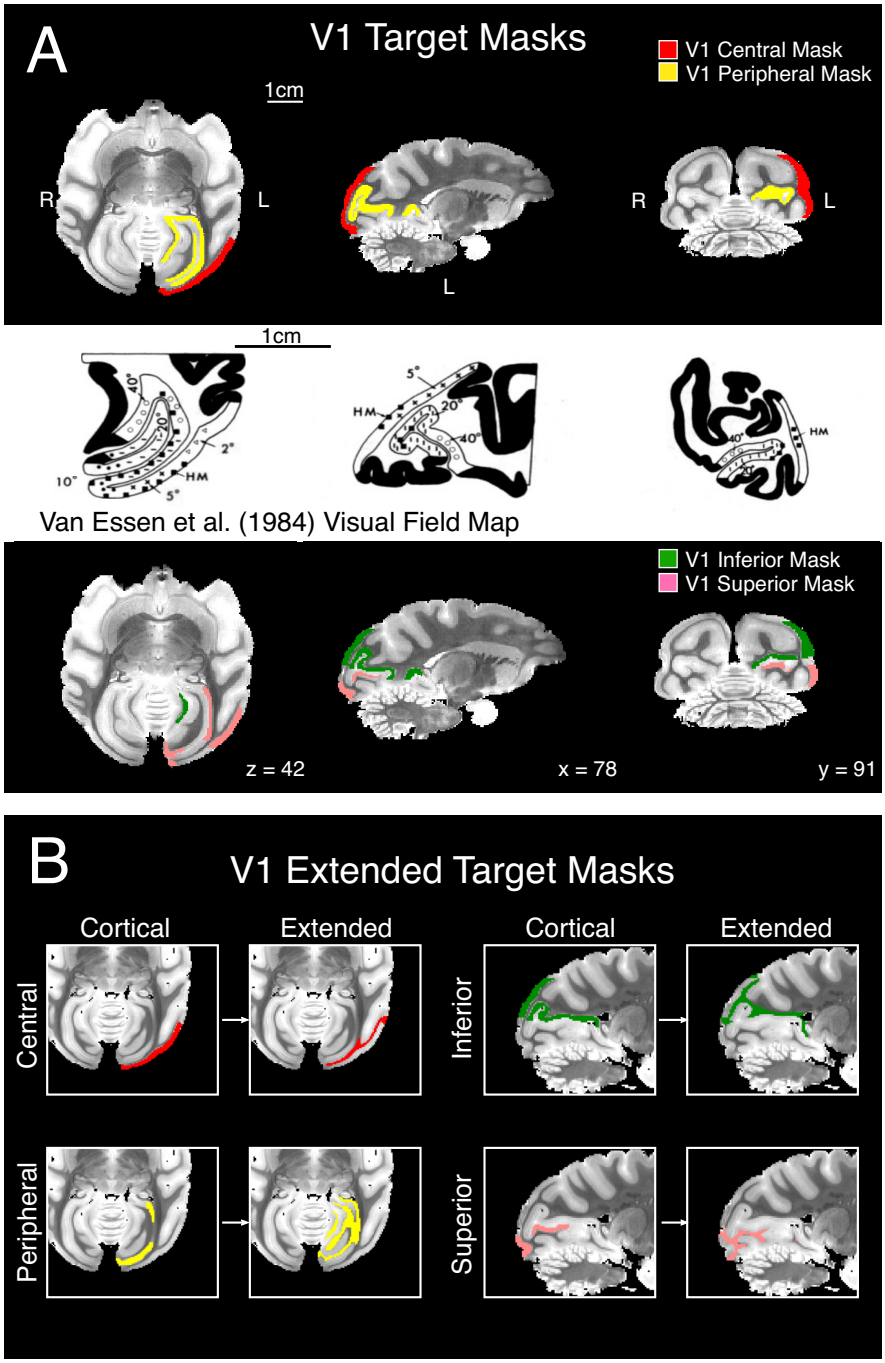

Figure 2.2: **Tractography target masks.** **(A)** V1 was divided into cortical target masks according to its retinotopy. V1 was divided either by eccentricity (central visual field representation, red; peripheral, yellow) or by elevation (inferior visual field, green; superior, pink). The V1 neurophysiological topographic map from Van Essen et al. (1984) is shown, for comparison. **(B)** V1 cortical masks (left of arrow) were extended into well-connected, neighbouring white matter (right of arrow). These well-connected voxels were identified using tractography seeded from the different V1 cortical masks. White and black scale bars are 1 cm.

2.2.1.9 Predicting the visual topography of seed areas

The probabilistic algorithm produced a map of the seed area, showing how many streamlines reached a specific target from each voxel; this is referred to as a streamline frequency map. This allowed a label to be assigned to each seed voxel according to the target with which it had the highest probability of landing a streamline. Thus, labeling each seed voxel was equivalent to predicting the visual topography of the seed area from the estimated number of connections it made with the different targets, because the target masks represented different visual field representations. However, it was important to first overcome a potential bias in probabilistic tractography. Dr. Jackson Smith developed a normalization strategy to overcome potential biases in probabilistic tractography, which is illustrated in Figure 2.3 (figure reproduced with permission from Dr. Jackson Smith).

Suppose that a seed region is used in two sessions of probabilistic tractography that target one area (Target 1) or another (Target 2). Streamlines coming from different locations in the seed (Fig. 2.3A, x-axis) may have different probabilities of reaching a given target, resulting in different numbers of streamlines (y-axis) that reach the target from different parts of the seed (peaks). One target (Target 2) may happen to receive a higher baseline level of streamlines than a different target (Fig. 2.3A, white; compared with Target 1, black). In practice, this might result if one target was larger than the other, or closer to the seed (Liptrot et al., 2014). Thus, labelling seed voxels based on the number of streamlines that reached each target could underestimate which parts of the seed area were relatively better connected to the target with a lower baseline level of hits. As Figure 2.3A suggests, there might be an iceberg effect; too much of the seed would be labelled by Target 2, and too little by Target 1.

Streamline frequency maps are spatial histograms. A standard technique for comparing the shapes of histograms with different sample sizes is to estimate their probability density functions (PDF). Therefore, the strategy employed was to normalise the streamline frequency maps by first applying moderate spatial smoothing (3D Gaussian convolution

kernel, 0.5 mm SD *post mortem*, 1 mm SD *in vivo*), to overcome regions of sparse sampling, and then computing the probability density of each seed voxel:

$$p_i = \frac{s_i}{(S \times v)}$$

and,

$$S = \sum s_j$$

Where s_i is the number of streamlines from the i^{th} seed voxel that reached a designated target, S is the total number of streamlines from all seed voxels that reached the same target, v is the volume of a voxel (0.125 mm^3 *post mortem*, 1 mm^3 *in vivo*), and p_i is the probability density of the i^{th} voxel. This estimated the underlying probability density function (PDF). Figure 2.3B illustrates how the normalised streamline counts in Figure 2.3A are expected to produce PDF estimates with equivalent baselines and peaks. For the tractography analysis, a PDF map was computed for each seed and target combination. Seed voxels were then labelled according the target that gave it the highest probability density. In Figure 2.3B, coloured areas under the PDF curves show which parts of the seed would be labelled by Target 1 (black) or Target 2 (white); unlike in Figure 2.3A, the seed is evenly divided between both targets.

Figure 2.3C-E demonstrates the normalisation of an example seed area (LGN, left hemisphere, M127 *post mortem*) when targeting either central (orange) or peripheral (yellow) V1. In these panels, voxels are ordered along the x-axis based on the difference between the central PDF and the peripheral PDF, while the vertical line separates central (left) from peripheral (right) seed voxels. The raw streamline counts were biased in favour of peripheral V1 (Fig. 2.3C), which had a higher baseline average (yellow square) than central V1 (orange square). After estimating the PDF from each set of streamline counts (Fig. 2.3D), the counts were normalised by the baseline average for each target (squares), but the shape of each curve stayed the same (compare C & D). Subtracting peripheral from

central PDFs (Fig. 2.3E, ΔPDF), then gives the label of each seed voxel. Voxels where the peripheral PDF was less than central ($0 < \Delta$PDF) were predicted to have central visual field representation, while voxels where the central PDF was less than peripheral (ΔPDF < 0) were predicted to have peripheral visual field representation. The same technique was used to predict the visual field representation of every seed voxel for each pair of V1 targets; once to determine its visual eccentricity (V1 central vs peripheral), and again to determine its visual elevation (V1 inferior vs superior).

To summarise seed voxel labelling across all of the *post mortem* data, the population average difference of PDFs was found (Fig. 2.3F & G). In order to sort voxels along the x-axis by the difference in PDFs (as in panels C-E), the voxel order first had to be normalized to account for different seeds sizes (different hemispheres having seeds with different numbers of voxels). This normalization was done by dividing by the number of voxels to give each voxel a number between 0 and 1 (where 0 means the voxel with the biggest PDF value, and 1 means the voxel with the smallest PDF value), and then applying a cubic-spline interpolation separately to each PDF using MATLAB.

For example, you might have two PDFs from masks with 2 and 3 voxels. The x-axis plot for the two PDFs, as in panel D, would have values:

1 , 2 , 3

1 , 2

Normlising by dividing with the number of voxels gives:

0.33 , 0.66 , 1

0.5 , 1

Performing a one-dimensional interpolation produces:

0.33 , 0.66 , 1

0.33 , 0.66 , 1

The average of PDF values can then be computed to produce the plots as in panels F & G. For both the central-to-peripheral (F) and inferior-to-superior (G) topographies, there were parts of both the LGN (solid) and V5/MT (dashed) seed regions with a clear preference for one V1 target or the other (95% bootstrap confidence intervals, grey shading). Thus, we were able to predict the visual topography of both seed regions by estimating their connections to different parts of V1.

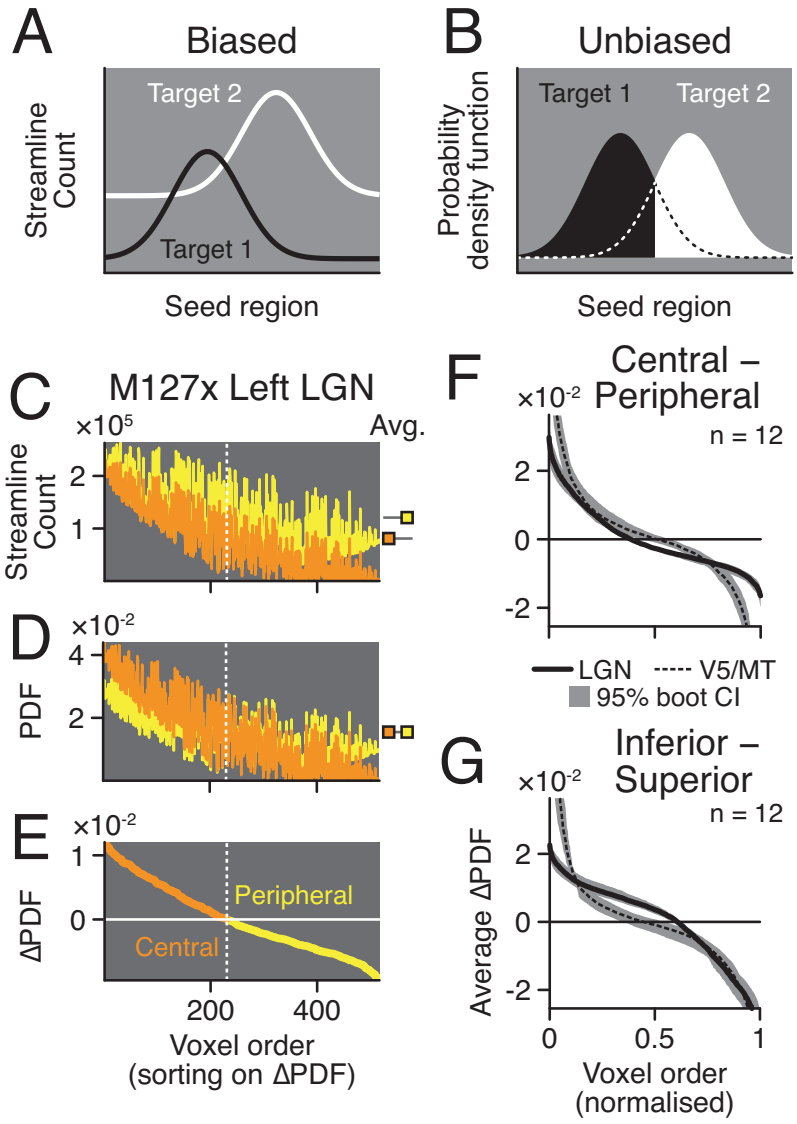

Figure 2.3: **Predicting topographic maps using probabilistic tractography. (A)** Illustration of potential bias in probabilistic tractography. The streamline frequency map from a seed region (mapped on x-axis to Target 1 (black) is on average less than Target 2 (white); this could occur if Target 2 was closer to the seed. **(B)** Normalising streamline counts by estimating the probability density function (PDF). Each part of the seed is assigned a visual representation (coloured area) based on which target it got the most probability density from, either Target 1 (black area) or Target 2 (white area). **(C)** An example streamline frequency map (M127 left LGN *post mortem*) when targeting either central (orange) or peripheral (yellow) representation in V1. Squares show the average frequency. **(D)** Same as C, but showing the PDF estimates. **(E)** The central PDF in D minus the peripheral PDF. Colours indicate which visual field representation the seed voxels were assigned. In C-E, seed voxels were ordered the same way on the x-axis, by the difference of PDF values in E. **(F)** The population average difference of PDFs for visual eccentricity maps, in LGN (solid) and V5/MT (dashed). **(G)** Same as F, except showing the average PDF difference for visual elevation maps. Grey shading in F & G shows 95% bootstrap confidence intervals.

2.2.1.10 Evaluating the topographic predictions based on tractography

The predicted maps of visual eccentricity and elevation in LGN were validated using a high-resolution (25 µm isotropic voxels) digital atlas of a Rhesus LGN (Erwin et al., 1999). The atlas was based on a single LGN mapped with a combination of histological and electrophysiological techniques. The LGN atlas was divided into two pairs of distinct regions based on visual field position. For one pair, parts of the LGN with either central (0-11°) or peripheral (≥12°) visual field eccentricity were identified in the atlas. For the other, the parts with visual field elevations that were either above (superior) or below (inferior) the horizontal meridian were identified. This provided a benchmark against which the tractography-based maps of LGN could be directly compared. To do this, each LGN seed mask was first registered to a binary mask of the atlas (FSL, FLIRT, linear affine transformations); the same transformations were then used to register the predicted topographic maps onto the atlas. Any part of the registered LGN that fell outside of the atlas was removed before further analysis because it would not be possible to assess the classification of these voxels. On average 87.0% (SD ± 4.61%, n = 12) of the volume of registered LGN was retained. Finally, the percentage of correctly classified voxels was found in each subregion of the atlas (central, peripheral, inferior, superior). For example, the percentage of voxels with a 'correct central' label was found by taking all voxels classified as central falling on the central atlas region over all the voxels falling on the central atlas region. These scores measured the success of our topographic predictions in LGN, as the percentage of voxels in each subregion of the atlas with the correct label can be compared with the chance level of 50%. A statistical comparison of whether this similarity was significantly different from chance was computed using a randomised non-parametric test (see following section *Randomised non-parametric tests*).

To verify the predicted visual topography of V5/MT, the predicted maps were first compared qualitatively with electrophysiological visual maps of V5/MT obtained previously in this lab from other animals (Krug et al., 2004). As it was not possible to register our

predicted maps of V5/MT to the electrophysiological visual maps, an alternative method of quantitative validation was required. This was achieved by computing the spatial centres of gravity (COG) of for each part of a single predicted topographic map (e.g. central and peripheral), and comparing the spatial separation of these two parts. The COGs were computed for the underlying PDF maps upon which it was based. They are defined here as the average position of each seed voxel, weighted by the voxel's probability density of landing a streamline onto a given target. Therefore, the COG is pulled towards the part of the seed that landed the most streamlines on a specific target. Different COGs could then be computed for different parts of the same seed mask and the Euclidean distance between the COGs computed. The significance of this spatial separation was compared using another randomized non-parametric test. The same analysis was also carried on the predicted LGN topographic maps.

2.2.1.11 Randomised non-parametric tests

This study employed two randomised, non-parametric resampling procedures (e.g. Efron & Tibshirani, 1993; Nichols & Holmes, 2002) to estimate the significance of the two measures that were used to compare the arrangement of the predicted maps; one measure being the distance between COGs for two parts of a single topographic map, and the other measure being the voxel-wise similarity of topographic labels from one map to another. The randomised non-parametric tests were implemented using a MATLAB function written by Dr. Jackson Smith.

In the first case, a randomised, non-parametric procedure was used to test for significant differences in COG position. The test was carried out by resampling the pair of PDF maps that were used to find the COGs. A single resampling was obtained by exchanging PDF values between two maps in a random number of randomly selected seed voxels. In this example, this would require swapping values of the PDF map targeting central V1 for the values of the map targeting peripheral V1. After the swap, new COGs were computed and

the Cartesian distance was found. The process was repeated 10,000 times to produce a distribution of COG distances. This distribution was used to estimate confidence intervals (2.5 and 97.5 percentiles for lower and upper 95% intervals) and the p-values (fraction of the distribution greater than the empirical distance).

The second form of random permutation test was used to estimate the significance of the voxel-wise similarity between pairs of topographic maps. It was used in the following comparison of datasets: *post mortem* DWI vs LGN atlas, *in vivo* DWI vs LGN atlas, and *post mortem* vs *in vivo* DWI. In the first two cases, each predicted topographic LGN map was registered to the LGN atlas (see above). In the third case, the *in vivo* streamline frequency maps were registered onto the *post mortem* image of the same brain before predicting the *in vivo* topographic maps. The voxel-wise similarity of two topographic maps was quantified by asking what percentage of voxels were assigned the same visual field representation in both. For each permutation of the test, the topographic labels were randomly exchanged between voxels - this was done separately for each map. The effect was to permute the position of voxels in each map within the spatial confines of the region of interest. After the spatial permutation, the percentage of voxels with the same topographic label in both maps was found. This procedure was repeated 10,000 times, yielding a distribution of percentages from which to estimate confidence intervals and p-values. An advantage to this approach was that no assumption had to be made about the chance level of similarity. Because the prediction of topographic maps was coarse, there were only two parts to each map, i.e. two topographic labels. If each map were evenly divided, then the chance similarity of any two maps would have been 50%. But if one or both of the maps was dominated by one topographic label, then the chance level could vary between 0 and 100%.

2.2.1.12 Connectivity probability index

In order to compare the relative number of connections between a V1 target and the magnocellular or parvocellular layers of LGN, a quantitative estimate of the probability with which each of the parts of the LGN is connected to the target is required. This measure should be normalized by the size of the seed region and the number of streamlines sampled. This connectivity probability measure gives the probability of the seed generating a streamline that reached the target:

$$p = \frac{S}{(k \times V)}$$

Here p is the connectivity probability, S refers to the total number of streamlines between the seed and target, V is the volume of the seed mask (voxels), while k is a constant referring to the number of streamlines generated per voxel. Due to the low value of many connectivity probabilities, the resulting data were prone to positive skewness. To compensate, all connectivity probabilities were logarithmically transformed (after multiplying with 10^7) to give a connectivity index, used to compare the relative connectivity probability between LGN and V1 in different visual pathways.

2.2.1.13 Standard space

For spatial normalisation of the predicted maps, which was required during the randomised non-parametric tests and for visual presentation of the results in stereotactic alignment, all brains and predicted topographic maps were transformed onto the 112RM-SL atlas of McLaren et al. (2009). Each *post mortem* b0 average image was registered onto the atlas (FSL, FLIRT, affine linear registration), and the resulting transformations were used to register the predicted topographic and PDF maps. For 3D visualisation of streamline density through the white matter, b0 average images were registered to an MNI standard

macaque brain (McConnell Brain Imaging Centre, Montreal Neurological Institute, McGill University; FSL, FNIRT), and the same transformations were used to register whole-brain streamline density maps.

2.2.2 *In vivo* human

2.2.2.1 Subjects

Six adult human diffusion-weighted imaging datasets were acquired from the Human Connectome Project, WU-Minn Consortium (Principal Investigators: David Van Essen and Kamil Ugurbil; 1U54MH091657) funded by the 16 NIH Institutes and Centres that support the NIH Blueprint for Neuroscience Research; and by the McDonnell Centre for Systems Neuroscience at Washington University. Included in the study were 2 males and 4 females (age range 22 – 35).

2.2.2.2 Data acquisition

Data were acquired with a Siemens 3T Skyra scanner equipped with a maximum gradient strength of 100 mT/m. DWI was collected using 32-channel receive coils (Ugurbil et al., 2013) and a 2D spin-echo single-shot multiband EPI sequence with a multi-band factor of 3 and monopolar gradient pulse (Stejskal & Tanner, 1965; Sotiropoulos et al., 2013). A SENSE1 magnitude reconstruction was used (Sotiropoulos et al., 2013d). Whole-brain DWI volumes were collected at 1.25 mm x 1.25 mm x 1.25 mm resolution (matrix size PE $\times$ Readout = 144 $\times$ 168 with left–right (LR) phase encoding (PE) and 6/8 PE partial Fourier), with 111 slices acquired in interleaved slice order to cover the entire brain using a Multiband (MB) factor of 3 for slice acceleration and no acceleration along the PE direction. A total of 108 echoes were collected, with echo spacing of 0.78 ms and readout bandwidth 1490 Hz/pixel, resulting in a total echo train length (ETL) of 84.24 ms. Sampling in q-space includes 3 shells at b = 1000, 2000 and 3000 s/mm^2 (diffusion times are Δ = 43.1

ms and δ = 10.6 ms). TE and TR are matched across shells (TE = 89 ms, TR = 5.5 s). For each shell, 190 data points are obtained, corresponding to 90 isotropic diffusion-sensitised directions and 5 b = 0 images acquired once per phase encoding (PE) direction (i.e. LR and RL pairs). Total scanning time for this protocol was approximately 55 min (https://www.humanconnectome/org/documentation/MGH-diffusion/).

High-resolution T1-weighted structural images were acquired using a 3D MPRAGE sequence with the following parameters: 1 mm isotropic voxels size, TR = 2530 ms, TE = 1.15 ms, TI = 1100 ms, flip angle = 7°, FOV = 256 x 256. Acquisition time was 6 minutes. Data were acquired with a minimal level of pre-processing to combine PE pairs and correct for susceptibility distortions, eddy-currents and head motion (Andersson et al., 2003; Glasser et al., 2013). The datasets were also corrected for gradient non-linearities and aligned to the T1 structural space using spline interpolation and rigid body transformation.

2.2.2.3 Probabilistic tractography: Human

Probabilistic tractography was carried out on the human DWI data using the same implementation and methods described previously for the macaque DWI data. The optimal step size, number of steps, and curvature threshold parameters for human DWI data were based on analysis of the effect of these parameters on the *post mortem* data (see Chapter 3 Results). Seed masks were manually delineated using FSL tools with reference to both a registered MNI LGN mask, and a human brain atlas (Mai et al., 2004). Target masks were registered onto the T1-weighted anatomical image from a probabilistic atlas of visual topography in human cortex created by Wang et al. (2015). These probabilistic maps of different regions of V1 were identified using fMRI retinotopic mapping paradigms averaged across 53 subjects and displayed in volume-based standard space. The top 10% of voxels of these probabilistic maps were binarized and registered to the individual diffusion imaging space for use as target masks. Target masks were made of regions defining the central (0-11°), peripheral (≥12°), inferior, and superior visual field representations in V1

(Fig. 2.4B). The LGN was delineated manually, as visual inspection of the MNI atlas LGN clearly showed the LGN to be incorrectly located (Fig. 2.4A). Since the T1-weighted anatomical image had been pre-registered to the same space at the diffusion images (1.25 mm^3 isotropic voxel resolution), tractography was carried out in this native, diffusion space and run individually for all subjects.

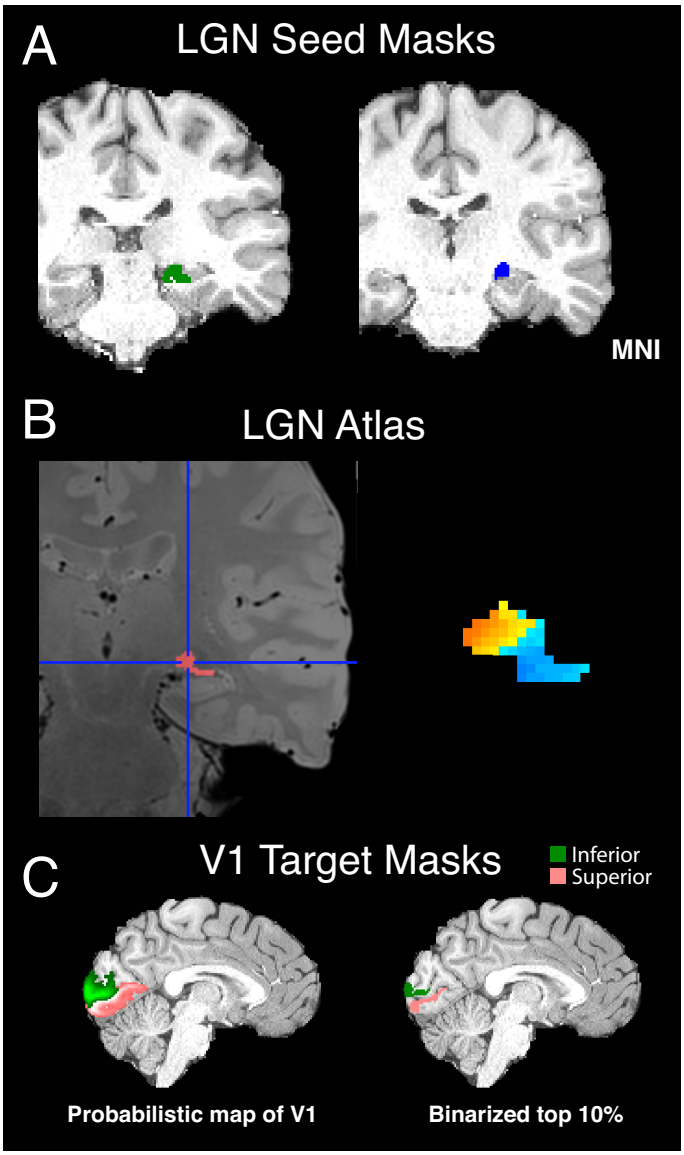

Figure 2.4: **Human tractography seed masks, LGN atlas, and V1 target masks.** **(A)** Representative LGN seed mask shown here on coronal sections. LGN seed masks were manually defined using FSL tools (green) and with reference to Mai et al.'s (2004) atlas of the human brain. The MNI atlas defined LGNs (blue) were not used as these were incorrectly located (too anterior), and their size and shape was also not typical of a human LGN. The LGN atlas in **(B)** confirms that the manual delineation more accurately depicts the size, shape, and location of the LGN. The LGN atlas was defined using a high-resolution proton-density scan to define the LGN boundaries, and pRF mapping to define the retinotopic organization. This figure shows the elevation mapping, with orange-yellow representing the inferior visual field, and light blue-dark blue representing the superior visual field. **(C)** Representative V1 target masks (inferior in green, superior in pink). Target masks were created from a probabilistic atlas of visual topography in human cortex (Wang et al., 2014). The top 10% of voxels of these probabilistic maps were binarized and registered to the individual diffusion imaging space for use as target masks.

2.2.2.4 Evaluating the topographic predictions based on tractography: Human

The predicted maps of visual eccentricity and elevation in LGN were validated using maps obtained during a population receptive field (pRF) study on retinotopic maps in human LGN (DeSimone et al., 2015). The pRF model is a voxelwise forward-encoding approach that uses spatially and temporally dynamic stimuli to derive RF properties from the blood oxygen level-dependent (BOLD) signal of a population of neurons within a single voxel. Eccentricity and elevation maps in the LGN were computed by DeSimone et al. using the pRF model. Averaged proton density-weighted images were used to constrain and confirm the functional activations. The obtained maps were 0.75 mm isotropic, and were separated into regions representing inferior and visual field, and central (0-11°) and peripheral field (≥12°). Using similar methods to the *post mortem* and *in vivo* macaque analyses, these maps provided a benchmark against which the tractography-based maps of LGN could be compared. This was achieved by registering the predicted maps to the atlas, and computing the percentage of voxels labelled similarly. Statistical comparison of whether this similarity was significantly difference from chance was computed using a randomised non-parametric test as before.

2.3 Summary

This chapter outlined the data acquisition and processing stages involved in the analysis of datasets with diffusion-weighted imaging. The first part of this chapter described the experimental procedures involved in scanning macaques *in vivo* and the subsequent stages of extracting and acquiring scans from *post mortem* macaque brains. The chapter then detailed the stages involved in carrying out probabilistic tractography and evaluating the results, both of which include novel approaches developed in this thesis. The processes are kept the same for both *post mortem* and *in vivo* where possible. Where differences do

exist, such as in defining the regions of interest for tractography, and in the tractographic parameters, they are explicitly stated. The final part of the chapter described the data acquisition and processing stages for Human Connectome Project acquired human diffusion data. Again the process of carrying out and evaluating the probabilistic tractography was kept as analogous as possible to the macaque diffusion-weighted imaging analyses.

Chapter 3

Optimizing probabilistic tractography

3.1 Introduction

Probabilistic tractography involves the selection of a number of parameters used in the probabilistic tracking process. To date, there has been relatively little systematic evaluation of how the parameters concerning streamline length and streamline curvature influence the outcome of tractography. While some studies have explored the effect of step size (Parizel et al., 2007; Tournier et al., 2011; Côté et al., 2013) and streamline curvature (Tournier et al., 2002; Côté et al., 2013; Takemura et al., 2016), these studies usually involve deterministic tractography as opposed to probabilistic tractography, do not explore the overall effect of streamline length, and are often modelled on simulated data.

The default parameters for probabilistic tractography given in the diffusion toolbox in FSL are: maximum number of steps = 2000, step length = 0.5 mm, curvature threshold = 0.2. While there is little consensus on the appropriate parameters to use, one previous human study using probabilistic tractography as implemented in FSL used a step length of 0.2

mm and no curvature threshold (Miller et al., 2012), and another study also on humans used a step length of 0.5 mm, 0.2 curvature threshold, with no maximum number of steps (streamlines allowed to continue until reaching a mask representing the brain surface) (Behrens et al., 2003).

The maximum number of steps limits the number of steps a streamline can take before it is terminated. The step length determines the length of each step, and its selection should therefore also take into the consideration the size of the voxels used. The number of steps and the step length combine to limit the maximum length of streamline permitted, as the length of the streamline is the product of the length of each propagation step and the size (distance in mm) of each step. The overall streamline length should therefore be considered when choosing appropriate tractography parameters. The curvature threshold limits how sharply streamlines can turn. The value is the cosine of the minimum allowable angle between two steps (e.g. 0.2 corresponds to a minimum angle of approximately ± 80 degrees). This constraint is used to allow for the expectation that white matter fibres will not exhibit sharp changes/reversals in direction (Schmahmann et al., 2007; Wakana et al., 2007; Behrens & Jbabdi, 2009). Increasing the angle threshold has previously been shown to result in more and longer streamlines in a deterministic streamline tractography algorithm (Parizel et al., 2007). These default FSL parameters are those generally employed by studies on probabilistic tractography, however, they are more appropriately designed for diffusion imaging data acquired from human subjects, and at *in vivo* clinical image resolutions (Miller et al., 2012; Behrens et al., 2003).

The aim here is to develop a set of tractography parameters suited for detecting realistic connectivity in the *post mortem* macaque brain. This represents an important starting point for validating the results of diffusion imaging, as the results can be systematically compared to 'gold-standard' histological tract-tracing and electrophysiological methods with a high degree of confidence due to the high-quality data afforded by *post mortem* imaging. Once the effects of different tractography parameters for *post mortem* macaque diffusion imaging are established, the aim will then be to determine whether DWI and prob-

abilistic tractography is able to uncover topographic connections across multiple brains, for different seed regions (LGN and V5/MT), and different targets (central-peripheral V1, inferior-superior V1). These results can then provide the benchmark for the *in vivo* applications of diffusion imaging.

3.2 Methods

To explore the effect of different tractography parameters on LGN tractography, the predicted maps of LGN visual eccentricity were evaluated for a single post mortem hemisphere (M130, Left), in which 3 tractography parameters were varied systematically. The number of steps was varied in relation to the step size to limit the maximum permitted streamline length as a percentage of the total anterior-to-posterior brain length (approximately 140-150 mm). Thus, the following parameters were used:

Streamline length: 50%, 75%, 100%, 125% (of total brain length)

Step Length: 0.0625, 0.125, 0.25, 0.5

Curvature Threshold: 0.0, 0.2, 0.4, 0.6

As described in the Methods (Chapter 2), the predicted maps of visual eccentricity were validated against the digital LGN atlas (Erwin et al., 1999) for each parameter combination. The tractography-derived predicted topographic map was first registered to the LGN atlas. The percentage of correctly classified registered voxels was then found for each subregion of the atlas. For example, the percentage of voxels with a 'correct central' label was found by taking registered voxels classified as central that fell on the central part of the atlas, divided by all registered voxels that fell on the central part of the atlas (registered voxels labelled central in central atlas region / all registered voxels in central atlas region). The same calculation was carried out for the peripheral atlas region, and the results combined together to give a percentage correct score reflecting the accuracy of the connectivity-derived LGN segmentation.

As the correct percentage score is derived from all correctly classified central voxels and all correctly classified peripheral voxels combined, it is possible for correct percentage score to be the same for two LGN maps with differing proportions of labelled central and peripheral voxels. To further evaluate the contribution each parameter combination makes towards

the predicted LGN topography, the number of voxels labelled central and the number of voxels labelled peripheral were also computed and given as a proportion of the total number of voxels. This is the proportion of central and peripheral voxels before registration to the digital LGN atlas.

Finally, this process was carried out for tractography sessions using cortical grey matter targets (NonExt) and for tractography sessions using extended target masks (Ext), and for before and after probability density normalization (pre/post-PDF) (see Chapter 2, Methods, for details on probability density normalization).

3.3 Results

3.3.1 Effect of different tractography parameters on predicting LGN topography

Figure 3.1 shows the mean accuracy of the predicted map for various levels of the maximum streamline length (Fig. 3.1A), step size (Fig. 3.1B), and curvature threshold (Fig. 3.1C) parameters. The mean accuracy is computed for each condition (NonExt Pre-PD, NonExt Post-PD, Ext Pre-PD, and Ext Post-PD) for a given parameter value, pooled across all others. For example, the mean accuracy for 50% total streamline length is computed for each of the four conditions pooling together the percentage correct scores of all the different step sizes and curvature threshold values.

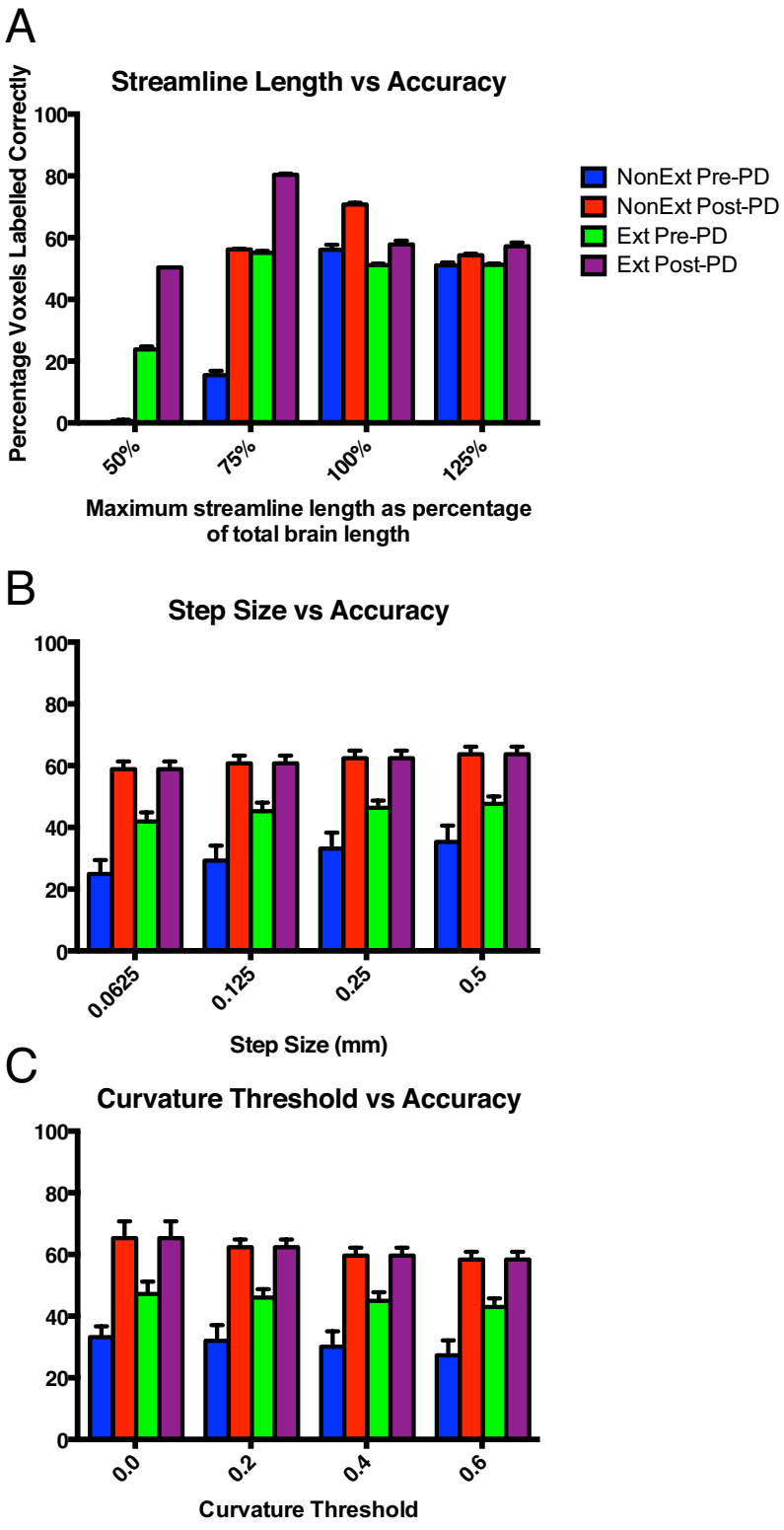

Figure 3.1: Graphs of the effect of **(A)** maximum streamline length, **(B)** step size, and **(C)** curvature threshold, on mean accuracy of predicted topographic map. Mean accuracy is computed for each condition for a given parameter value pooled across all others. Error bars are standard error of the mean.

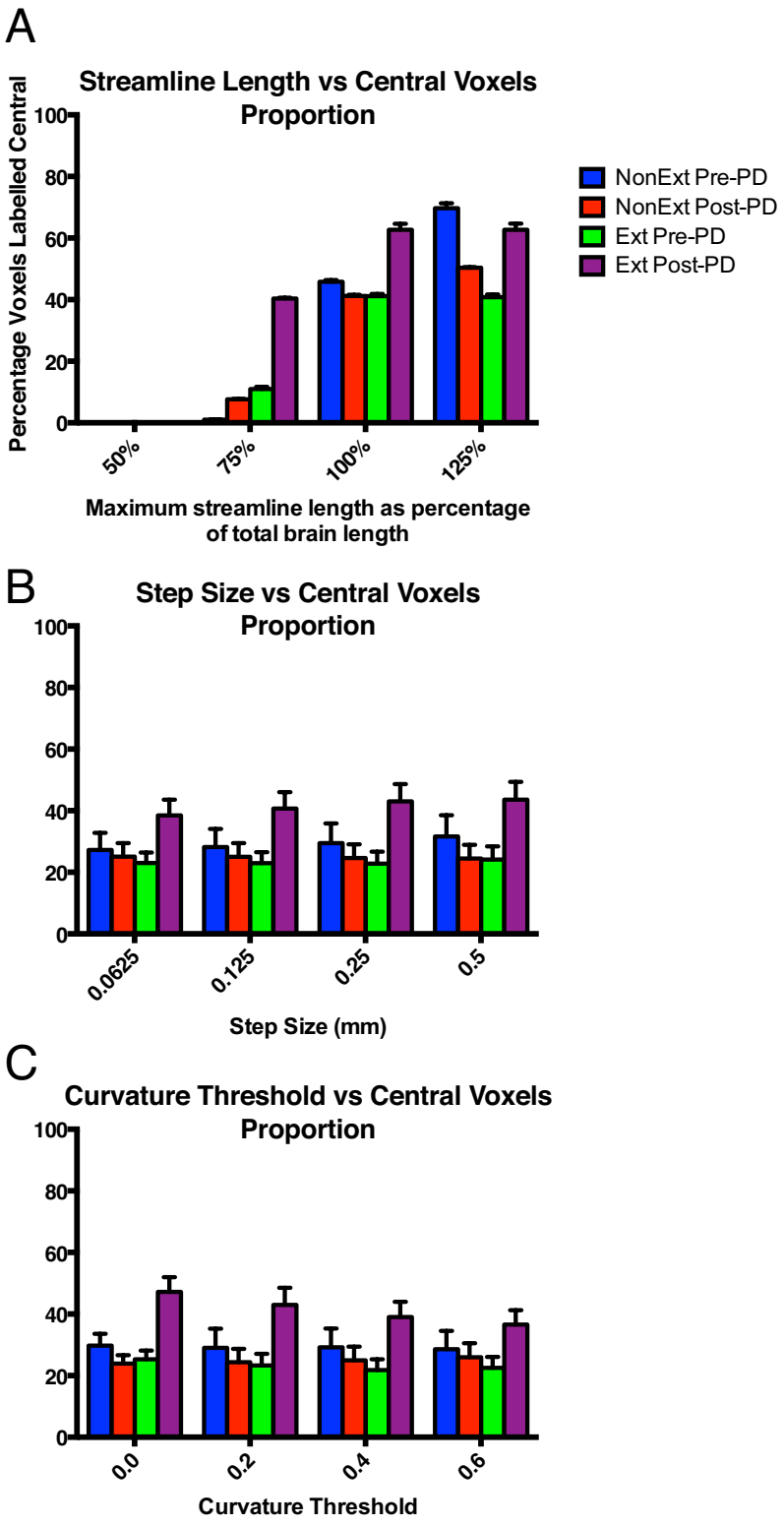

Figure 3.2: Graphs of the effect of **(A)** maximum streamline length, **(B)** step size, and **(C)** curvature threshold, on proportion of central voxels in the predicted topographic map. Mean accuracy is computed for each condition for a given parameter value pooled across all others. Error bars are SEM.

The results indicate that the mean accuracy of predicted topography is highest when the number of steps limits the total streamline length to 75% of the total brain length (Fig. 3.1A). This is the case for conditions when using extended targets, however mean accuracy is highest at 100% of the total brain length for conditions using cortical targets. This is likely to be related to the fact that cortical targets represent an increase in distance away from the seed compared with extended targets. Thus, the optimal maximum streamline length depends on the target type used. Overall, the results indicate that limiting streamlines to 50% brain length terminates them before they are able to reach V1 from LGN and therefore result in a failed segmentation. Streamlines 75% brain length for extended targets and 100% brain length for cortical targets result in accurate segmentations, however, increasing the maximum permitted streamline length to 100% for extended targets and 125% for cortical targets, reduces the accuracy of the segmentation, likely due to the introduction of spurious tracts.

A 2 x 2 x 4 ANOVA was carried out for target type x normalization x streamline length, which showed a significant three-way interaction ($F(3,240) = 72.79$, $p < 0.001$). This indicates that one, or more, two-way interactions differ across the levels of a third variable. There was a significant main effect of target type ($F(1,240) = 843.8$, $p < 0.001$), a significant main effect of normalization ($F(1,240) = 857.7$, $p < 0.001$), and a significant main effect of streamline length ($F(1,240) = 1212.2$, $p < 0.001$). There was no significant target x normalization interaction ($F(1,3) = 1.3$, $p = 0.25$. There was a significant target x streamline length interaction ($F(3,240) = 451.6$, $p < 0.001$. There was a significant normalization x streamline length interaction ($F(3,240) = 137.5$, $p < 0.001$).

In addition, the results from the analysis on the proportion of central voxels indicate that it is the increase in classification of central voxels at 100% and 125% streamline lengths that might reduce the accuracy (Fig. 3.2A). According to the atlas, 50.3% voxels should be classified as central when describing 0-11° of the visual field. Although the proportion of central voxels at 75% streamline length is much lower than 50.3% for all conditions, having much higher proportions of central voxels such as occurs with 125% streamline length

Condition	Max. Streamline Length	Step Size	Curvature	Accuracy
NonExt Pre-PD	100%	0.5 mm	0.0	67.1
NonExt Post-PD	100%	0.5 mm	0.2	75.8
Ext Pre-PD	75%	0.25 mm	0.0	57.9
Ext Post-PD	75%	0.5 mm	0.0	82.4

Table 3.1: Parameter combination with the highest accuracy of predicted topography for each condition.

results in a much lower accuracy of predicted topography, as more voxels are incorrectly classified as central.

The mean accuracy of the predicted topography does not appear differ significantly for different step sizes and curvature thresholds, although the mean accuracy is highest for 0.5 mm steps and 0.0 curvature threshold (Fig 3.1B&C). Given that the percentage scores are computed for all other parameters pooled together, the optimal combination of parameters may not necessarily be those combinations that use 0.5 mm steps and 0.0 curvature threshold. The best parameter combination for each condition is shown in Table 3.1 and represents the parameter combination for which the predicted topographic map had the highest similarity with the atlas. The predicted topographic map from each parameter combination was individually registered to the atlas and the similarity determined. Figure 3.3 plots the similarity between the atlas and the predicted topography maps for each parameter combination.

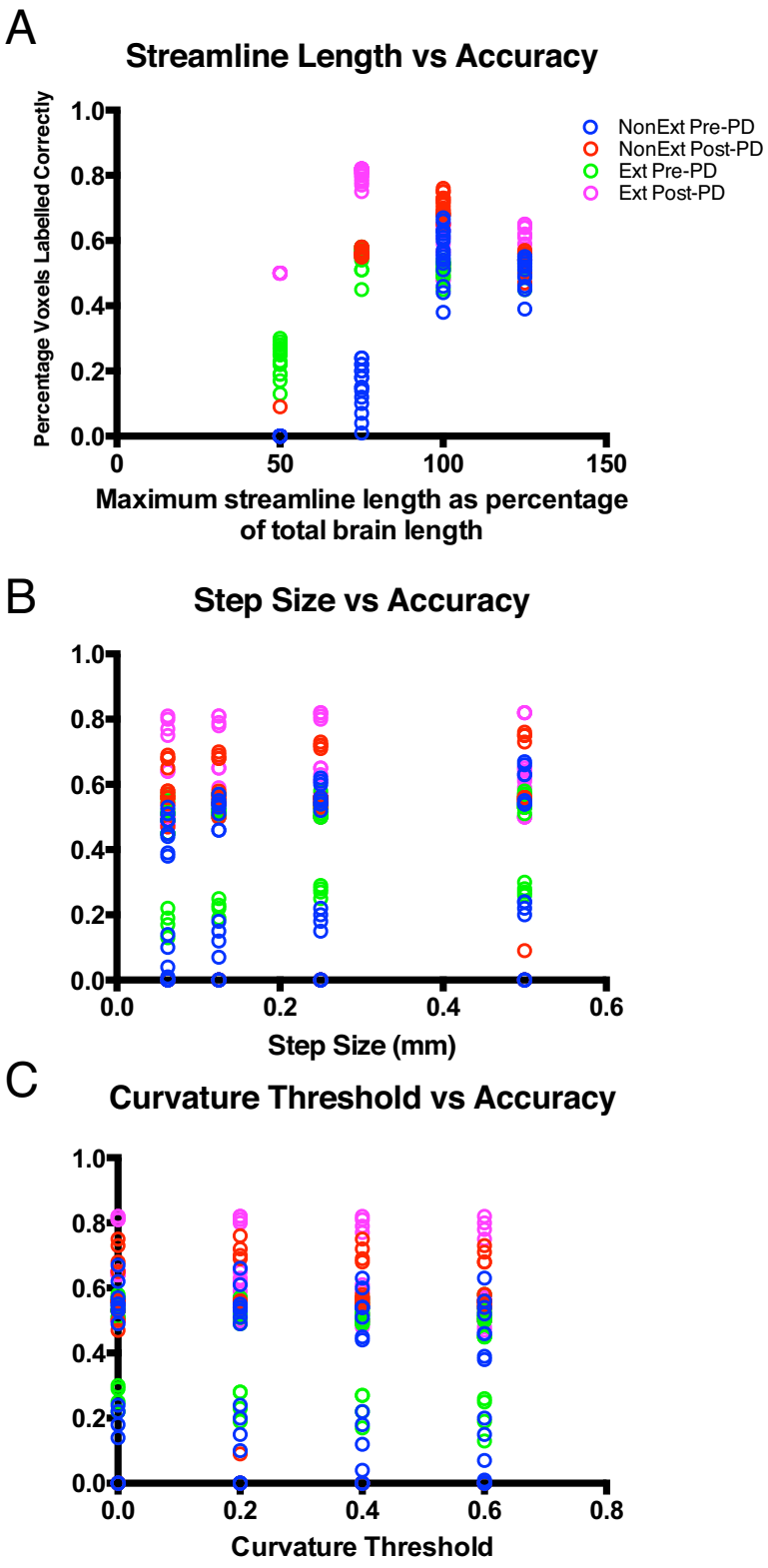

Figure 3.3: Scatter plot of the percentage similarity between the atlas and the predicted topographic map for every parameter combination, grouped by **(A)** maximum streamline length, **(B)** step size, and **(C)** curvature threshold.

The results from Table 3.1 and Figure 3.3 indicate that the highest accuracy is achieved using 75% brain length for number of steps, 0.5 mm steps and 0.0 curvature threshold. The finding that 0.5 mm steps is optimal fits with the conclusions of Tournier et al. (2011) study on the effect of step size on probabilistic streamlines. They observed using simulated data that small step sizes in relation to the voxel size result in more accurate tracking if the spread in fibre orientation distributions is assumed to come from noise only. However, since this is not the case, due to the inherently limited resolution of DWI, smaller step sizes result in underestimation of the uncertainty of the generated tracks, while step sizes matching the voxel size are more likely to reflect the ground truth.

The results from Table 3.1 also suggest that the best parameter combination may depend on whether cortical targets or extended targets are used, and whether probability density normalization is applied. Overall, it appears that accurate prediction of LGN topography uses 0.0 curvature threshold, and long enough streamlines to reach the target, but not excessively longer than required. A more fine-grained optimisation of the streamline length could be carried out to determine at which streamline length the peak accuracy is achieved, however, this would only be optimising the tractography for a single hemisphere. The primary purpose of this analysis is to determine appropriate tractography parameters to use for probabilistic tractography across many different brains for *post mortem* and *in vivo* diffusion datasets. Furthermore, it is evident that the use of extended target masks influences the seed to target distance, and that probability density normalization influences the accuracy of predicted maps. Therefore a next step is to determine what the effect of using extended target masks and probability density normalization is on accuracy measures of probabilistic tractography across all hemispheres.

	% Voxels Cent	% Voxels Peri	% Correct
Cortical Target: Pre-PDF (No smoothing)	4.0 (7.1)	96.0 (7.1)	51.2 (7.1)
Extended Target: Pre-PDF (No smoothing)	3.7 (6.5)	96.3 (6.5)	50.4 (2.9)
Cortical Target: Pre-PDF (With smoothing)	4.6 (10.3)	95.4 (10.3)	53.2 (0.1)
Extended Target: Pre-PDF (With smoothing)	2.0 (6.2)	98.0 (6.2)	49.6 (1.3)
Cortical Target: Post-PDF	21.7 (6.6)	78.3 (6.6)	65.7 (8.9)
Extended Target: Post-PDF	38.8 (4.0)	61.2 (4.0)	67.7 (8.8)

Table 3.2: Comparison of the effect target type and probability density normalization on the proportions of centrally and peripherally classified voxels, and the accuracy of predicted topography. Proportion of central voxels in LGN atlas is 50.3%. Tractography parameters are 75% maximum streamline length, 0.5 mm steps, 0.0 curvature threshold. ±SD in parenthesis (n =12).

3.3.2 Effect of extended target masks and probability density normalization on predicting LGN topography

After establishing the probabilistic tracking parameters in the previous section for a single hemisphere, the similarity of predicted LGN topographic maps of eccentricity and the atlas was computed for all *post mortem* hemispheres. A comparison of the mean percentage correct score for each topographic map is shown in Table 3.2 for cortical targets vs. extended target masks, and before and after probability density normalization (pre/post-PDF). The probability density normalization also involves a preliminary spatial smoothing step (3D Gaussian convolution kernel, 0.5 mm SD); therefore the mean correct percentage is also shown before applying the probability density function with and without the spatial smoothing. The proportions of central and peripheral voxels before registration to the atlas are also given (Table 3.2).

The results indicate that when probability density normalization is not applied, the effect of using extended target masks causes a small decrease in the number of streamlines reaching central V1 targets compared with targets confined to the cortical ribbon, and therefore reduces the percentage correct atlas score. However, when probability density normalization is applied, the percentage of voxels labelled 'central' increases relative to the proportion of peripheral voxels, and this is what likely leads to the higher percentage accuracy based on the atlas (Erwin et al., 1999). Furthermore, this effect appears to be stronger for the extended target mask tractography than when target masks are confined to the cortical ribbon. The expected proportion of central voxels, according to atlas, would be 50.3%. Smoothing appears to have little effect overall.

A 2 x 3 within subjects ANOVA found no significant effect of target type (Cortical vs. Extended targets, $F(1,11) = 0.131$, $p = 0.72$) on segmentation accuracy, but there was a significant effect of processing (Pre-PDF no smoothing vs. Pre-PDF with smoothing vs. Post-PDF, $F(2,22) = 68.194$, $p < 0.001$). Bonferroni corrected pairwise comparisons revealed significant differences between the Pre-PDF no smoothing and Post-PDF ($p < 0.001$) conditions, and between Pre-PDF with smoothing and Post-PDF ($p < 0.001$), but not between Pre-PDF no smoothing and Pre-PDF with smoothing processing conditions ($p = 0.59$). Bonferroni corrected pairwise comparisons were also carried out for extended targets vs. cortical targets for each processing condition (Pre-PDF no smoothing, Pre-PDF with smoothing, and Post-PDF). None of these pairwise comparisons were significant.

Overall, the results suggest the highest accuracy of the predicted topography is achieved using probability density normalization. Using extended target masks does not lead a significantly higher accuracy of segmentation, however, the expected proportion of central voxels (50.3%) is closer for extended targets post-PDF, than for cortical targets post-PDF (Table 3.2, 38.8% extended vs. 21.7% for cortical). Bonferroni corrected pairwise comparisons on the proportion of central voxels showed that significantly more voxels were classified as central when using extended targets vs. cortical targets Post-PDF ($p < 0.0001$), but no significant differences in proportion of central voxels between extended

targets vs. cortical targets, neither Pre-PDF no smoothing nor Pre-PDF with smoothing. Thus, when probability density normalization is applied, using extended targets masks over cortical target masks results in a significantly higher proportion of centrally classified voxels, which more closely matches the proportion of central voxels we would expect from the LGN atlas (Erwin et al., 1999).

Furthermore, the predicted topography appears to be qualitatively better with extended target masks (Fig. 3.4), and their use may be necessary for tractography sessions in which the number of streamlines reaching the targets is low (i.e. V5/MT to V1 tractography). The number of streamlines that reached a target was significantly lower for cortical targets (mean = 1,567,759 [SD ± 2,388,809]) compared with extended targets (mean = 47,067,839 [22,352,858]; paired Wilcoxon signed rank test, Z = 6.03, $p < 0.001$). Additionally, while the accuracy of predicted maps were not significantly different, the variance when using extended targets was reduced when compared to cortical targets, both before and after probability density normalisation (Table 3.2, cortical target SD ± 5.37%, extended target SD ± 4.34%, Levene's test, $p < 0.01$). Thus, the effect of extended target masks was to amplify the tractographic signal. On the basis of the results here, all subsequent LGN tractography sessions were conducted using extended target masks and probabilistic density normalization.

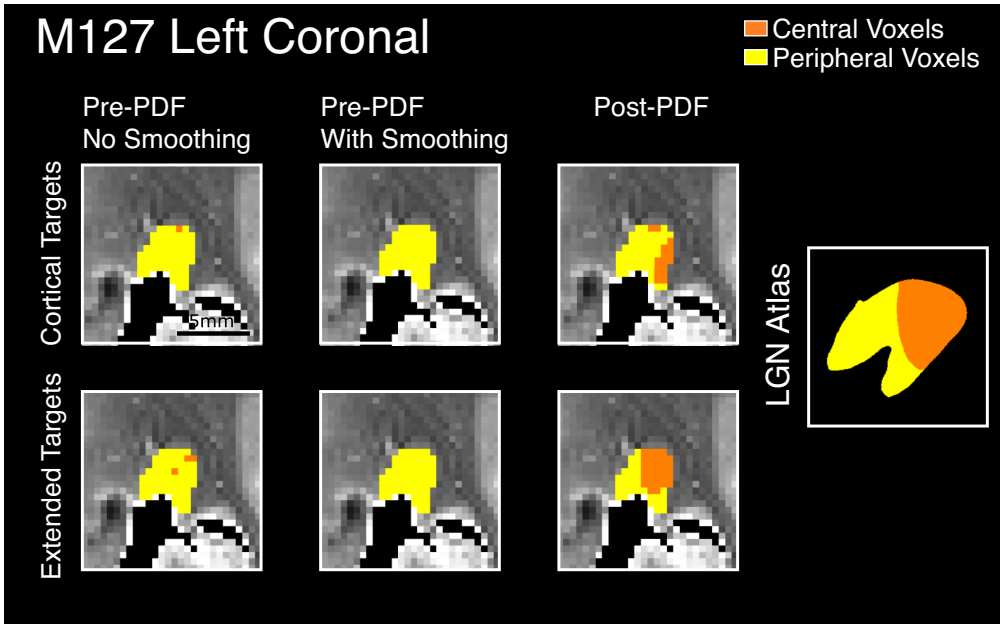

Figure 3.4: Representative predicted topographic maps for cortical vs extended targets taken from the same slice of the LGN under various processing conditions (M127). Although the probability density normalized topographic maps (Post-PDF) do not differ significantly in terms of classified voxels sharing the same label as the atlas for extended vs. cortical targets, this section highlights how the arrangement of voxels classified as central can differ for extended vs. cortical targets.

3.3.3 Effect of different tractography parameters on predicting V5/MT topography

The distance between centres of gravity (COGs) of the predicted topographies and the proportion of centrally labelled voxels were computed for each parameter combination. The same parameter combinations and the same hemisphere (M130 Left) were used as before. The distance between centres of gravity refers to the distance in millimetres between the COG for voxels classified as central and the COG for voxels classified as peripheral in the dorsal-ventral plane. The COGs were computed for the underlying PDF maps upon which the predicted topographic maps were based. They are defined as the average position of each seed voxel, weighted by the voxel's probability density of landing a streamline onto a given target. The value for the distance between COGs is the central COG subtracted from the peripheral COG. A positive value indicates the peripheral COG is more dorsal and would therefore match the more dorsal representation of the peripheral visual field in V5/MT in topographic maps determined from electrophysiology (Van Essen et al., 1981; Krug et al., 2004). According to Van Essen et al.'s study we would expect the peripheral COG to be approximately 3.5 mm dorsal of the central COG (Fig. 3.5). Furthermore, according to Van Essen et al.'s study (1981), the central 15° of the visual field is represented by slightly more than half of V5/MT. Therefore, in this study where central visual field is defined as 0-11° we would expect the proportion of central and peripheral voxels to be approximately equal.

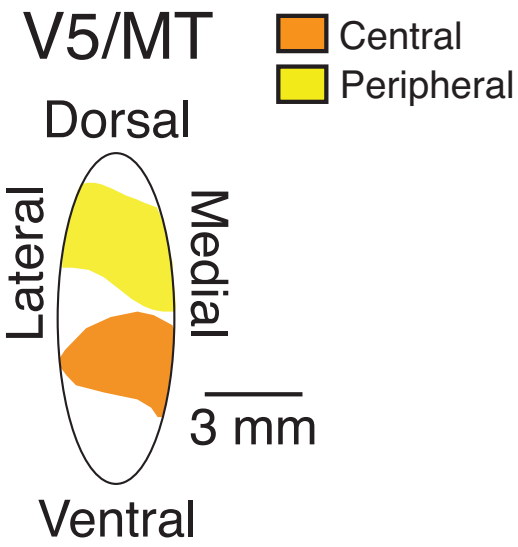

Figure 3.5: Summary diagram of expected visual topography in V5/MT, redrawn from Van Essen et al. (1981, Fig.12). Van Essen study mapped eccentricity data from electrophysiological recordings in V5/MT, and plotted the data onto the standardized map of V5/MT. Orange shaded areas shows region of V5/MT representing central 0-11° visual field, yellow shows (≥12°) peripheral visual field.

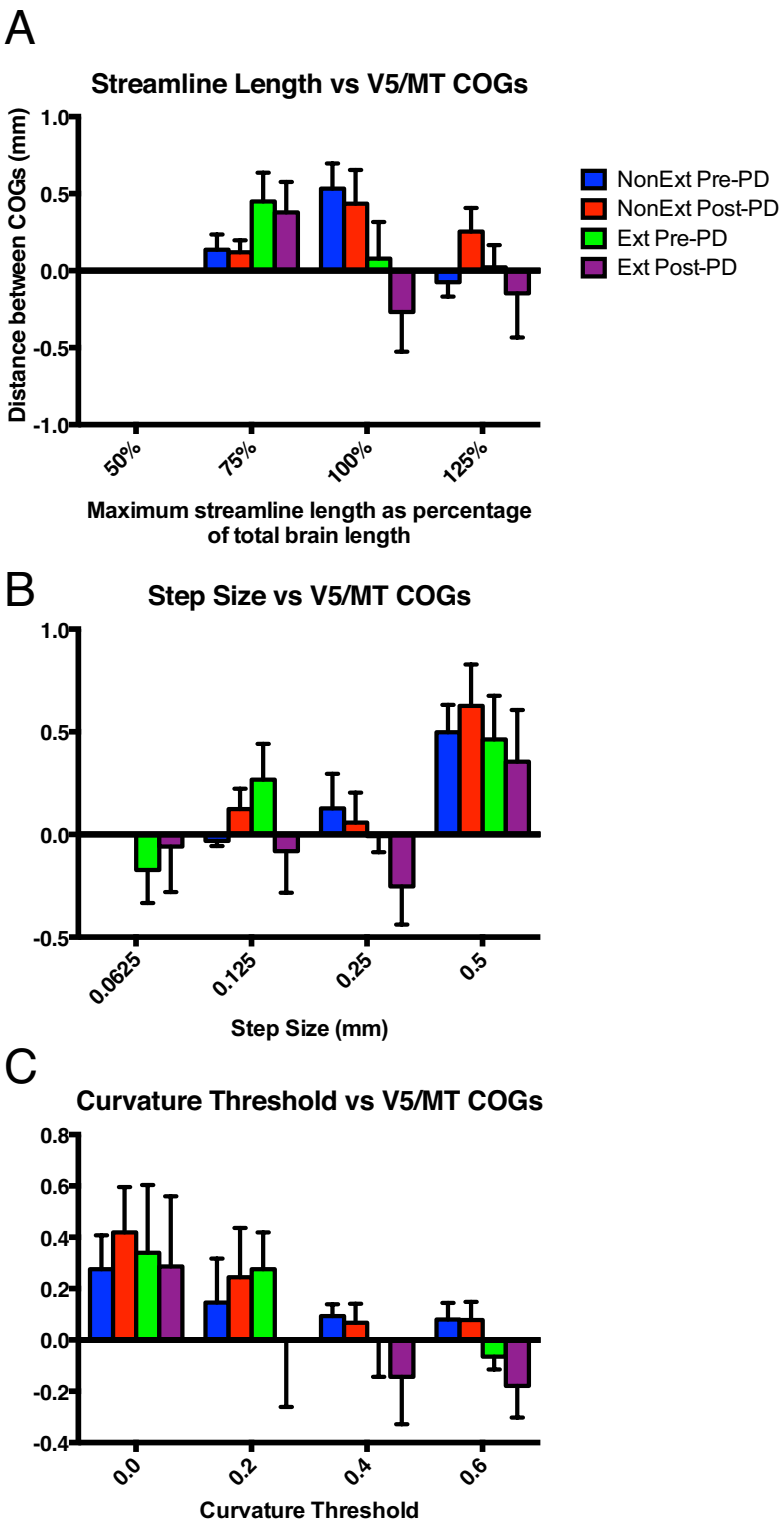

Figure 3.6: Graphs of the effect of **(A)** maximum streamline length, **(B)** step size, and **(C)** curvature threshold on the distance between central and peripheral centres of gravity (COGs) of V5/MT predicted topographic maps. Mean accuracy is computed for each condition for a given parameter value pooled across all other values. Error bars are SEM.

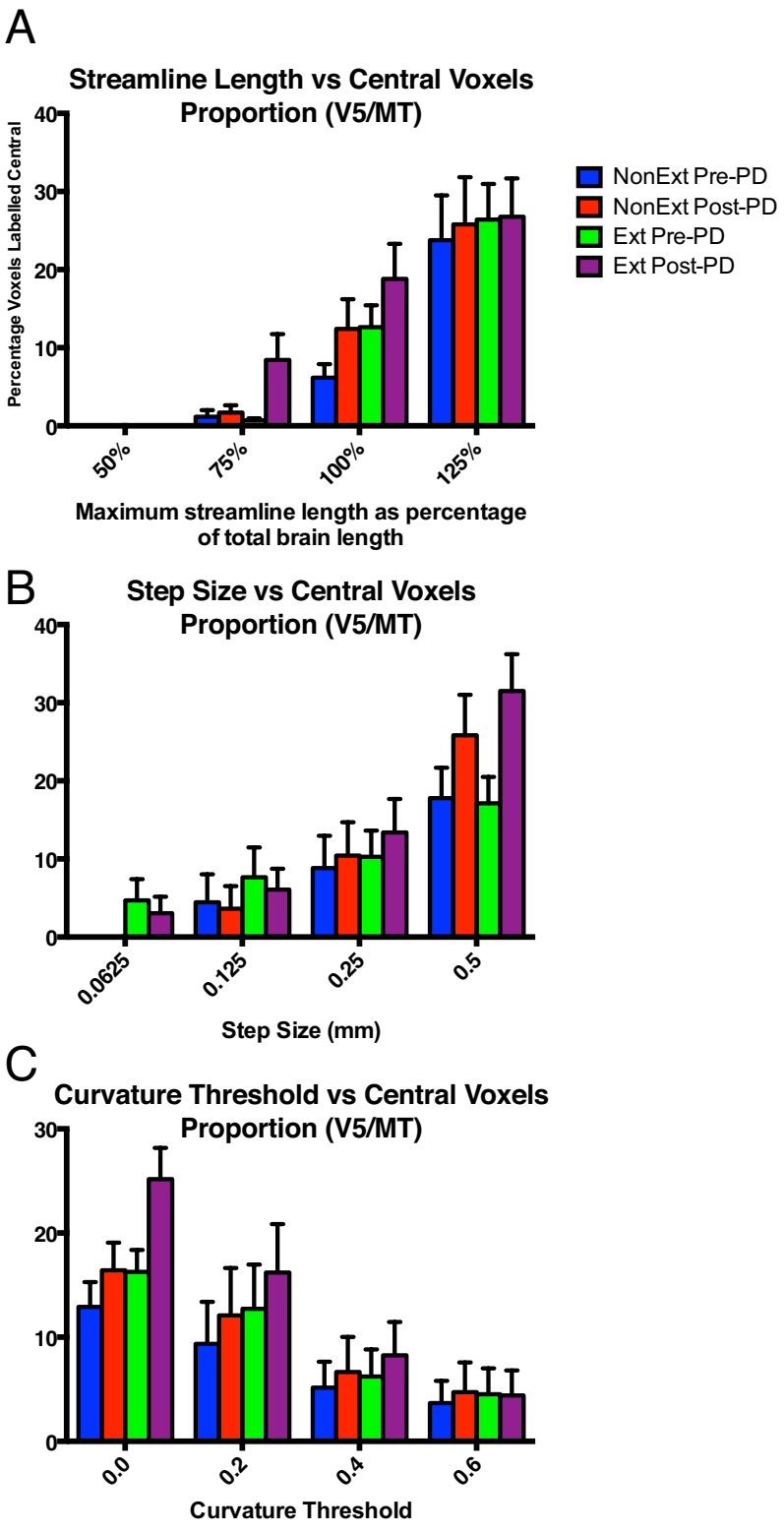

Figure 3.7: Graphs of the effect of **(A)** maximum streamline length, **(B)** step size, and **(C)** curvature threshold, on proportion of central voxels in the predicted V5/MT topographic map. Mean accuracy is computed for each condition for a given parameter value pooled across all others. Error bars are SEM.

The results indicate that when using cortical, non-extended targets, the distance between COGs is greatest when the number of steps limits streamline length to 100% of the brain length (Fig. 3.6A). However, when using extended targets, the distance between COGs is greatest when the number of steps represented 75% streamline length. When increasing the maximum streamline length to 100% and 125% brain length, for some conditions the centres of gravity were spatially inverted to what would be expected based on V5/MT electrophysiology, and suggest that the higher maximum streamline length permitted more spurious tracts to be included. The discrepancy between non-extended targets and extended targets is likely to be due to the fact that cortical, non-extended targets represent an increase in distance away from the seed compared with extended targets. Thus, the optimal maximum streamline length will vary according to the target type used. A maximum streamline length of 50% is too short to reach V1, and results in a failed segmentation (Fig. 3.6A).

There is a clear difference in COG distance when using 0.5 mm steps for all different target and processing conditions, while on average the segmentation fails for all other step sizes (Fig. 3.6B). The results also show that on average a curvature threshold of 0.0 results in the greatest distance between COGs, and there is a clear decline in segmentation quality as the curvature threshold increases (Fig. 3.6C).

Based on Van Essen et al.'s study (1981), we would expect the proportion of central voxels to be around 50%. A step size of 0.5 mm and curvature thresholds of 0.0 on gives on average the highest proportion of centrally classified voxels, however, neither result in a proportion greater than 35% in any of the target/processing conditions. This is likely to be due to the fact data is pooled over all other parameter values, and many of these other parameters result in failed segmentations. Although the 125% streamline length value results in the highest proportion of central voxels on average, the finding that this value results in poor spatial COG separations compared to lower streamline length values, indicates that there is an increase in central voxels but that these are located in regions we would not expect to find them.

Condition	Max. Streamline Length	Step Size	Curvature	COG Distance
NonExt Pre-PD	100%	0.25 mm	0.2	2.75
NonExt Post-PD	100%	0.5 mm	0.0	2.69
Ext Pre-PD	100%	0.125 mm	0.0	3.03
Ext Post-PD	75%	0.5 mm	0.2	2.72

Table 3.3: Parameter combination with the greatest distance between COGs (in millimetres) of predicted topography for each condition.

Although the results in Table 3.3 indicate that the optimal tractography parameters might range more widely than 75%, 0.5 mm step size, and 0.0 curvature threshold, this combination of parameters, identified earlier in this chapter as optimal for predicting LGN topography, always results in one of the highest separations between COGs. Based on this finding and the results presented above, and in order to maintain consistency between tractography sessions seeded from LGN and those from V5/MT, it was decided that these would represent the ideal tractography parameters to use throughout the rest of the study. Given that these results are for a single hemisphere only, the overall effects of extended targets and probability density normalization were compared across all hemispheres in the next section.

3.3.4 Effect of extended target masks and probability density normalization on V5/MT tractography

The proportion of labelled central and peripheral voxels were computed for all post mortem central-peripheral segmentations of V5/MT using fixed tractography parameters (75% maximum streamline length, 0.5 mm steps, 0.0 curvature). The distance in millimetres between the centres of gravity for centrally classified and peripherally classified voxels was also computed for each hemisphere.

	% Voxels Cent	% Voxels Peri	COG Distance
Cortical Target: Pre-PDF (No smoothing)	15.8 (16.7)	84.2 (16.7)	0.87 (2.43)
Extended Target: Pre-PDF (No smoothing)	2.1 (3.9)	97.9 (3.9)	0.90 (2.23)
Cortical Target: Pre-PDF (With smoothing)	9.3 (15.3)	90.7 (15.3)	0.87 (2.84)
Extended Target: Pre-PDF (With smoothing)	1.2 (3.0)	98.8 (3.0)	-0.14 (0.47)
Cortical Target: Post-PDF	42.3 (15.3)	57.7 (15.3)	2.38 (1.41)
Extended Target: Post-PDF	48.1 (15.3)	51.9 (15.3)	3.05 (1.76)

Table 3.4: Comparison of the effect of target type and probability density normalization on the proportions of centrally classified voxels, peripherally classified voxles, and distance between COGs of predicted topography. 75% maximum streamline length, 0.5 mm steps, 0.0 curvature threshold. ± Standard deviations in parenthesis (n =12).

A 2 x 3 within subjects ANOVA on the distance between centres of gravity revealed no significant effect of target type (Extended vs cortical targets, $F(1,11) = 0.03$, $p = 0.87$), but there was a significant effect of processing type (Pre-PDF no smoothing vs. Pre-PDF with smoothing vs Post-PDF, $F(2,22) = 11.33$, $p < 0.001$). There was no significant interaction ($F(2,22) = 2.82$, $p = 0.08$). Bonferroni corrected pairwise comparisons for processing type show no significant difference between Pre-PDF no smoothing and Pre-PDF with smoothing conditions ($p = 1.00$). The difference between the Pre-PDF no smoothing condition and Post-PDF condition was significant ($p = 0.024$), as was the difference between the Pre-PDF with smoothing condition and the Post-PDF condition ($p = 0.001$). Bonferroni corrected pairwise comparisons were also carried out for extended targets vs. cortical targets for each processing condition (Pre-PDF no smoothing, Pre-PDF with smoothing, and Post-PDF). None of these pairwise comparisons were significant.

Bonferroni corrected pairwise comparisons (alpha level $0.05/9 = 0.0056$) on the proportion of central voxels showed that significantly more voxels were classified as central when using extended targets vs. cortical targets Post-PDF ($p = 0.004$), but no significant differences in proportion of central voxels between extended targets vs. cortical targets, neither Pre-PDF no smoothing ($p = 0.01$) nor Pre-PDF with smoothing ($p = 0.09$). Thus, when probability density normalization is applied, using extended targets masks over cortical target masks results in a significantly higher proportion of centrally classified voxels, which more closely matches the proportion of central voxels we would expect from Van Essen et al.'s study (1981).

The results indicate that when probability density normalization is applied there is an increase in central voxels using extended target masks, however, there is no significant difference in COG distance for extended targets versus using cortical targets. The spatial smoothing step has no significant effect on the COG distance.

3.4 Discussion

The results suggest that the topography of both LGN and V5/MT seed regions is best predicted when probability density normalization is applied. Although there is no significant difference when using extended target masks, on average, using extended masks results in a more qualitatively realistic match between the LGN and the atlas, and perhaps increases the distance between V5/MT central-peripheral COGs. The match between the expected proportion of central voxels and the actual proportion of voxels in the predicted map is significantly better when using extended targets masks compared to using cortical targets for both LGN and V5/MT. This does not necessarily mean the predicted maps are better when using extended target masks, as the increase in central voxels may not necessarily be located in the correct location. However, the fact that there is a non-significant trend for the average LGN-atlas similarity to increase, and for the average V5/MT COG distance to increase when using extended targets, suggests that extended target masks improve predicted topographic maps but that this improvement does not reach significance, and furthermore that the improvement can be linked to the increase in the proportion of central voxels. Therefore on the basis of the results in this chapter, subsequent tractography sessions should be carried out using extended target masks, probability density normalization, maximum streamline length 75% brain length, step length 0.5 mm and 0.0 curvature threshold.

The finding that the probability density normalization was an effective way of improving the predicted topographic maps highlights the biases inherent in probabilistic tractography. Streamline counts are known to be biased in favour of larger targets and targets closer to the seed region (Behrens et al., 2003; Morris et al., 2008), yet there is no agreed upon method for dealing with these biases. FSL's probabilistic tractography algorithm includes an option for 'distance correction', in which the connectivity distribution becomes the length of the pathways that cross each voxel multiplied by the number of samples that cross it. It therefore represents the total distance streamlines travelled to reach the target (units =

voxels) and is a value that reflects both the probability of a connection and the total length of the streamlines that made it. However, because it's expressed in units of length, it is no longer a very meaningful biological measure, and no longer represents the probability of a connection, making comparisons of connectivity between regions meaningless. The authors of FSL's probabilistic tractography tools (Dr. Tim Behrens & Dr. Saad Jbabdi) agree that the distance-weighted solution has no reasonable interpretation or definition; nor was it intended to (JISCMAIL archives, FSL@JISCMAIL.ac.uk, https://www.jiscmail.ac.uk/cgi-bin/webadmin?A2=FSL;9fb9cff2.0805).

The probability density normalization procedure employed in this study represents a far more meaningful way of controlling for both distance and target size biases in probabilistic tractography that might bias streamlines to reach one target over another target. Its implementation should certainly be considered in future DWI studies looking at parcellating subregions based on connectivity to multiple targets.

The use of extended target masks in this study represents a second novel approach in using probabilistic tractography. As detailed in the Methods (Chapter 2, Extended target masks), it is based on a method developed by Liptrot et al. (2009) named ICE-T (Iterative Confidence Enhancement for Tractography). The ICE-T method overcomes the path-dependency (distance) problem by having an additional feedback loop stage of processing, after generation of an initial connectivity map, in which the seed region is grown through the aggregation of neighbouring voxels. This process is performed iteratively, tracking using the new region as a seed and is continued until the target is reached. The ICE-T method would not have been suitable for this study, as it still requires some initial streamlines to survive all the way from seed to target (which was not always the case, particularly for V5/MT seed voxels).

The important finding from the current study is that there was no significant difference in using extended target masks vs using cortical target masks on measures of predicted topographic map success (LGN-atlas similarity or on V5/MT COG spatial separation).

Thus, the assumption that *'reaching an intermediate voxel with a high probability of connection to the target is as good as reaching the target itself'*, can be considered a valid one. Furthermore, there is evidence to suggest that using extended target masks results in better-predicted topographic maps even though the quantification of this improvement is not significant. This evidence includes the qualitative assessment of the topographic maps, the closer match between expected proportion of central voxels and proportion in the topographic map, and the non-significant improvement in LGN-atlas similarity and V5/MT COG separation.

The conclusion of this is that extended target masks do not negatively affect the ability of DWI to detect corticocortical or thalamocortical topographic connections, and could potentially even improve this ability. The findings from the analysis of the effect of streamline length on predicting topographic maps showed that the effect is dependent on whether cortical targets are used (in which case a maximum streamline length 100% of the total brain length is optimal) or whether extended target masks are used (in which case 75% of the total brain length is optimal). This indicates that the effect of using extended targets masks is one of reducing the distance between the seed and the targets, and therefore may be beneficial in instances where boosting the tractographic signal is required for streamlines to reach target voxels. Although it could be argued that this could more simply be achieved by increasing the maximum permitted streamline length, allowing longer streamlines can potentially introduce more spurious tracts that might loop around implausibly to reach the target. The use of extended target masks ensures that only streamlines already on course to reach the target are boosted.

Overall, the results presented in this chapter indicate that the ability of DWI and probabilistic tractography to detect topographic connections can be improved when using probability density normalization, and there is evidence to suggest it can also be improved when using extended target masks. The maximum permitted streamline length also has a significant effect on the predicted topographic maps, as stopping streamlines short result in failed segmentations, yet allowing excessively long streamlines also decreases the accuracy

of the predicted maps. This is a finding that appears to be undeclared in the literature. The effects of step size and curvature threshold are more detailed in the literature (Parizel et al., 2007; Tournier et al., 2002; Tournier et al., 2011; Côté et al., 2013; Takemura et al., 2016). These studies usually explore the effect of step size and curvature on simulated data. The analyses presented in this chapter show the effects of these parameters on real data. I find here that a 0.5 mm step size and 0.0 curvature threshold results in better predicted topographic maps. This matches the literature suggesting that step sizes matching the voxel size are more likely to reflect the ground truth (Tournier et al., 2011), and the literature suggesting that lower curvature threshold values allow more and longer fibres to reach targets (Parizel et al., 2007). These values therefore represent appropriate values to use for future analysis on DWI and probabilistic tractography.

Chapter 4

Post mortem DWI and probabilistic tractography of the macaque LGN

4.1 Introduction

The lateral geniculate nucleus (LGN) is an anatomically distinct region of the thalamus and serves as the main relay for visual information from the eye to visual cortex. The LGN is innervated by the optic tract which is formed from the retinal ganglion cell axons of both eyes, and sends projections through the optic radiation to the primary visual cortex (V1) in the ipsilateral occipital lobe (Casagrande & Kaas, 1994). In primates, the LGN consists of six distinct layers of cell bodies with layers of neuropil and some neurons in between. The first two layers are magnocellular layers, innervated by magnocellular ganglion cells in the retina, so called because of their larger cell body (Perry et al., 1984). LGN layers three though six are parvocellular layers, receiving projections from retinal parvocellular cells. These magnocellular and parvocellular pathways form distinct projections from the retina (Conley & Fitzpatrick, 1989), remain segregated within the LGN (Michael, 1988) and appear to remain distinct from the LGN to V1. The magnocellular projection terminates primarily in V1 layer 4Cα, while the parvocellular projection terminates in

layers 4A and 4Cβ (Fitzpatrick et al., 1985). In between these 6 layers, neurons are thought to belong to the more recently defined koniocellular pathway (Casagrande, 1994; Hendry & Yoshioka, 1994). In the macaque, the axons from ventral K1-K2 koniocellular layers terminate in cortical layers 1 and 3A, whereas axons from the dorsal K3-K6 koniocellular layers terminate primarily in layer 3Bα (Casagrande et al., 2007). Each LGN receives only information from the contralateral visual field, and has a retinotopic organization such that neighbouring regions of visual space are represented by neighbouring neurons.

The connectivity and retinotopy of cortical and subcortical visual structures is defined in non-human primates (NHPs) using histological (Zeki, 1976; Connolly & Van Essen, 1984;) and electrophysiological techniques (Gur et al., 1997; Malpeli & Baker, 1975; Malpeli et al., 1996; Merigan & Maunsell, 1990; Nealey & Maunsell, 1994). These 'gold standard' techniques have shown that the primate visual system is organised in a highly topological manner. By contrast, magnetic resonance (MR) techniques tend to lack the spatial resolution required to uncover topological representations in small component structures of the visual system such as the LGN. However, the disadvantages of histological techniques are that they unsuitable for *in vivo* or intact brain preparations, and that *in vivo* electrophysiology is both challenging and invasive. Furthermore, these techniques are often unable to visualise the gross anatomical trajectories of visual pathways. As such, the retinotopic organisation of the LGN and its connections has so far been largely overlooked in primate functional MRI studies, in large part due to spatial limitations of fMRI resolution for small, subcortical nuclei. The LGN often appears as an undifferentiated grey mass of cells with the blood-oxygen level dependent (BOLD) response typically averaged over the entire structure.

As described in Chapter 2, diffusion-weighted imaging (DWI) and tractography (Le Bihan et al., 1986; Basser et al., 2000), provides a non-invasive methodology of revealing topological connections. Previously, tractography has been used to identify functionally meaningful subdivisions of the thalamic grey matter from thalamocortical connections (Behrens et al., 2003a). Similarly, DWI has been used to map projections of the corpus

callosum in humans, where fibres in the splenium projecting from one hemisphere to the other were found to be organized topographically with respect to their representations of visual space (Dougherty et al., 2005; Saenz & Fine, 2010). Such ordered connectivity between separate brain regions provides the substrate for information transfer between them (Kaas, 1997; Jbabdi et al., 2013). Thus, the function of one area can be inferred from its connections to another using DWI.

Building on these findings, in this chapter I investigate the visual topological pattern of connections in the Rhesus macaque (*Macaca mulatta*) between the LGN and V1. The connection between these regions is suitable for testing as there is a large tract of white-matter (the optic radiation) from the LGN to V1 that is easy to trace tractographically, while both regions have a well-known retinotopic organisation. I tested this by predicting coarse maps of the visual eccentricity and elevation in LGN from estimates of its connections to different parts of V1. I also predicted the relative number of LGN-V1 connections in separate magnocellular and parvocellular pathways. It was previously thought that DWI lacked the resolution to carry out analysis of topographical maps in the LGN, and such mapping has not yet been achieved non-invasively with DWI. To overcome the limitations of image resolution and data quality in depicting small structures such as a the LGN, I use high-resolution, high signal-to-noise ratio DWI datasets to investigate whether DWI with probabilistic tractography is sensitive and accurate enough to uncover preserved topological relationships in the anatomical connections between the LGN and V1.

4.2 Methods

The methods follow those detailed in the methods chapter (Chapter 2). In brief, six adult macaques (*Macaca mulatta*) yielding 12 hemispheres were included in this analysis – three females (M124x, M128x, and M129x) and three males (M126x, M127x, and M130x). The six macaques were perfusion-fixated transcardially, and the brains removed for diffusion imaging at Tim Dyrby's lab in Copenhagen, Denmark (DRCMR).

Probabilistic tractography was carried out on the DWI datasets, seeding from the LGN and targeting separate V1 target regions individually. The V1 target regions were extended target masks of V1 regions representing central, peripheral, inferior, and superior visual field regions individually (see Chapter 2, *Extended Target Masks*). After tractography was carried out, streamline counts in the seed voxels were probability density normalized (see Chapter 2, *Predicting the visual topography of seed areas*). Seed voxels were then labelled according to the target that gave it the highest probability density for a given target pair (central/peripheral or inferior/superior). To evaluate the accuracy of labelled voxels, the seed voxels were registered to a high-resolution digital atlas of the Rhesus LGN (Erwin et al., 1999), and the percentage of correctly classified voxels was found in each subregion of the atlas. A 3D rendering of this LGN atlas was created using FSLView3D and is shown in Figure 4.1 to illustrate the different representations of the visual field.

In the analysis of the connectivity of different subregions of the LGN (magnocellular and parvocellular components), separate masks were made for each of these subregions, and tractography carried out to central and peripheral V1 extended target masks. The relative number of connections between the LGN subcomponents and V1 targets was compared using a connectivity probability index (see Chapter 2, *Connectivity probability index*).

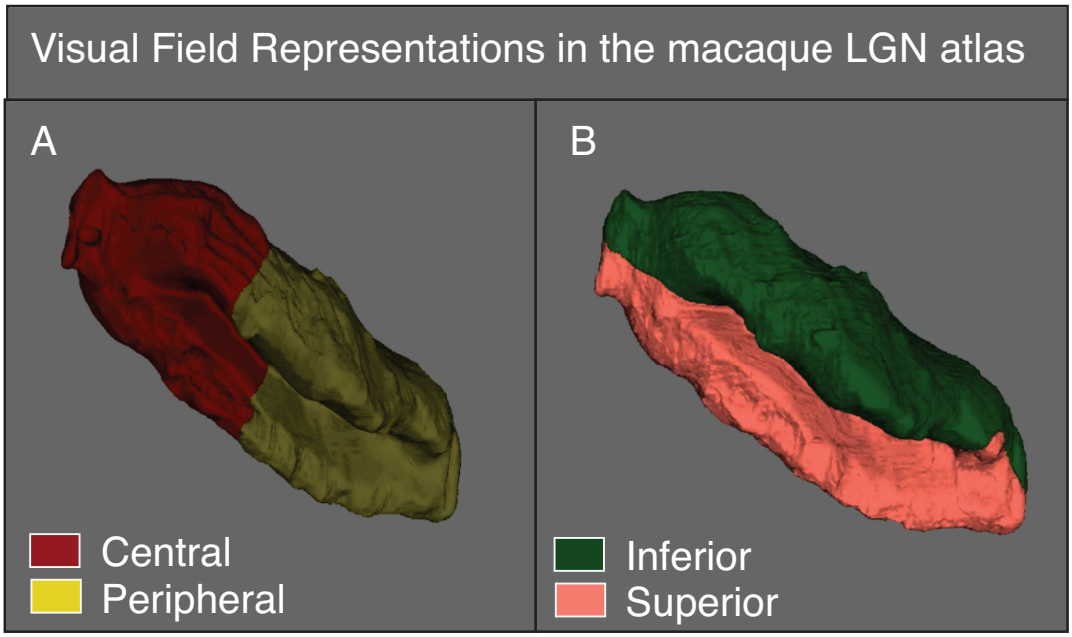

Figure 4.1: **3D rendering of LGN atlas showing different visual field representations.** Atlas reconstructed from Erwin et al. (1999) digital atlas of the LGN mapped at 25 µm isotropic voxel resolution. The atlas is based on a single left hemisphere LGN mapped with a combination of histological and electrophysiological techniques. The LGN atlas was divided into two pairs of distinct regions representing different parts of the visual field. (A) Shows the central 0-11° in red and the peripheral ≥12° in yellow. (B) Shows the region representing the visual field below the horizontal meridian (inferior visual field) in green, and the upper visual field (superior) in pink. This provided the benchmark against which the predicted tractography-derived maps of LGN could be compared.

4.3 Results

4.3.1 Mapping visual elevation topography in the LGN based on *post mortem* tractography to V1

First, I investigated whether the visual topographic organisation of geniculocortical connections was captured in the *post mortem* DWI by predicting the visual elevation topography of LGN (Fig. 4.2). Tractography was conducted separately for each hemisphere and V1 target; LGN was seeded, and streamlines targeted either the superior or inferior portion of ipsilateral V1. The probability density of a streamline (see Chapter 2, *Predicting the visual topography of seed areas*) hitting either target was then computed, and the visual mapping of each LGN voxel was determined by which target was most likely. The result was a coarse prediction of the visual elevation map for each LGN (Figs. 4.2-4.4).

These maps, based on connectivity to V1, revealed two clearly distinct subregions of LGN that mapped the superior and inferior visual field to LGN voxels in accordance with a high-resolution, digital atlas of the macaque LGN (Erwin et al., 1999). Figure 4.2 shows the maps for an example brain, in which the dorsal-medial half of LGN represented the inferior visual field (green), and the ventral-lateral half of LGN represented the superior visual field (pink). The border occupied a central position where the horizontal meridian line is expected (atlas).

A slice-by-slice examination in Figure 4.3 shows that the pattern and relative volumes of the topographical prediction matched well with the digital macaque LGN atlas throughout LGN. In particular, there was a smooth transition of the visual topographic map from the middle of LGN to the edges. This pattern of organization was highly consistent in all three stereotactic planes, and across all 12 hemispheres that were analysed (Fig. 4.4).

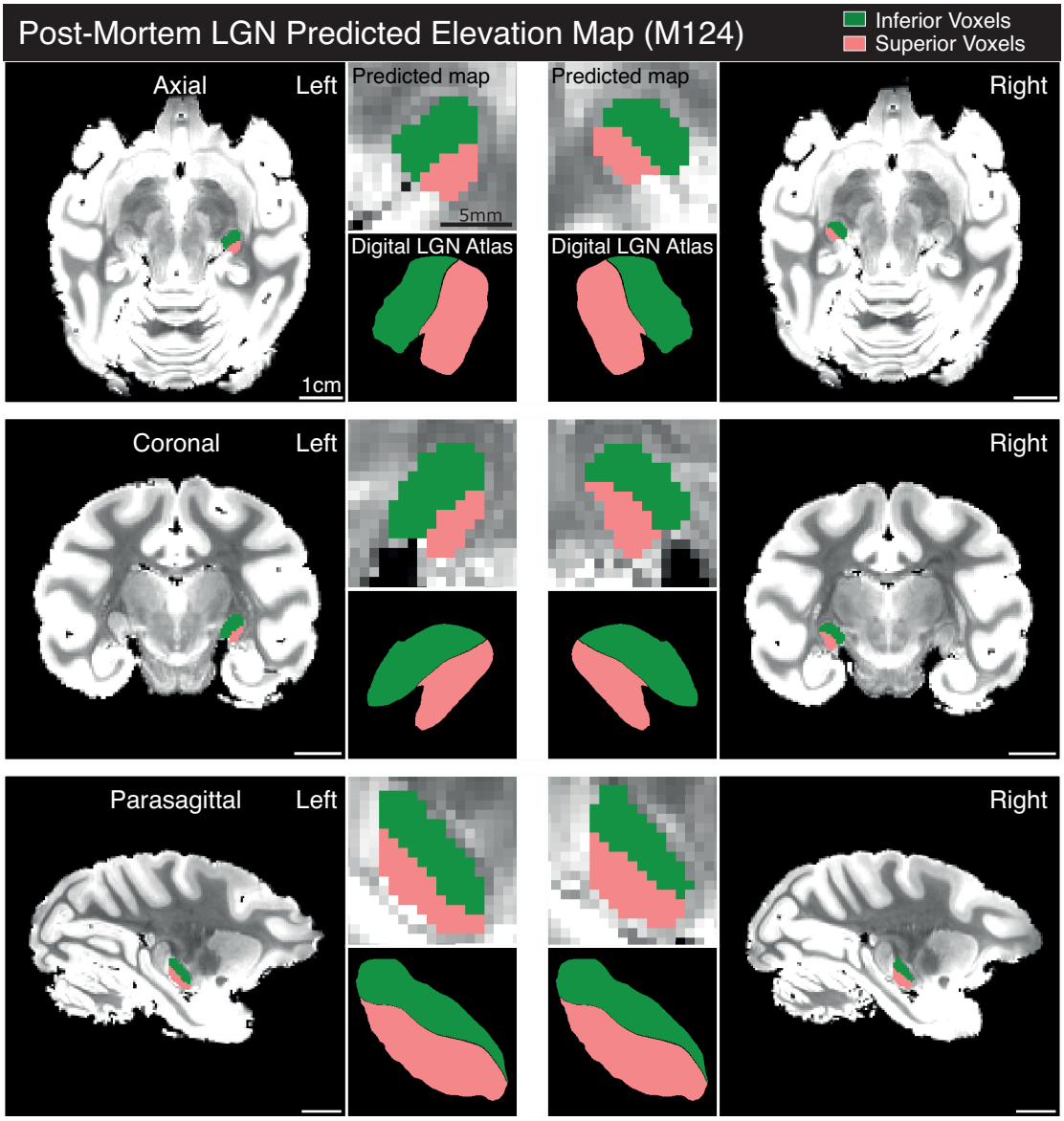

Figure 4.2: **LGN elevation topography.** The elevation maps for the LGN of brain M124 was predicted based on connectivity to superior and inferior visual field representations in V1. Full brain and magnified views show the midpoint slices of the LGN in each stereotactic plane (rows), compared with corresponding midpoint slices the LGN atlas (Erwin et al.,1999). Colours show the visual field representation in each map (inferior visual field, green; superior, pink). White scale bars are 1cm, black scale bars at 5mm.

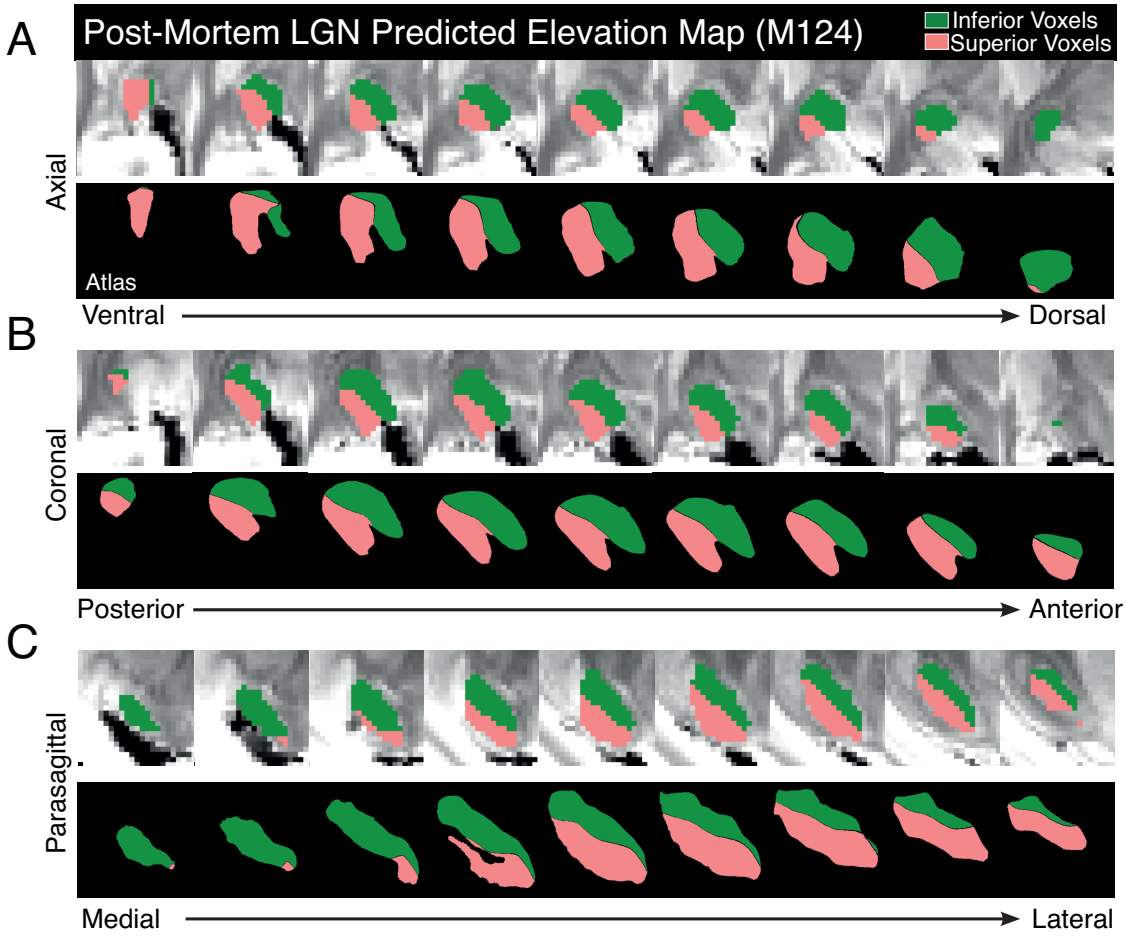

Figure 4.3: **Slice-by-slice examination of LGN elevation map for a single LGN.** The predicted map (M124, right) is shown above corresponding slices in the LGN atlas (Erwin et al., 1999) for the axial **(A)**, coronal **(B)**, and sagittal **(C)** planes of view. Colours are as in Figure 4.2.

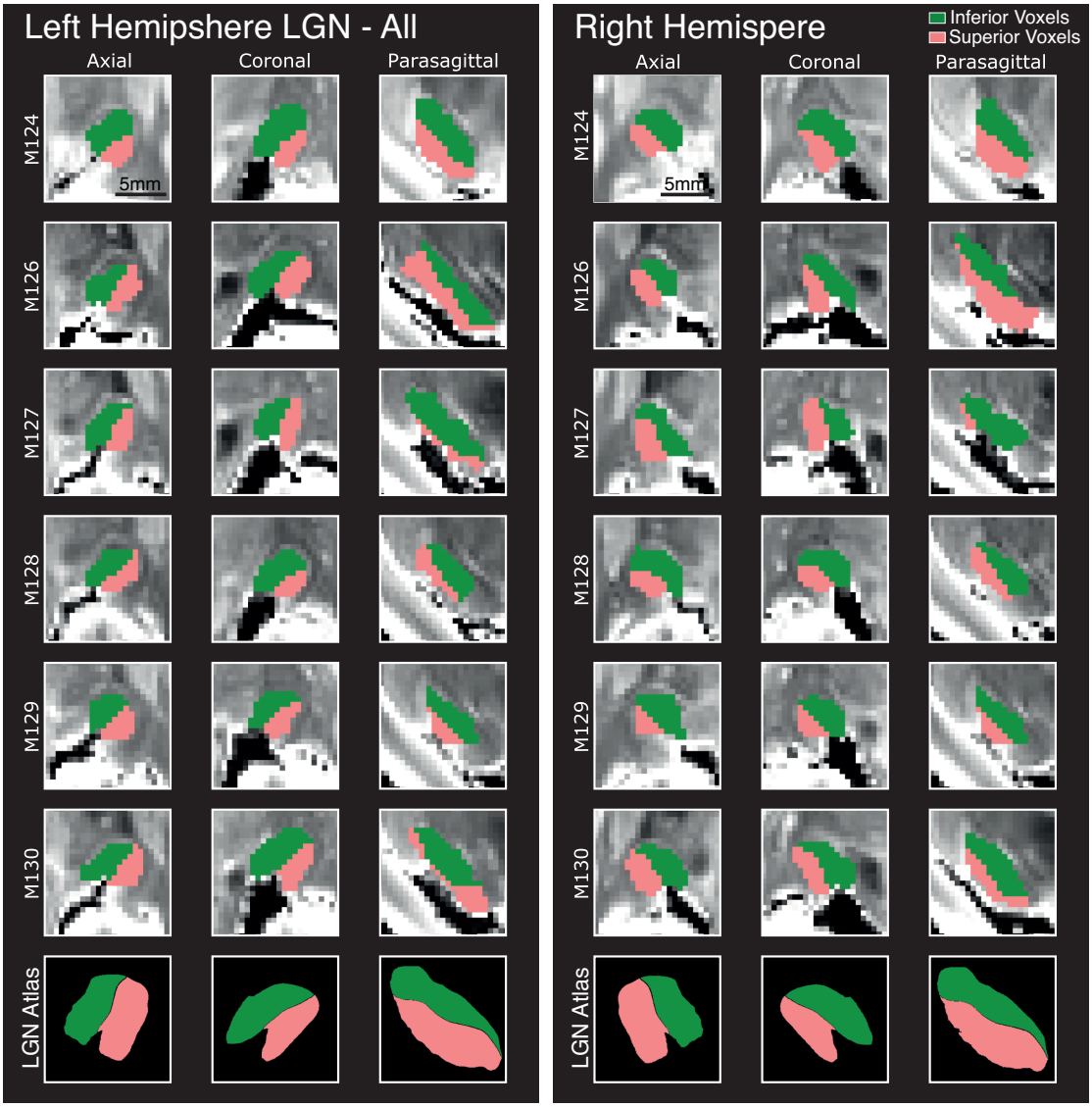

Figure 4.4: **Predicted LGN elevation maps for all hemispheres (n = 12).** Midpoint slices through the LGN are shown for each brain (rows), stereotactic plane of view (columns), and all hemispheres analysed. The bottom row shows corresponding points in the LGN atlas (Erwin et al., 1999). Colours are as in Figure 4.2. All hemispheres show two distinct clusters of inferior classified voxels (green) and superior classified voxels (pink), whose relative locations and volumes match well with the digital LGN atlas.

4.3.2 Mapping visual eccentricity topography in the LGN based on *post mortem* tractography to V1

Next, I sought to predict the eccentricity topography of LGN based on tractography to V1. The eccentricity topography of LGN maps along an orthogonal axis to elevation. The central and peripheral visual field representations of V1 were targeted in separate tractography sessions that were seeded from the LGN. Again, the predicted maps contained two distinct regions. Figure 4.5 shows one example brain, in which the lateral-posterior portion of LGN mapped the central visual field (orange), and the medial-anterior portion mapped the periphery (yellow). Though not as consistent as the elevation maps, the relative positions of these areas generally agreed with the LGN atlas across most hemispheres (Fig. 4.6). However, in some hemispheres (e.g. M124 left) the prediction did not fully match the LGN atlas, particularly in the parasagittal plane (e.g. Fig. 4.5 left; Fig. 4.6. M124, M128, M129).

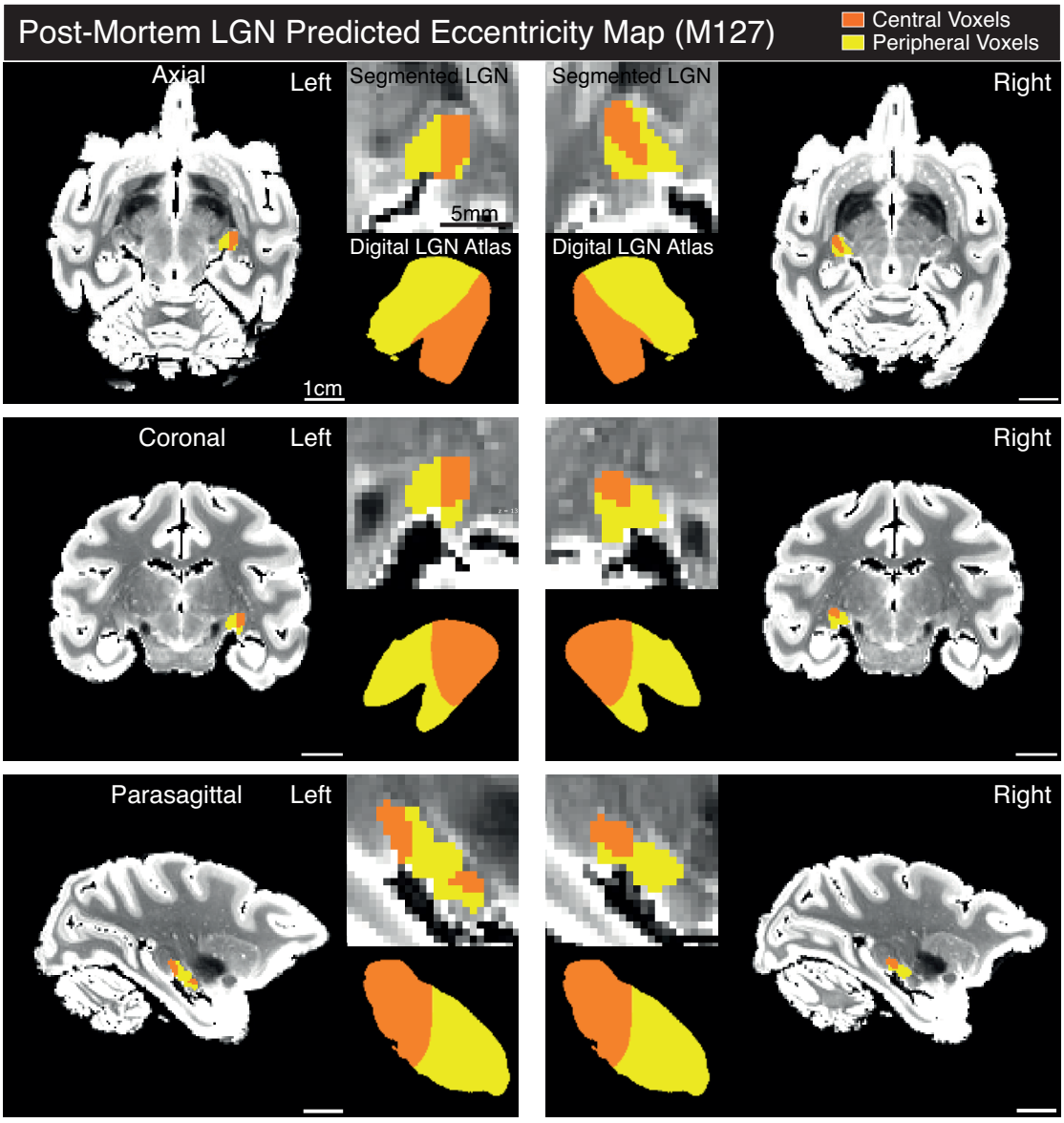

Figure 4.5: **LGN eccentricity topography.** Complementary figure to Figure 4.2, mapping eccentricity instead of elevation. Orange indicates the central visual field representation, and yellow indicates the peripheral visual field representation. Two distinct regions of classified voxels can identified with the lateral-posterior portion of LGN mapping the central visual field (orange), and the medial-anterior portion mapping the periphery (yellow). This spatial organization matches well with the LGN atlas (Erwin et al., 1999).

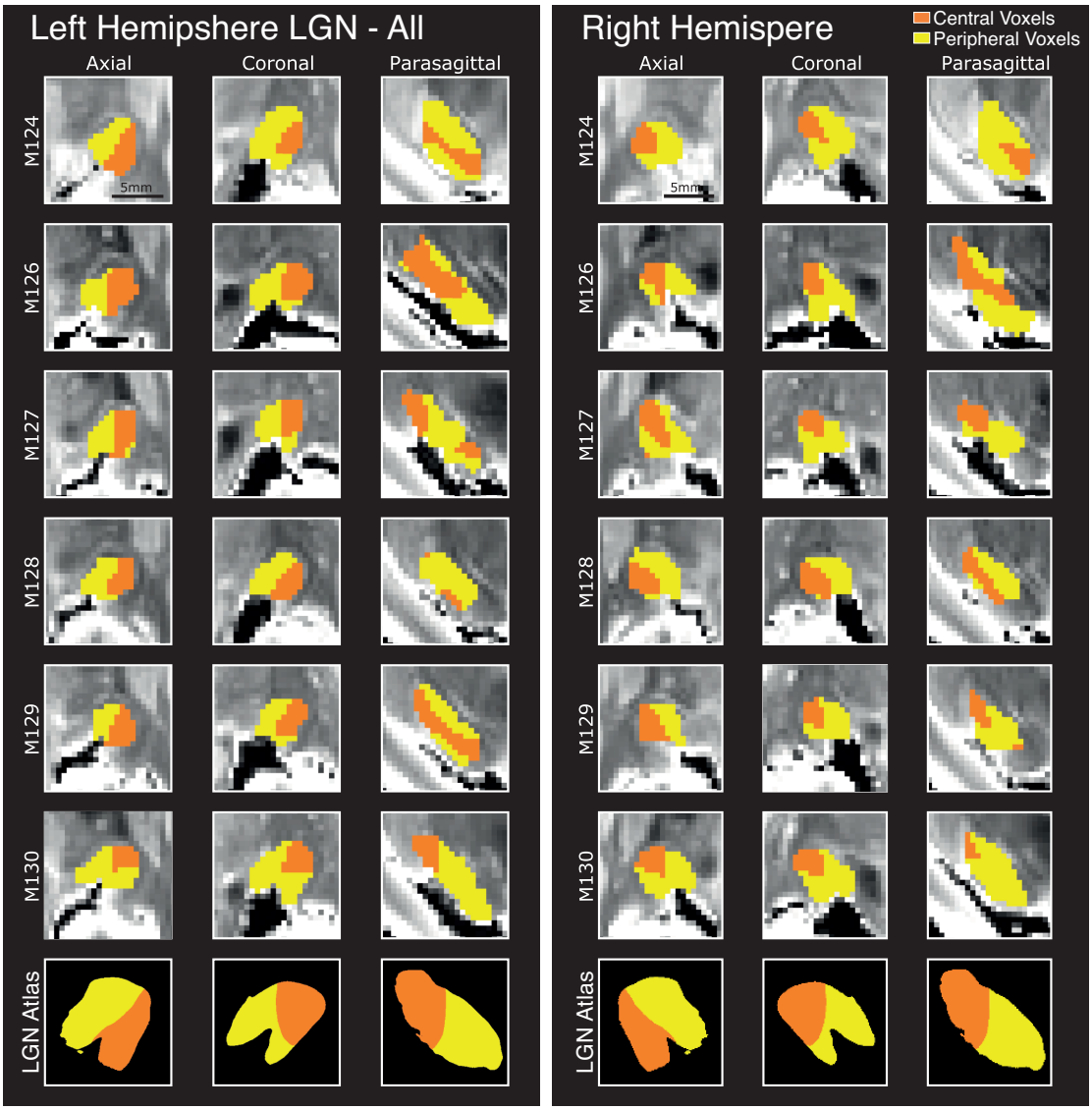

Figure 4.6: **Predicted LGN eccentricity maps for all hemispheres (n = 12).** The same layout as Figure 4.4, but colours are as in Figure 4.5 with central representations in orange and peripheral in yellow. Two distinct regions of voxels in the predicted maps are clearly identified. Their relative locations match the atlas for most hemispheres in the axial and coronal planes, however, the predicted maps do not fully match the atlas when viewed in the parasagittal plane for some hemispheres (e.g. M124, M128, M129).

4.3.3 Quantifying predicted LGN topographies based on tractography

The topographic predictions were difficult to validate overall by eye, because the result depended on the plane of view, particularly for the central-peripheral topographic maps. Therefore, the accuracy of the maps was quantified by first registering them onto an LGN atlas, then making a voxel-wise comparison. Each visual division of the atlas was examined separately (central, peripheral, inferior, and superior) to find the percentage of each predicted map that was correct (Fig. 4.7A). The predictions were generally good. That is, the percentage similarity between the classified voxels of the LGN and the LGN atlas, was above chance (assuming 50%) in the central (mean = 58.1% [SD ± 8.8], one sample t-test, $p = 0.008$), peripheral (mean = 77.1% [10.7], $p < 0.001$), inferior (mean = 92.0% [4.7], $p < 0.001$), and superior (mean = 75.2% [13.0], $p < 0.001$) portions of LGN. Overall, the predicted elevation maps were more accurate (mean % correct = 83.1% [8.2]) than the eccentricity maps (mean % correct = 67.7% [13.7]; paired t-test, $p < 0.001$).

However, the maps also contained errors. Aside from resolution and registration problems caused by the imperfect registration of the topographic map to the LGN atlas space, there could be two possible reasons for errors in the predicted maps. Either the predicted spatial arrangement of the voxels was wrong, or one part of the map was underestimated. To check the latter possibility, examination of the LGN topographic maps found that, on average, 38.27% (SD ± 4.48) of LGN mapped the central visual field, 61.73% (4.48) was peripheral, 40.13% (5.38) was superior, and 59.87% (5.38) was inferior. In contrast, 48.36% of the LGN atlas was mapped to central, 51.04% to peripheral, 50.52% to superior, and 48.59% to inferior visual field representations. Therefore, the predictions underestimated the central part of the LGN eccentricity map (mean predicted difference = 23.46%, atlas difference = 2.68%, t-test, $p < 0.001$) and the superior part of the elevation map (mean predicted difference = 19.75%, atlas difference = 1.93%, $p < 0.001$). Therefore, some of the apparent success in predicting the locations of peripheral and inferior LGN was due to overestimation.

To determine how well the overall arrangement was predicted, the whole volume of each predicted map was compared to the LGN atlas. On average, the predicted maps agreed with the atlas (mean correct percentage of volume = 75.3% [SD ± 11.5], one-way t-test, $p < 0.001$), although the elevation maps (mean = 83.1% [8.2]) were better predicted than the eccentricity maps (mean = 67.7% [13.7], paired t-test, $p < 0.001$). A random permutation test (see Chapter 2, *Randomised non-parametric tests*) provided the significance of each individual comparison. For 23 of 24 predicted topographic maps, the similarity between the predicted map and the atlas was significantly better than chance ($p < 0.05$) and only one hemisphere (M128x, left hemisphere, eccentricity map, 49.2%) was not ($p > 0.05$). These results suggest that DWI detected the general topographic organisation of LGN to V1 connections.

To determine the internal consistency of the predicted LGN topographic maps, a Leave-One-Out-Cross-Validation (LOOCV) analysis was carried out in which the topographic map from each hemisphere (the test set) was compared with a composite average of the predicted maps from all other hemispheres (the model set) registered to the same native space as the test hemisphere. The percentage of voxels similarly labelled between the test hemisphere and the model set was computed in the same way as described previously for the topographic maps vs. the digital LGN atlas. This process was repeated for each test hemisphere and the mean similarity between the test set and the model set computed for each type of topographic map segmentation (Central/Peripheral and Inferior/Superior; Fig. 4.7B). This cross-validation provides an estimate of the generalisation performance of predicted topographic maps generated by the DWI datasets and demonstrates the consistency within the experimental dataset. The results show that the percentage similarity for topographic maps within the datasets does not differ significantly from the percentage similarity computed for the topographic maps compared to the digital atlas (two-way ANOVA; topographic map type effect, $F(1,11) = 55.33$, $p < 0.001$; comparison type effect, $F(1,11) = 0.37$, $p = 0.56$; interaction, $F(1,11) = 0.32$, $p = 0.59$). The results indicate that the DWI datasets demonstrate a high level of consistency in the generation of topo-

graphic maps. The finding that the values obtained for the internal comparisons appear to mirror the digital atlas comparison might suggest that the less consistent results for the Central/Peripheral eccenctricity segmentations might be underlying the lower accuracy achieved in the digital atlas comparison for ecccentricity topographic maps compared to elevation topographic maps.

4.3.4 Connectivity of magno- and parvocellular LGN layers to V1

Malpeli et al. (1996; see also Azzopardi et al., 1999) proposed that the magnocellular and parvocellular pathways have different distributions of afferent fibers from LGN to different visual field representations in V1. Parvocellular afferents should be almost uniformly distributed throughout V1, while a smaller number of magnocellular afferents should increase in density with visual eccentricity. This study tested whether the *post mortem* DWI data could detect such differences by seeding streamlines from either the magnocellular or parvocellular layers of LGN, while targeting either the central or peripheral visual field representations in V1. The resulting streamline counts were normalised to estimate the probability of connections between LGN subcomponents to different regions of V1.

The connectivity probability index (see Chapter 2, *Connectivity probability index*) to both V1 targets was stronger when seeding from parvocellular LGN (mean parvocellular = 6.48, [SD ± 0.24]; mean magnocellular = 4.62 [0.95]; two-way ANOVA, LGN seed effect, $F(1,22) = 163.23$, $p < 0.001$), in agreement with the prediction that more parvocellular fibres reached V1 (Malpeli et al., 1996). However, the V1 targets received different numbers of streamlines from both the magno- and parvocellular LGN seeds (mixed two-way ANOVA, V1 target effect, $F(1,22) = 3191.59$, $p < 0.001$). More streamlines reached the closer peripheral V1 target (mean magnocellular index = 5.11, [0.57]; parvocellular = 6.63, [0.17]), than central V1 (magnocellular = 4.12, [1.02]; parvocellular = 6.33, [0.21]); paired t-tests, $p < 0.001$). But the magnitude of this difference depended on which part of LGN was seeded (two-way ANOVA, interaction, $F(1,22) = 5.871$, $p = 0.024$).

To compare the two pathways, Malpeli et al. calculated the ratio of magno- to parvocellular cell magnification at different eccentricities (replicated in part of Fig. 4.7C). The increased magno/parvo ratio at peripheral eccentricities suggested that more magnocellular LGN neurons had eccentric receptive fields. From their Figure 12, the magno/parvo ratio of cortical afferent density was also derived (Fig. 4.7C), which showed the same trend and suggests that a larger proportion of magnocellular afferents connected to peripheral V1. I calculated a similar relationship in the magno/parvo ratio of connectivity probability (average ratio; central V1 target = 0.018 [SD ± 0.03]; peripheral V1 = 0.047 [0.04]; paired t-test, $p < 0.001$; Fig. 4.7C). Although a greater absolute number of streamlines reached peripheral V1, this result shows that a greater number of magnocellular streamlines relative to parvocellular streamlines reached peripheral V1 than central V1, matching Malpeli et al.'s observation. Thus, the *post mortem* DWI from this study was able to resolve the topographic organisation of different functional streams in the geniculocortical visual pathway.

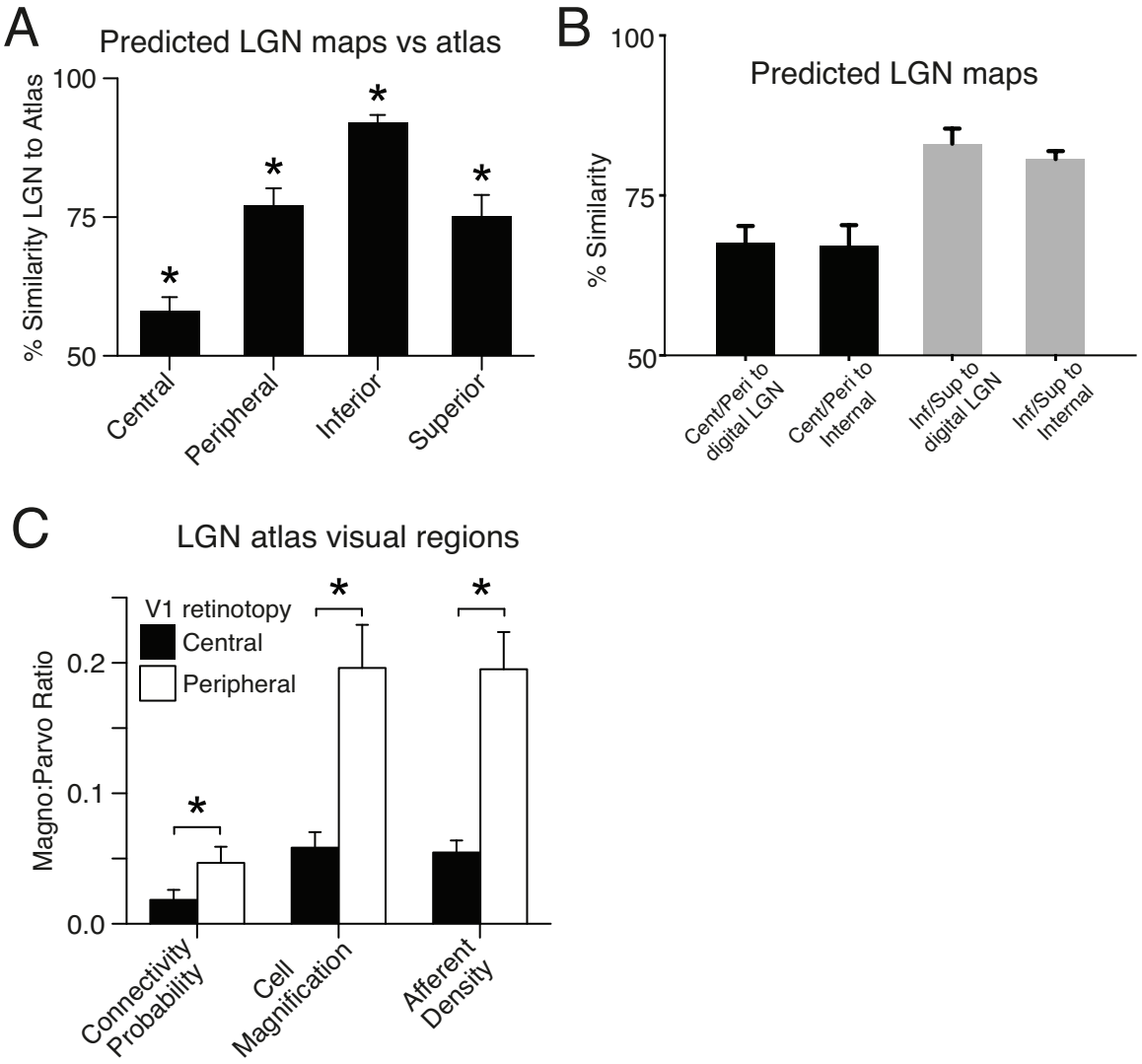

Figure 4.7: **Quantifying LGN map prediction accuracy based on probabilistic tractography to V1. (A)** The average percentage of the LGN atlas (Erwin et al., 1999) that was matched by the topographic predictions. This comparison was done separately for each visual division of the atlas: central visual field, peripheral, inferior, and superior. The results from each hemisphere were averaged together (n = 12). * denotes significance above 50% (t-test, p $<$ 0.01). **(B)** LGN map prediction accuracy measured by similarity to the digital LGN atlas and to a model atlas derived from an internal Leave-One-Out-Cross-Validation approach (n = 12). **(C)** LGN magnocellular over parvocellular ratios comparing raw connectivity probability, magnification factor, and LGN to V1 afferent density with respect to connectivity to different parts of V1 (central visual field, black; peripheral, white). Magnification factor and afferent density were derived from Malpeli et al. (Fig. 10 and 12). * significant difference (paired t-test, $p < 0.0167$). All error bars show standard error of the mean.

4.3.5 Topographically organised streamlines

To visualise the trajectory of streamlines travelling from LGN to V1, the density of streamlines was measured in each voxel by counting how many passed through. Density maps were made for each hemisphere and specific V1 target, and normalised by their peak value. All maps were registered to a standard space, and a threshold was applied to show voxels with the top 10% of densities. These areas of high streamline density are shown in Figure 4.8A.

When compared with the predicted LGN topographies (Figs. 4.4 & 4.6), it can be seen that streamlines generally maintained the same topographic arrangement en route to V1 as the part of V1 they connect to. For example, streamlines from ventral LGN that preferentially targeted superior V1 (Fig. 4.8A, pink) appeared to remain ventral of the streamlines from dorsal LGN that targeted inferior V1 (green). To illustrate this more clearly, the weighted average of the dorsal-ventral position of the streamlines from Figure 4.8A was computed, in each coronal slice (Fig. 4.8B); position was weighted by streamline density. From these data, it was found that streamlines connecting to inferior visual field representations in V1 were generally dorsal to superior connected streamlines (mean difference = 1.68 mm [SD $\pm$ 0.73 mm], t-test, $p < 0.001$). In contrast, the streamlines targeting central V1 (Fig. 4.8C, orange) appeared surrounded by those targeting peripheral V1 (yellow), though there was a weak trend for peripheral streamlines to be dorsal (mean difference = 0.41 mm [0.50 mm], $p < 0.003$; Fig. 4.8D). The close dorsal-ventral proximity might reflect the less clear arrangement for the LGN eccentricity maps observed for some hemispheres. These results suggest that the white matter tracts had a similar topographic organisation, and that the tracts connecting to central and peripheral V1 were more intermingled than the fibres connecting to inferior and superior visual field representations of V1.

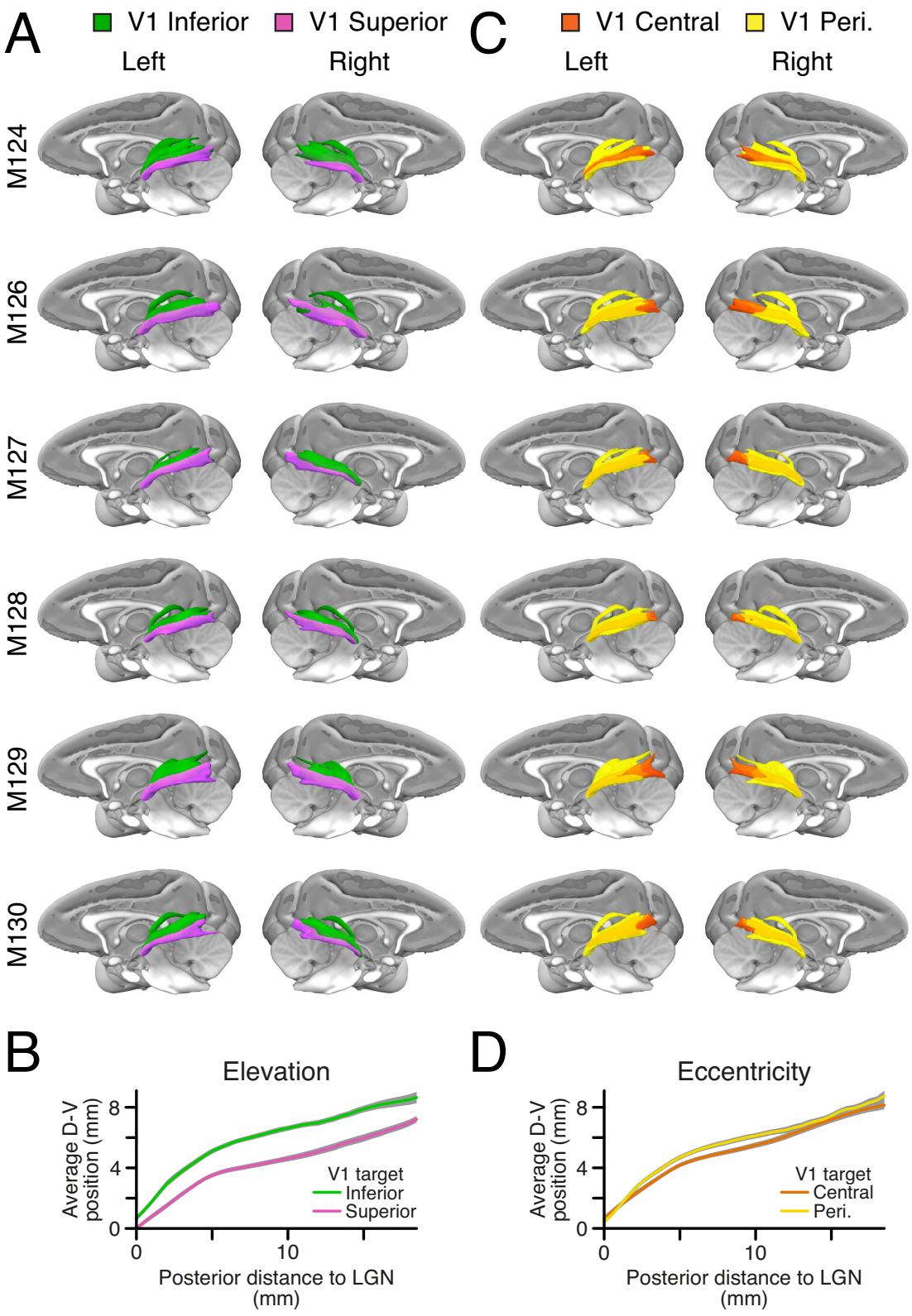
A
V1 Inferior
V1 Superior
Left
Right
C
V1 Central
V1 Peri.
Left
Right
M124
M126
M127
M128
M129
M130
B
Elevation
Average D-V position (mm)
8
4
0
0
10
Posterior distance to LGN (mm)
V1 target
Inferior
Superior
D
Eccentricity
Average D-V position (mm)
8
4
0
0
10
Posterior distance to LGN (mm)
V1 target
Central
Peri.

Figure 4.8: **Streamline density maps maintain topographic organisation. (A)** Streamline density for two sets of streamlines that were seeded in LGN and targeted either V1 inferior (green) or superior (pink). In all hemispheres the streamlines targeting inferior V1 generally run more dorsally than streamlines targeting superior V1. **(B)** Population average of the weighted average dorsal-ventral position of the streamlines targeting inferior and superior visual field V1 representations in A. **(C)** Same as A, but targeting V1 central (orange) or peripheral (yellow). In all hemispheres the streamlines targeting central V1 generally run in the centre of the white matte fibre bundle, with streamlines targeting peripheral V1 generally surrounding the central fibres, although there is considerable overlap. (D) Same as B, but using the streamlines in C. In A&B, 3D surfaces show the volume containing voxels with the top 10% of streamline density, created using Mr Cat software (Donders Institute, Nijmegen, Netherlands and University of Oxford, UK; Mars et al., 2015) and the MNI macaque brain atlas was used as a standard space to show the streamline density maps (McConnell Brain Imaging Centre, McGill University; Frey et al., 2011).

4.4 Discussion

Using diffusion-weighted imaging and probabilistic tractography on *post mortem* macaque datasets, this chapter shows that the LGN can be subdivided into two distinct subregions based on preferential connectivity to regions of V1 representing either inferior of superior visual field. The results presented show a pattern of organisation in which the dorsomedial region of LGN is preferentially connected to regions of V1 subserving inferior visual field (represented in the dorsal half V1), while ventrolateral LGN connects to superior visual field V1 (ventral half of V1). This pattern in highly consistent across all 12 *post mortem* hemispheres. The results in this chapter also show that the LGN can be subdivided into regions with differential connectivity to central and peripheral visual field V1 regions. The dorsal, posterior portion of the LGN has a higher connectivity with central V1, while ventral, medial and anterior portions of LGN connect preferentially to peripheral V1. The findings were verified qualitatively and quantitatively against functional retinotopic atlases of the LGN derived from electrophysiology (Erwin et al., 1999).

A further question addressed in this study was whether quantifiable predictions of connectivity could also be made for different functional LGN subcompartments (Magnocellular vs Parvocellular)? This is an important question in determining the spatial resolution limits of this technique. In the human and the monkey, the LGN is subdivided into magnocellular and parvocellular layers, and these layers have differential connectivity as you move from the central to the peripheral visual field (e.g. Clark, 1941). Using DWI, a change was observed in the magno/parvo connectivity ratio across V1, consistent with electrophysiological recordings (Malpeli et al. 1996). The study by Malpeli et al. (1996) also includes cell counts from their original study (Malpeli & Baker, 1975) and data from Connolly & Van Essen (1984) using retrograde tracers, showing that the ratio of magnocellular to parvocellular neurons was lowest in the LGN subregion subserving central vision.

The implication is that this ratio increases as a function of eccentricity. This finding was disputed by Livingstone and Hubel (1988) on the basis that errors were accumulated during the unfolding and remapping of the topography of the LGN in the Connolly & Van Essen study, resulting in inaccurate numbers for neuron density. However, a more recent study carried out by Azzopardi et al. (1999), also using retrograde labeling to determine the magno/parvo ratio, confirmed the findings from Malpeli et al. (1996) and Connolly & Van Essen (1984), that the magno/parvo ratio increases with eccentricity. Azzopardi et al. (1999) observed a mean ratio of 1:35 at the fovea and 1:5 at the periphery, similar to the ratios of 1:40 at the fovea and 1:4 at the periphery calculated by Connolly and Van Essen (1984). In our study, we observe a similar ratio of around 1:55 at the fovea and 1:20 at the periphery. Given that the density of retrogradely labeled neurons in the LGN is some combination of both the relative diameters of magnocellular and parvocellular terminal fields, and also their afferent density, it is impressive that DWI is able to make predictions of the LGN-V1 connectivity at similar levels of accuracy as neuronal tracing techniques. Exploring how the topography of magnocellular and parvocellular subcomponents varies across the visual field is important for understanding how the overrepresentation of central vision in the cortex is achieved (Azzopardi et al. 1999), and how different aspects of visual

information are made more explicit at different eccentricities. For example, additional parvocellular inputs to cortex could serve to enhance spatial phase encoding and therefore hyperacuity at the fovea, while the relatively higher magnocellular inputs in the periphery could serve to enhance coarse-grained movement information and make this information more explicit to higher-order visual areas involved in motion processing. While these ideas have been confirmed in previous animal studies, they have not been conclusively shown in humans. The purpose of the analyses in this chapter was to show that connectivity measures derived from DWI are highly comparable to those derived from gold standard techniques, and thus DWI represents an accurate technique capable of making quantifiable prediction of connectivity in primates, even for subregions of small structures such as the LGN.

A further goal of this study was to determine the trajectory of the pathway projections in the visual system. This investigation found evidence of a well-ordered topological projection from LGN to V1, such that LGN tracts to inferior and superior visual field V1 project, and remain well segregated all the way from LGN to V1 (Fig. 4.8). The topology of this connection is what permits the successful segmentation of LGN, and suggests that the axons are organized in the same way. Evidence for a preserved topology of connection between thalamic and cortical axons has previously been shown in rats using carbocyanine dyes during development (Molnar et al., 1998a), although the preserved topology in that study was not for within an area, but for different thalamic nuclei to different cortical areas. Topographic connectivity between the visual cortex and the LGN (via the thalamic reticular nucleus) has been demonstrated using anterograde Biocytin tracers in the rat brain (Lozsádi et al., 1996). Specifically, they showed that corticothalamic fibres representing similar elevations in the visual field run more or less parallel to each other on entering subcortical white matter. The topographic organization of optic radiation fibres has also been shown in the cat, using neuroanatomical tracers injected into the LGN (Nelson & LeVay, 1985). Interestingly, both of these studies found that there is a crossing over of fibres in the geniculocortical pathway. The retinotopic organization of the visual cortex

is often a mirror reversal of visual space, i.e. inferior visual field is represented dorsally and the peripheral visual field is represented medially. In order to maintain a preserved topology of connectivity, this means that some pathways will need to cross over, whereas others can be connected directly without a need for a crossing. Connolly and Van Essen (1984) first predicted that there should be a crossing over of geniculocortical fibres, as the topography of striate cortex is topologically inverted with respect to that of the LGN. They predict that this occurs in the inferior-superior axis, but accept that the inversion could be about the central-peripheral axis instead and not about the inferior-superior axis.

Based on the results of this current study, it appears as though the inversion is likely to occur for the central-peripheral axis, as we can see more twisting and overlap in this axis (Fig. 4.8), whereas there is a clear dorsal-ventral segregation of inferior and superior streamlines. Indeed, it is likely that the crossing over of fibres for the central-peripheral axis is what leads to poorer segmentation of the LGN into central and peripheral subregions compared with the inferior-superior segmentation, as the crossing over causes partial volume effects, which the resolution of DWI is unable to resolve. Looking at the probabilistic trajectory of the fibres, although there is not a clear, direct crossing over of fibres, it does appear that the pathway from the LGN to central V1 runs in a direct route to the posterior of the brain, passing alongside peripheral V1 on the way, while the pathway to peripheral V1 from the LGN, turns and twists around the central pathway and branches off appropriately when nearing V1 regions subserving peripheral V1. This study shows for the first time in macaques the 3D trajectory of topological geniculocortical connections, and supports the principle of an inverted connectivity in one plane as proposed by Connolly and Van Essen (1984).

In conclusion, the analyses presented in this chapter indicate that DWI is capable of mapping topological connectivity at a level of accuracy previously not thought possible, and that the level of accuracy can be validated qualitatively and quantitatively. A mean overall accuracy of 67.7% was achieved for predicting the central-peripheral topography of the LGN to V1 connectivity compared against the LGN atlas, while a mean accuracy

of 83.6% was achieved for predicting the inferior-superior topography. The connectivity measures derived from DWI were also found to be highly comparable to those derived from gold standard techniques, for LGN magnocellular and parvocellular subregions.

Chapter 5

V5/MT and *in vivo* probabilistic tractography

5.1 Introduction

Extrastriate visual area V5/MT was first identified by Zeki (1969) as a distinct cytoarchetectonic area located in the posterior bank of the temporal sulcus, whose neurons were later shown to be particular sensitive to direction and velocity of motion stimuli (Dubner & Zeki, 1971). Tracer studies have shown reciprocal connectivity between area V5/MT and V1 (Zeki, 1969; Ungerleider & Mishkin, 1979; Maunsell and Van Essen, 1983; Fries et al., 1985). The general model of motion processing is that V1 neurons form the initial stages of motion processing, in which the motion of the individual components of a pattern are extracted, and this information is then passed to extrastriate areas such as V5/MT where the global motion pattern is computed (Adelson & Movshon, 1982; Movshon & Newsome, 1984). Furthermore, micro-stimulation of V5/MT neurons in awake, behaving macaques have been shown to influence perceptual decisions about motion stimuli, and indicates that V5/MT makes a direct contribution to the perception of motion stimuli (Krug et al., 2013). V5/MT is also known to be retinotopically organised, with each hemisphere

mapping the contralateral visual field (Maunsell & Van Essen, 1987). Representation of the central visual field (0-15°) occupies over half of V5/MT's surface area, and there is also a slight bias toward the lower quadrant of the visual field (Van Essen et al., 1981).

While the pathway between V1 and V5/MT has only been described qualitatively or at best semi-quantitatively, it is generally considered to be a long-range, low-weight, weak connection (Felleman & Van Essen, 1991; Markov et al., 2013), particularly in comparison to thalamocortical connections. In contrast to the LGN, which sends the majority of its projections to V1, V5/MT sends major projections to MST, a region immediately medial to V5/MT, (Newsome & Wurtz, 1981; Van Essen et al., 1981), and VIP. The cortical inputs to V5/MT come from several areas, including V1, V1, V3, V3A, VP and PIP (Maunsell & Van Essen, 1983c; Felleman & Van Essen, 1991). Although single axon data suggest that the strongest input to V5/MT is most likely from V1 (Rockland, 1989; Rockland, 1995). V1 and V5/MT are reciprocally connected, with the projection from V1 arising predominantly in layer IVb, and to a lesser degree layer VI (Zeki, 1969; Lund et al., 1975), and the projection from V5/MT back to V1 terminating in those layers from which the projection to V5/MT originates, i.e. layers IVb and VI (Maunsell & Van Essen, 1983c).

Thus, area V5/MT is highly suitable region for addressing whether the many connections between LGN and V1 were necessary to predict LGN's visual topography? To see if we could trace cortico-cortical connections as well as thalamocortical connections, this chapter uses probabilistic tractography to try and predict the visual topography of extrastriate cortical area V5/MT. The same tractography techniques were used as for the LGN analyses, except that streamlines were seeded in V5/MT instead. To further test the capability of diffusion-weighted imaging and probabilistic tractography, this chapter employed the same methodologies as in the *post mortem* analyses to determine whether topological connectivity can be detected in *in vivo* datasets previously thought to be of too low resolution for that to be achievable. The LGN to V1 connectivity in datasets from four of the same brains that were analysed in the *post mortem* chapter, were also analysed in this chapter.

5.2 Methods

The V5/MT seed masks were tailored by hand for each brain with reference to myelin-stained histological slices taken from the left hemisphere (ROI delineation performed by Dr. Jackson Smith). This was done to address the inter-subject variation of V5/MT on the cortex (Van Essen et al. 1981). V5/MT maps onto a well-defined region of dense myelination (Large et al., 2016), and therefore construction of seed masks based on visual comparison to the myelin-stained sections of the same brains provides an accurate means of delineating the region. This is important as the variability in location of V5/MT relative to gyral and sulcal landmarks is on the order of 2-3 mm, and therefore a significant fraction of the area. To verify the predicted visual topography of V5/MT, the predicted maps were first compared them qualitatively with electrophysiological visual maps of V5/MT obtained previously in this lab from other animals (Krug et al., 2004). The maps were created from single neuron extracellular recordings in two, awake macaque monkeys. The electrodes were introduced into the visual cortex at an angle of 20° to the horizontal plane. Quantitative validation of the predicted topographic maps was achieved by computing the distance between the centres of gravity (COGs) for each part of the predicted topographic map (see Chapter 2, *Evaluating the topographic predictions based on tractography*). All probabilistic tractography parameters and analysis procedures were the same as in the *post mortem* LGN to V1 analyses, and carried out on the same six *post mortem* macaque brains as the LGN to V1 analyses.

For *in vivo* tractography, analyses were carried out on *in vivo* DWI acquired from four of the same brains used in the *post mortem* analyses. The step length tractography parameter of 1.0 mm was used to match the voxel width of the in vivo data, and the number of steps readjusted to maintain a maximum permitted streamline length 75% of the total brain length. 2.4×10^6 streamlines were generated per seed voxel, in comparison to the 3×10^5 generated for the *post mortem* datasets, in order maintain the same density of streamlines (1 mm^3 *in vivo* vs. 0.125 mm^3 *post mortem*). All other probabilistic tractog-

raphy parameters and analysis procedures were the same as in the *post mortem* LGN to V1 analyses.

5.3 Results

5.3.1 Mapping visual topography in V5/MT based on *post mortem* tractography to V1

The eccentricity maps were first predicted, and compared by eye with receptive field (RF) maps obtained by the Krug lab in previous experiments (Krug et al., 2004). In those awake recording experiments, electrode penetrations took a posterior approach to V5/MT through a recording chamber over the occipital lobe that was angled by 20°. Figure 5.1A shows the average eccentricity of V5/MT RFs at each electrode penetration site for two different animals. The perspective is that of someone standing behind the monkey and looking down the recording chamber towards V5/MT.

The RF maps show that the central visual field was represented in the ventral-lateral part of V5/MT – while the periphery had a dorsal-medial representation (see also Van Essen & Maunsell, 1981; Kolster et al., 2009). Figure 5.1B shows the eccentricity maps that were predicted using probabilistic tractography. These were projected onto a 2D plane that was tilted by 20°, to resemble the RF maps (Fig. 5.1A). Almost all of them show the same relative organisation, with a ventral-lateral central region, and a dorsal-medial peripheral region. However, the amount of V5/MT devoted to central eccentricities appears to be underestimated relative to the electrophysiological map.

Next, the elevation maps were predicted. These should have looked like the RF maps (Fig. 5.1C), where ventral V5/MT represented the superior visual field and dorsal V5/MT represented inferior. The top part of the DWI-based elevation maps (Fig. 5.1D) had a similar arrangement; the dorsal tips were mapped inferior, and superior was mapped just below that. However, the ventral part of V5/MT was mapped inferior, in most hemispheres. In some cases, the medial rim was also mapped inferior (e.g. M129 left), which agrees with other maps of V5/MT (Van Essen et al. 1981; Kolster et al. 2009, 2014) that show

the elevation decreasing from medial to lateral. But these maps do not have the same ventral-inferior region that was predicted here.

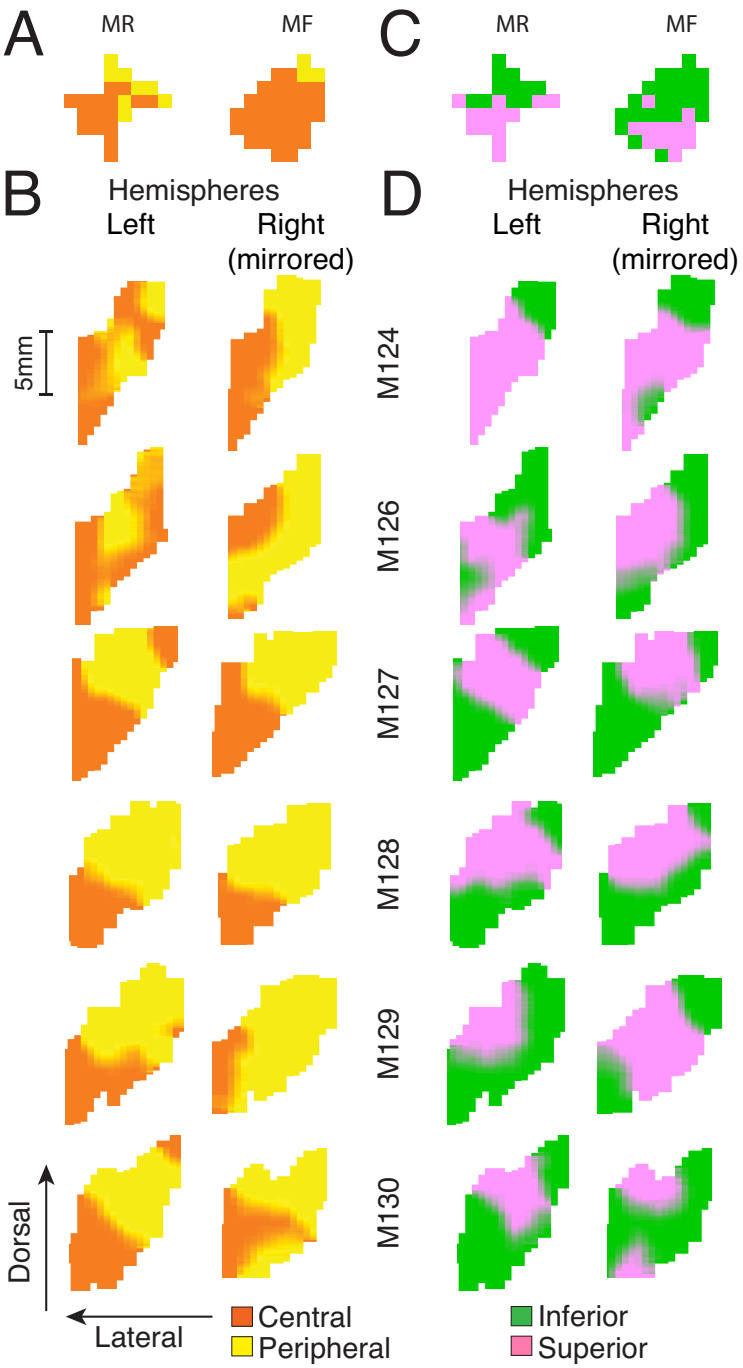

Figure 5.1: **V5/MT topography.** **(A)** Average receptive field (RF) eccentricity of isolated V5/MT neurons recorded using single electrodes in the left hemisphere of two behaving monkeys (MR and MF; Krug et al., 2004). Squares show the average RF centre for different grid positions (1 mm spacing) in the recording chamber, which was angled at 20°. RFs were either in the central (orange) or peripheral (yellow) visual field. **(B)** The predicted V5/MT eccentricity maps, based on *post mortem* DWI. Maps were projected at 20° to match the electrophysiology data. **(C)** same as A, but showing whether RFs were in the inferior (green) or superior (salmon) visual field. **(D)** Same as B, but showing the predicted V5/MT elevation maps.

5.3.2 Topographic map orientation

Since it was not possible to register the predicted topographic maps onto the electrophysiological visual maps of V5/MT, an alternative method of verifying whether voxels in the predicted maps formed spatially distinct clusters was required. To do this, I analysed the relative positions of predicted visual map voxels by computing the centres of gravity (COG) for each part of a single predicted topographic map (e.g. central and peripheral), and comparing the spatial separation of these two parts. The COGs for each part of a predicted topographic map can either be computed from the probability density map (PDF map COG), or from the binarized, hard-segmented map (hard-segmented map COG) in which all voxels in that part of the predicted map have a value of 1. Computing the COG from the PDF map gives the average position of each seed voxel weighted by the voxel's probability of landing a streamline on a given target, meaning the COG is pulled towards the part of the seed that landed the most streamlines on a specific target. Alternatively, computing the COG from the hard-segmented map does not weight the COG by the streamline density and gives a more representative view of the spatial locations of the predicted topographic map regions. The hard-segmented map COG was used for representation of the predicted map COGs in standard space in Figure 5.2, and for comparison with the V5/MT and LGN atlas along the dorsal-ventral, anterior-posterior and medial-lateral dimensions. The PDF map COGs were used when estimating the significance of the spatial separation of the predicted topographic regions from the Euclidean distance between those regions.

The predicted maps were first registered onto the 112RM-SL atlas (McLaren et al., 2009), to compare different hemispheres. The hard-segmented map COGs were then found for each topographic mapping, including for the predicted LGN topographic maps from Chapter 4. Figure 5.2 shows a coronal projection of the COGs (circles) of the central (orange, A&C), peripheral (yellow, A&C), inferior (green, B&D), and superior (pink, B&C) visual field representations in V5/MT (A&B) and LGN (C&D). Lines (grey) connect data from the

same hemisphere, showing the axis of each map. Compared to a V5/MT (A&B, left; Van Essen et al., 1981; see also Fig. 5.1A&C) and LGN (C&D, left; Erwin et al. 1999) atlas, the relative configuration of the predicted maps was generally correct: in V5/MT, central was ventral of peripheral; in LGN, central was dorsal-lateral of peripheral, and inferior was dorsal-medial of superior. However, from this analysis of the tractography results there was no consistent arrangement for the V5/MT elevation maps.

The results indicated that the average central V5/MT COG was 1.64 mm lateral (SD ± 1.07 mm, paired t-test, $p < 0.001$), 1.15 mm anterior (± 1.29 mm, p = 0.01), and 2.77 mm ventral (± 2.26 mm, $p = 0.001$) of the average peripheral V5/MT COG. By contrast, the average inferior and superior V5/MT COGs were not different from each other (medial/lateral distance = 0.08 mm [SD ± 1.04 mm], $p = 0.51$; dorsal-ventral = 0.44 mm [± 0.89 mm], $p = 0.11$; anterior-posterior = 0.22 mm, [± 2.39 mm], $p = 0.75$). In the LGN, the average central COG was 0.42 mm lateral (SD ± 0.15 mm, $p < 0.001$), 0.24 mm posterior (± 0.31 mm, $p = 0.012$) and 0.40 mm dorsal (± 0.44 mm, $p = 0.005$) of the average peripheral COG, while the average inferior COG was 0.38 mm medial (± 0.14 mm, $p < 0.001$), 0.2 mm anterior (± 0.19 mm, $p = 0.002$), and 0.29 mm dorsal (± 0.27 mm, $p = 0.002$) of the average superior COG.

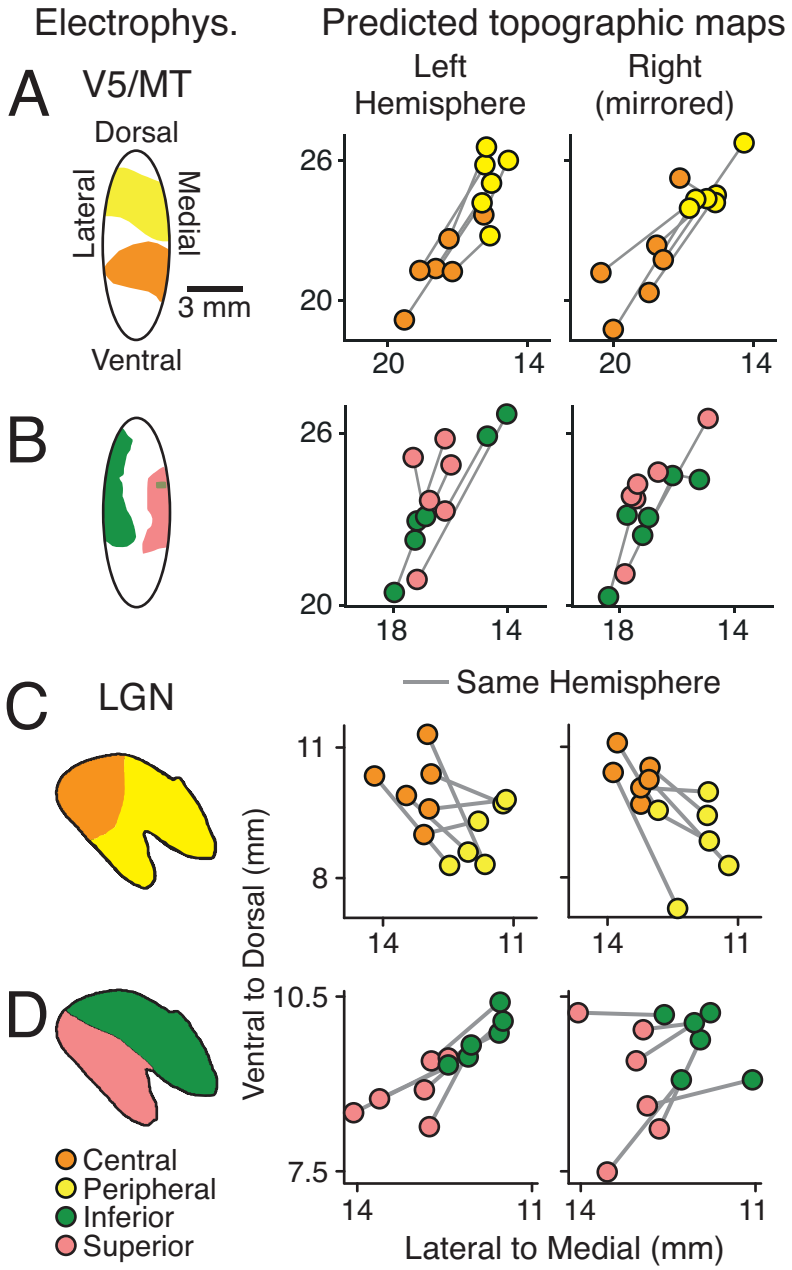

Figure 5.2: **Relative orientation of predicted topographic maps in V5/MT and LGN. (A)** V5/MT eccentricity topography showing the hard-segmented map COGs (circles) of central (orange) and peripheral (yellow) visual field, from a coronal perspective (right-hand panels). Data from the same hemisphere are linked (grey lines). An atlas derived from electrophysiology recordings is shown for comparison (left, Van Essen et al., 1981). **(B)** Like A, but showing V5/MT elevation mapping inferior (green) and superior (pink) visual field. **(C)** Like A, but showing LGN eccentricity maps (LGN atlas, Erwin et al., 1999). **(D)** Like C, but showing LGN elevation maps. Predicted maps were all registered to the 112RM-SL atlas (McLaren et al., 2010), before computing the COGs.

In order to estimate the significance of the spatial separation of COGs, the Euclidean distance between each PDF map COG pair was first computed. This simultaneously compares all spatial dimensions from two points on the Cartesian plane using the formula:

$$Distance = \sqrt{(x2 - x1)^2 + (y2 - y1)^2 + (z2 - z1)^2}$$

A randomised, non-parametric test was then carried out on the Euclidean distances computed from each hemisphere from each topographic map pairing to estimate the significance. For V5/MT, the average distance from central to peripheral PDF map COGs was 3.52 mm (SD $\pm$ 2.36 mm, $p < 0.01$). Although the average distance from inferior to superior PDF map COGs was 3.38 mm ($\pm$ 1.55 mm, $p < 0.01$), this had no systematic orientation (Fig. 5.1D, Fig. 5.2B). For LGN, the average distance between central and peripheral COGs was 0.7 mm ($\pm$ 0.44 mm, $p < 0.01$), while the average distance between inferior and superior COGs was 0.60 mm ($\pm$ 0.18 mm, $p < 0.01$).

In summary, the relative spatial locations of parts of the predicted V5/MT eccentricity map were comparable to the Van Essen et al. (1981) atlas based on electrophysiology. The atlas estimates a 3.5 mm dorsal-ventral distance between central-peripheral visual field representations, which is similar to the 2.77 mm distance between the hard-segmented COGs in this study (Fig. 5.2A). The Van Essen et al. atlas also estimates an approximately 3 mm lateral-medial distance for inferior-superior visual field representations; however, this study does not find any significant difference in lateral-medial distance for inferior-superior visual field representations (Fig. 5.2B). Assuming the curvature along the cortex is negligible then the Euclidean distance between COGs should be similar to the dorsal-ventral distance for V5/MT. The mean Euclidean distance of 3.52 mm computed for the predicted topographic map COGs is comparable to the 3.5 mm dorsal-ventral distance estimated from the V5/MT Van Essen et al. atlas for central-peripheral visual field representations. A mean Euclidean distance of 3.38 mm was also comparable to the 3 mm lateral-medial

distance for inferior-superior visual field representations estimated from the Van Essen atlas, however, it is important to note that there was no systematic orientation of the inferior and superior predicted topographic map regions.

The Euclidean distances between the COGs of the LGN predicted topographic maps were underestimated (0.7 mm for the central-peripheral distance, and 0.6 mm for the inferior-superior distance). In the digital LGN atlas (Erwin et al., 1999), the Euclidean distance from the central COG to the peripheral COG is 2.75 mm, and 2.25 mm from the inferior COG to the superior COG. This underestimation may result from a bias in streamline sampling, as more streamlines from lateral LGN were kept. Thus, when computing the COGs from the underlying PDF maps, the Euclidean distances are underestimated. To confirm this, a comparison was made between the mean COG for the LGN seed mask and the mean COGs for the PDF maps. The comparison revealed that PDF map COGs were located significantly more laterally than the centre of the LGN (PDF map COG medial-lateral position vs LGN seed mask medial-lateral position, average difference = 0.62 mm, t-test, $p < 0.001$). Looking instead at the LGN COGs computed from the hard-segmented, binzarized topographic maps, the average positions of the predicted visual mappings in the LGN (Fig. 5.2 C&D) are more in line with the atlas (mean central vs peripheral COG = 2.06 mm [SD $\pm$ 0.79]; inferior vs superior = 1.56 mm [SD $\pm$ 0.21].

Altogether, these results suggest that some of V5/MT's visual topography, namely the central-peripheral visual field topography, can be predicted from tractographic estimates of its cortico-cortical connections with V1, and underline the ability of DWI to predict the visual mapping of LGN.

5.3.3 Predicting LGN visual topography from *in vivo* DWI and probabilistic tractography

Obtaining high-quality DWI data from living subjects is difficult because scan times are limited, and the data contain physiological noise and motion artefacts. So, how much anatomical information is captured by *in vivo* DWI? To address this question the topographic maps obtained *in vivo* were compared to the digital LGN atlas. Predicted topographic maps obtained *in vivo* were also directly compared to the topographic maps obtained from the same *post mortem* brain. Both scans sample the same underlying anatomical information; therefore they should produce similar topographic maps. Four brains scanned *in vivo* were analysed. Except for step size and the number of streamlines seeded from each voxel, tractography was carried out the same way as for the *post mortem* DWI. LGN voxels were classified as inferior/superior (Fig. 5.3) or central/peripheral (Fig. 5.4) as before and displayed in stereotactic coordinates (112-SL atlas space; McLaren et al., 2009). The predicted maps again reveal distinct subregions whose relative locations are in accordance with what would be predicted based on the digital atlas of the macaque LGN.

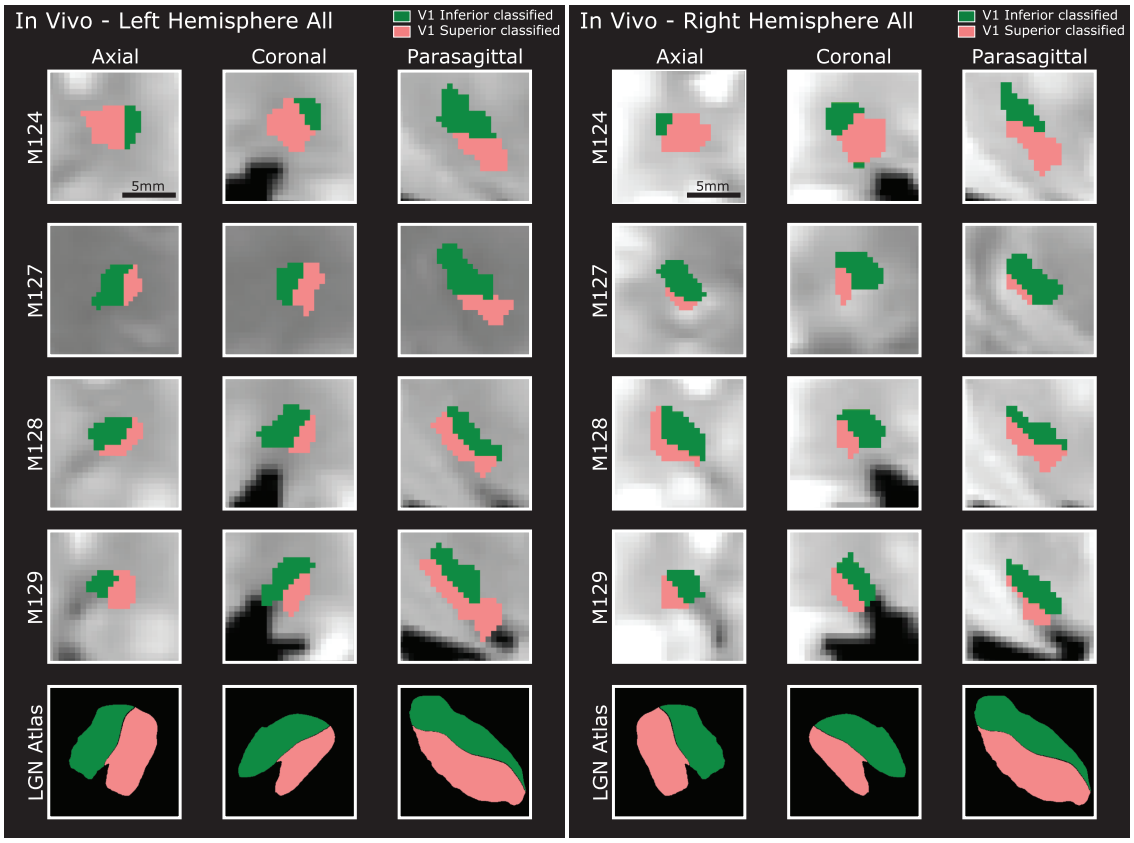

Figure 5.3: **In vivo predicted LGN elevation maps for all hemispheres (n = 8).** Midpoint slices of the LGN are shown for each brain (rows), plane of view (columns), and hemisphere. The bottom row shows corresponding slices through the LGN atlas (Erwin et al., 1999). Colours show the visual field representation in each map (inferior visual field, green; superior, pink). Hemispheres in brains M127, M128, and M129 all show two distinct clusters of inferior and superior classified voxels, whose relative locations and volumes match well the with the digital LGN atlas. The M124 left and right hemisphere voxel clusters appear to match the atlas well in the parasagittal plane, but do not fully match the atlas in the axial or coronal planes. Black scale bars are 5mm.

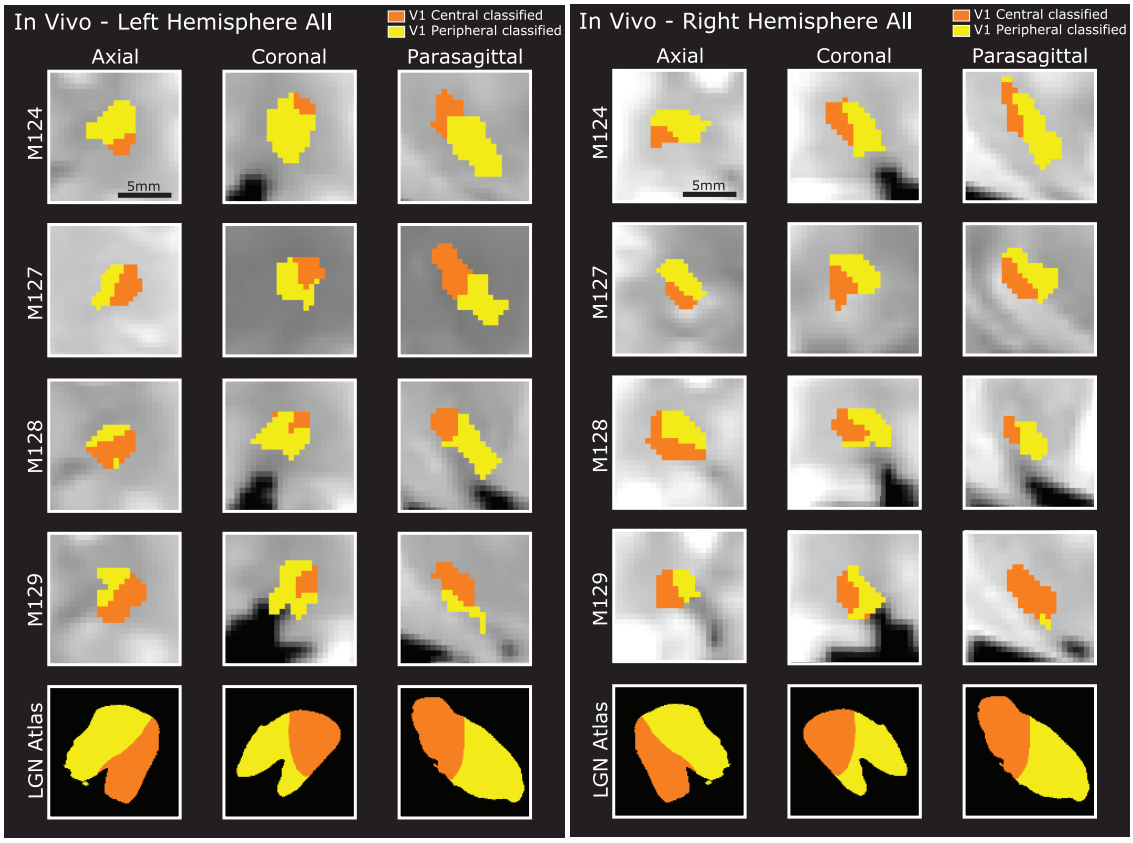

Figure 5.4: **In vivo predicted LGN eccentricity maps for all hemispheres (n = 8).** Middle slices of LGN are shown for each brain (rows), plane of view (columns), and hemisphere. The bottom row shows corresponding points in the LGN atlas (Erwin et al., 1999). Colours show the visual field representation in each map (central visual field, orange; peripheral, yellow). In most hemispheres, the relative location of centrally classified voxels and peripherally classified voxels match the LGN atlas. Black scale bars are 5mm.

Firstly, the *in vivo* LGN predicted maps were compared against the high-resolution digital LGN atlas (Erwin et al., 1999). On average the predicted maps agreed with the atlas (mean correct percentage = 63.3% [17.3], t-test, $p = 0.008$). On average the elevation maps (mean = 68.1% [16.4], were better predicted than the eccentricity maps (mean = 58.5% [18.0]), however this difference was not significant (paired t-test, $p = 0.35$). A random permutation test provided the significance of each individual comparison. For 13 of 16 predicted topographic maps, the similarity between the predicted map and the atlas was significantly better than chance ($p < 0.05$). The three comparisons that were not similar to the atlas were M124 right (inferior-superior), M127 left (central-peripheral), and M18 right (central-peripheral). These results suggest that for the majority of the *in vivo* DWI datasets, probabilistic tractography detected the general topographic organisation of LGN to V1 connections similarly to the *post mortem* DWI, although to a slightly lesser extent.

To quantitatively compare the *in vivo* results to the *post mortem* results, the streamline frequency maps from both *in vivo* LGN and V5/MT sessions were then registered to the *post mortem* images of the same brain, where topographic maps were predicted as before. This allowed a voxel-wise comparison of the *in vivo* and *post mortem* maps. The percentage of each map that was the same was measured, using either *in vivo* or *post mortem* DWI. For example, Figure 5.5A&B demonstrates the similarity of the *in vivo* and *post mortem* LGN elevation (A) and V5/MT eccentricity (B) maps for one hemisphere (M129, left). Each hemisphere was then plotted as an overlap ratio: 'empirical match / chance', where *chance* is the probability of randomly selecting the same topographic label from both maps, and *empirical match* is the fraction of voxels with the same label in both maps (Fig. 5.5C).

On average, the *in vivo* and *post mortem* maps were similar (mean = 61.10%, SD $\pm$ 17.36%; one-way t-test, $p = 0.001$), but the LGN maps (Fig. 5.5C, circles) were more alike than the V5/MT maps (squares; mean LGN = 71.92%, V5/MT = 50.25%, two-way ANOVA, $p < 0.001$). Although the similarity of eccentricity (Fig. 5.5C, orange-yellow; mean = 63.48%) and elevation (pink-green; mean = 58.69%) maps was not different overall ($p =$

0.29), this depended on the seed area (interaction, $p = 0.016$). Assuming a chance value of 50%, the average similarity was greater than chance for the LGN elevation (mean = 75.21% [SD ± 16.26], t-test, $p = 0.003$), and eccentricity (mean = 68.63% [± 9.47], $p < 0.001$) maps. Although the similarity of the LGN elevation maps was slightly higher (mean difference 6.58%), this was not significant (paired t-test, $p = 0.30$). There was a non-significant trend for the V5/MT eccentricity maps to be similar (mean = 58.34% [± 14.50], $p = 0.148$), but this was skewed by one outlier (M128 right, 32.76% similarity < chance, random permutation test, $p < 0.001$). When removed, the similarity of V5/MT eccentricity was above chance (mean = 62.00%, paired t-test, $p = 0.028$). In contrast, the similarity of V5/MT elevation maps was less than chance (mean = 42.17% [± 8.27], $p = 0.032$).

In order to account for individual differences in the chance level (see Fig. 5.5C, 95% confidence intervals, black and dotted lines) the significance of each individual *in vivo* to *post mortem* comparison was found using a random permutation test. 20 of 32 comparisons (62.5%) were above chance ($p < 0.002$), 5 (15.6%) were not different from chance ($p > 0.086$), and 7 (21.9%) were significantly below chance ($p < 0.002$). Of the 20 comparisons above chance, 7 were LGN elevation maps, 7 were LGN eccentricity maps, 5 were V5/MT eccentricity maps, and 1 was a V5/MT elevation map. Of the 5 non-significant comparisons, there was one LGN elevation, LGN eccentricity and V5/MT elevation map, and 2 V5/MT eccentricity maps. Most of the 7 comparisons below chance were V5/MT elevation maps (6) and one was a V5/MT eccentricity map. Thus, even when taking different chance levels into account, the most success in predicting topographies was observed for *in vivo* LGN, followed by V5/MT eccentricity maps, with a failure to replicate V5/MT elevation maps. This suggests that the *in vivo* DWI detected some of the topographically organised connections between V1 and both LGN and V5/MT.

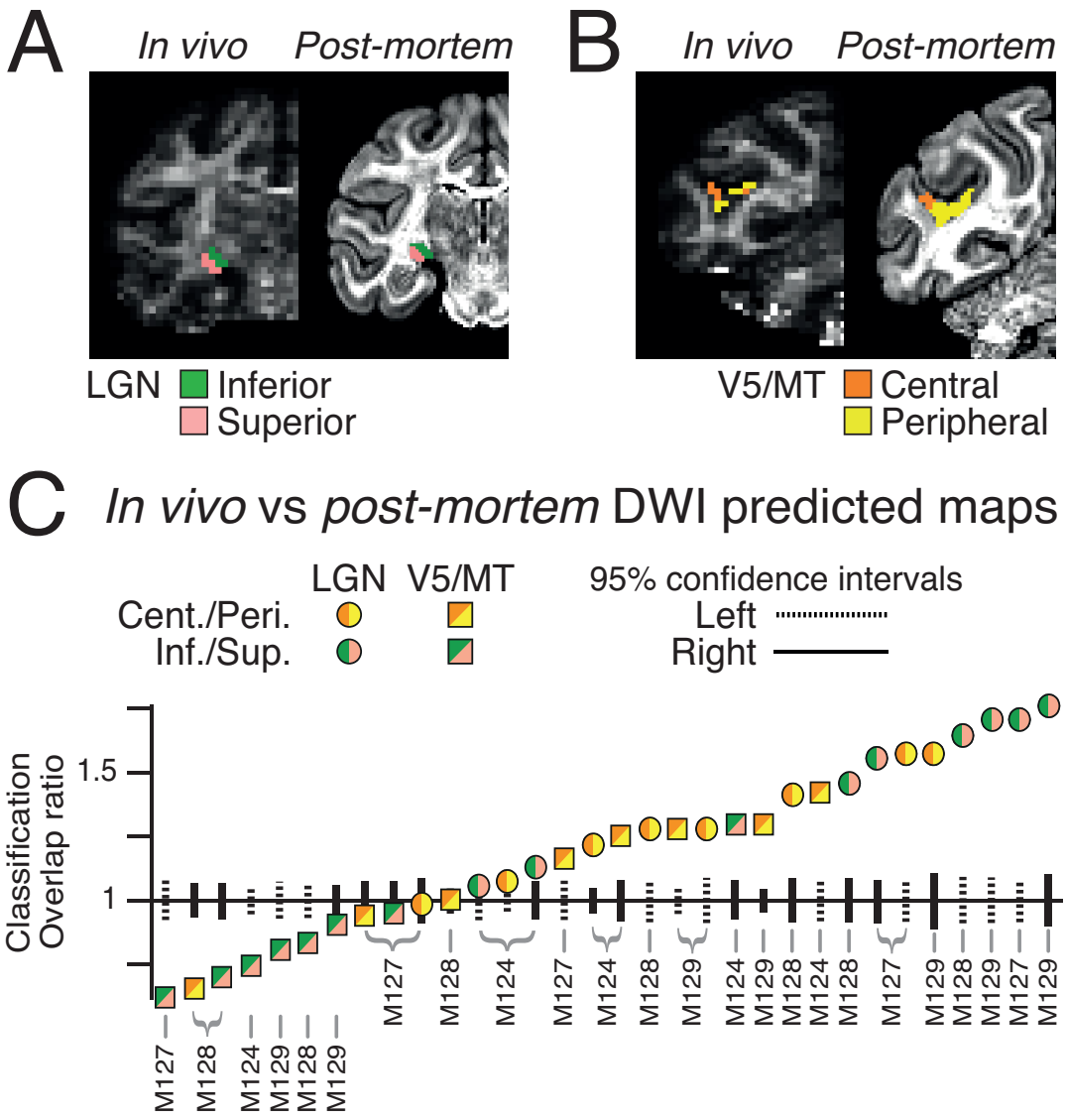

Figure 5.5: **Comparing topographic predictions using in vivo and post mortem DWI. A-B**, Side by side comparison of the predicted LGN elevation **(A)** and V5/MT eccentricity **(B)** maps from an example brain (M129) scanned *in vivo* (left) and *post mortem* (right), on top of coronal slices of the fractional anisotropy maps. **(C)** Voxel-wise comparison of predicted eccentricity (orange/yellow) and elevation (pink/green) maps from *in vivo* and *post mortem* DWI, for LGN (circles) and V5/MT (squares). Overlap ratio given as 'empirical match / chance'. Lines are 95% confidence intervals (left hemisphere, dashed; right hemisphere, solid).

5.4 Discussion

5.4.1 Mapping V5/MT and in vivo LGN topography with probabilistic tractography

As an extension of the previous work on thalamocortical topological connections (Chapter 4), this chapter demonstrated that DWI and probabilistic tractography is able to uncover highly specific topological connections in the cortico-cortical V5/MT to V1 pathway. This pathway is relatively weaker than the thalamocortical optic radiation pathway, however, the process of using extended target masks and normalization of the bias in tractography was successful in boosting sensitivity of the weaker tractographic signals of the V5/MT pathway. The pathway was successfully reconstructed, and eccentricity, in particular, was mapped in good agreement with electrophysiological and histological observations. Loss of specificity in the probabilistic tracking may explain the failure to predict V5/MT elevation maps, as the more the tractographic signal is boosted, the more noise is also introduced and the lower the specificity of the tracking (see following discussion on probabilistic tractography and diffusion imaging). Kolster et al. (2009, 2014) has suggested that a cluster of areas in the STS (including V5/MT, as well as MST, FST and V4t) are organised around a common point on the cortical surface that represents the fovea. Both the eccentricity and elevation maps are organized around that point, but orthogonally to one another. Eccentricity is mapped concentrically, with greater eccentricities being mapped onto larger circles. Elevation, however, is mapped radially, organized along lines that radiate out from the foveal point, such that one line across the cortex maps to the same visual elevation. As a result, the central representation in ventral V5/MT is close to an area where elevation switches rapidly around the foveal point. Therefore, it may be that our method was unable to resolve the close proximity of central/inferior visual representations in neighboring cortical areas. In addition, the elevation map of V5/MT varies across the thinnest dimension of V5/MT (Van Essen et al. 1981; Kolster et al. 2009), which may have been more difficult to resolve than the eccentricity map, which varies across the longest dimension of

V5/MT. Furthermore, the repeating pattern of different elevations across the visual areas comprising this cluster means that if area borders are not accurately defined, one would expect to see repetitions in the topographic map.

The results in this chapter also suggest that the *in vivo* DWI carried anatomical information about topographically organised connections. The highest success was observed in using *in vivo* DWI to predict LGN topographic maps, which is likely thanks to the large number of axons passing directly between the two areas. The LGN topographic maps showed a significant degree of similarity with the digital atlas (Erwin et al., 1999) for 13 out of the 16 comparisons (both central-peripheral and inferior-superior topographic maps), although the mean similarity between the predicted map and the atlas were lower than was achieved for the same *post mortem* hemispheres. DWI was often able to predict the V5/MT eccentricity maps, though not as well as the LGN maps. This was not necessarily surprising, as the cortico-cortical V1 to V5/MT connections were fewer and more complex. There was a failure, however, to replicate the V5/MT elevation maps. The significant disagreement of the *in vivo* and *post mortem* maps should not be surprising, as it was not possible to predict accurate V5/MT elevation maps from *post mortem* DWI. Therefore, the *in vivo* DWI of lesser resolution and signal-to-noise could only result in noisier estimates of the V5/MT elevation maps that were poorly matched to the *post-mortem* estimates.

5.4.2 Limitations of probabilistic tractography and diffusion imaging

The limitations of DWI tractography have been well documented since its inception (Basser et al., 2000), and relate primarily to the problem of coarseness or 'scale' of DWI. The size of a DWI voxel is several orders of magnitude larger than the size of the underlying axons it is meant to represent. This impacts the accuracy of subsequent tractography due to partial volume effects, particularly in areas with crossing fibres, and in distinguishing between fibres that run in close proximity, such as occurs within the optic radiation (Kier et al., 2004). The assumption that improvements in data quality and modeling approaches can

permit the accurate mapping of white matter pathways has been challenged by Thomas et al. (2014), who compared a single high-resolution, *post mortem* macaque DWI dataset with the results of previous tracer studies. They investigated a range of different tractography methods and concluded that neither demonstrated high anatomical accuracy, putting a limit of about 75% on the accuracy of tractography. However, their measure of DWI accuracy is limited, as they did not compare tracer data and DWI data from the same brain. Other groups have made direct comparisons of DWI data against tracer data for the same brain (Dyrby et al., 2007), and for DWI against manganese tracing in the same brain (Knösche et al., 2015). Jbabdi et al. (2013) have also shown strong agreement between chemical tracers and DWI tractography in macaques and humans for ventral prefrontal cortex (vPFC) white matter pathways. Although only qualitative, these studies demonstrated that DWI is able to delineate major fibre tracts. Knösche et al. (2015) proposed that improvements in data acquisition and signal-to-noise ratio (SNR) are likely to lead greater DWI mapping accuracy, however, all these studies highlight the tradeoff involved in DWI between sensitivity (detecting real connections) and specificity (rejecting false connections).

The findings from the current study do indicate that DWI is indeed capable of mapping topological connectivity at a level of accuracy previously not thought possible, and that the level of accuracy can be validated qualitatively and quantitatively. The high-resolution data obtained from *post mortem* macaques overcomes the limitations of poor signal-to-noise ratio and sensitivity to fast-imaging artifacts (Le Bihan, 2006), permitting the analysis of both well-known and less well-known connections. Furthermore, the careful optimization of the parameters used in the tractography sessions, such as samples per seed voxel, maximum pathway length, curvature threshold, the use of extended target masks and probability density normalization, have all contributed to the success in segmenting the LGN and V5/MT into functional subregions. More specifically, the use of extended target masks can increase the yield of streamlines reaching a target without a negative effect on accuracy. The development of this methodology has important implications in

the analysis of diffusion-weighted imaging for *in vivo* datasets. The *in vivo* studies on the same macaque brains showed that probabilistic tractography, in combination with the methodology developed here, can also be used to successfully segment the within-area LGN and V5/MT topographic maps in datasets previously thought to be of too low resolution to achieve that goal.

How can the results here be reconciled with the reports of poor anatomical accuracy by Thomas et al. (2014) using DWI to investigate tracts from the precentral gyrus and from visual area V4? This study concedes, as do Knösche et al. (2015) that there is a trade-off in achieving high sensitivity of DWI (detection of all true tracts) and high specificity (not detecting false tracts). This trade-off is an inherent limitation in the reconstruction of source information from noisy data. However, the results of this study show that, with high-resolution data, the precise delineation of seed and target ROIs, and the appropriate selection of tractography parameters, DWI is able to uncover highly specific topological connections with only a minor loss in sensitivity - as shown by the successful reconstruction of the small V5/MT to V1 pathway. The use of inclusion and exclusion masks to eliminate impossible tracts also appears to be of crucial importance in reducing false positives, and is a methodology supported by Jbabdi et al. (2013).

The findings from this thesis contribute to an important step forward in the validation of diffusion-weighted imaging for *in vivo* work, and a new impetus for segmenting gross anatomical regions into functionally meaningful entities or subdivisions, which may be too small for initial fMRI detection. These subdivisions could then be identified with DWI, and defined as regions of interest in subsequent fMRI investigations. Additionally, in clinical settings, accurately delineating the trajectory of the optic radiation preoperatively is crucial during surgeries of the temporal lobe (Yamamoto et al., 2007). In conclusion, the results presented here show that at this resolution, and combined with the techniques employed in this study, that diffusion imaging is sensitive and accurate enough to reveal evidence of ordered connectivity even within small subcortical regions (LGN) and within weakly-connected sensory cortical regions (V5/MT). This thesis demonstrates that tractog-

raphy can uncover topographical maps, and be used to generate not just valid qualitative descriptions of pathways, but also quantitative data on connectivity that can be validated against neurophysiological and histological data. The comparison of the different tractography parameters and the *in vivo* vs. *post mortem* analyses provide a benchmark for the *in vivo* clinical applications of these methods.

Chapter 6

In vivo DWI and probabilistic tractography of the human LGN

6.1 Introduction

Mapping the human connectional anatomy is a fundamental goal of modern neuroscience (Van Essen, 2013; Glasser et al., 2016), however, a major limitation is that the 'gold standard' axonal tracer methods used in animal models are not appropriate in humans. Axonal transportation of tracers relies on the active axoplasmic transportation processes that occur constantly within cells *in vivo*. The process of tract-tracing therefore usually requires the *in vivo* injection of the tracers, and subsequent *post mortem* tissue analysis, making it an unsuitable technique for human studies on ethical grounds. While the results of the previous chapters demonstrate the ability of diffusion-weighted imaging and probabilistic tractography to investigate connectivity and retinotopic organization within regions non-invasively, they also highlight the need to fully validate non-invasive tractography results, which are after all, an indirect measure of anatomical connections. Tractography studies in macaques are crucial as they can be validated with respect to tract-tracing, 'gold standard' histological and electrophysiological techniques, providing confidence in the tractography

results obtained. Such a direct validation for human diffusion studies is not possible. However, the next best approach is to translate the tractography methodology and protocols that have been established and validated in other primate species such as the Rhesus macaque, to studies of human connectivity. This is a good way of ensuring that the results of human tractography are built upon a methodologically sound foundation. The results can then be validated against the best available data source, which could be macaque tract-tracing data, simulated data, or human fMRI data. Ultimately, the solution to validating DWI studies in humans relies on establishing a valid methodology and the convergence of results from multiple imaging modalities. The aim of this chapter is to build on the macaque diffusion imaging work of the previous chapters, and to assess the ability of DWI to detect topological connectivity between the LGN and V1 in humans.

The functional and anatomical similarities between the macaque and human brain have been extensively described (e.g. Passingham, 2009; Neubert et al., 2014; Mars et al., 2011; Mars et al., 2013; Large et al., 2016), while other studies have also compared similar white matter pathways in macaques and humans (e.g. Ramnani et al., 2006; Mars et al., 2011). Studies of the human LGN, however, have generally been limited to *post mortem* analyses of degeneration patterns, usually following retinal or cortical lesions, or atrophy following diabetic or alcoholic amblyopia (Rönne, 1910; Rönne, 1914; Hickey & Guillery, 1979). A unique property of the mammalian LGN is that it exhibits sharply localized cell atrophy following retinal lesions or unilateral enucleation (Kupfer, 1962). This feature has meant that the laminar organization of the human LGN has been well studied, and has been found to be highly similar to the macaque LGN laminar organization (Hickey & Guillery, 1979). By contrast, the layout of the representation of the visual field in the human LGN is less well understood. This is because *post mortem* investigations and degeneration studies do not allow the same level of investigation of the visual field representation that electrophysiology allows in non-human primates. That being said, Kupfer (1962) looked at three cases of unilateral macular lesions, and found that the upper visual field was represented inferiorly, and lower visual field represented superiorly, similar to the organization in macaques.

However, Kupfer's study proposed that the region of the LGN representing central vision occupied the posterior two-thirds to three-fourths of the LGN volume, which Hickey and Guillery (1979) disagree with. From their histological investigations of the human LGN, they suggest the central visual field is represented in approximately half of the LGN volume. The location of the central visual field representation itself is largely agreed as being represented in the medial-posterior part of the LGN, with peripheral visual field represented in the medial and lateral portions, much in the same way as the organization in the macaque LGN (Le Gros Clark & Penman, 1933).

These studies indicate the need for a more detailed investigation into the retinotopic organization of the human LGN, and non-invasive methodologies such as fMRI and DWI represent the most appropriate way of achieving this. In a previous fMRI study, retinotopic organization in the LGN was demonstrated by distinct and inverted activations in response to checkerboard visual stimuli in inferior and superior LGN regions corresponding to upper and lower visual field stimulation respectively (Chen et al., 1999). Similarly, Schneider et al. (2004) used fMRI (1.5 mm^3 voxel resolution) at 3T to map central and peripheral visual field representations, and extended this work using population receptive field models to estimate the response properties of individual voxels in the LGN (DeSimone et al., 2015). This study produced retinotopic maps of the LGN in three human subjects mapping eccentricity and elevation separately, using checkerboard bar stimuli. Additional studies have also resolved layer-specific signals in the LGN using fMRI, with greater magnocellular layer activation in response to high temporal frequency, low spatial frequency, achromatic stimuli, and greater parvocellular layer activation in response to low temporal frequency, high spatial frequency, chromatic and achromatic stimuli (Denison et al., 2014; Zhang et al., 2015). To date, no studies have successfully reported using DWI to map retinotopic organization in the LGN. The goal of this chapter is to determine whether DWI, probabilistic tractography and the methodology established in the previous macaque DWI work, are able to detect a topographic organization in the human LGN based on its connectivity to different parts of the topographic map in V1. This is important not only in

testing the capabilities of DWI, but also in facilitating the translation of primate acquired data to the human brain.

6.2 Methods

Analysis was carried out on six adult human diffusion-weighted imaging datasets acquired as part of the Human Connectome Project (see Chapter 2). The step length tractography parameter of 1.25 mm was used to match the voxel width of the in vivo data, and the number of steps adjusted to maintain a maximum permitted streamline length 75% of the total brain length. 4.6×10^6 streamlines were generated per seed voxel, in comparison to the 3×10^5 generated for the post mortem macaque datasets (Chapters 3 and 4), in order maintain the same density of streamlines sampled from the seed region (1.95 mm^3 in vivo vs. 0.125 mm^3 post mortem). All other probabilistic tractography parameters and analysis procedures were the same as in the *post mortem* and *in vivo* LGN to V1 analyses.

6.3 Results

The elevation and eccentricity topographic LGN maps were predicted based on connectivity to different parts of V1, and compared to the population receptive field (pRF) map of elevation and eccentricity in the human LGN from DeSimone et al. (2015). Representative midpoint slices of the LGN from each hemisphere are shown in Figure 6.1 and Figure 6.2 alongside the DeSimone et al. map. The similarity of the predicted topographic maps to the DeSimone et al. map was computed by registering the predicted topographic maps onto the DeSimone et al. pRF map. This was carried out for tractography sessions using extended and non-extended, cortical target masks, and for before and after probability density normalization (Table 6.1) to give the proportion of voxels classified by target type, and mean percentage similarity score.

	% Voxels Cent	% Voxels Peri	% Similarity
Cortical Target: Pre-PDF	0.3 (0.9)	99.7 (0.9)	27.2 (22.8)
Extended Target: Pre-PDF	0.5 (1.6)	99.5 (1.6)	62.7 (8.0)
Cortical Target: Post-PDF	1.8 (4.4)	98.2 (4.4)	55.3 (18.8)
Extended Target: Post-PDF	11.0 (10.1)	89.0 (10.1)	65.2 (7.2)
	% Voxels Inferior	**% Voxels Superior**	**% Similarity**
Cortical Target: Pre-PDF	9.1 (18.5)	90.0 (18.5)	25.1 (16.8)
Extended Target: Pre-PDF	13.6 (22.4)	86.4 (22.4)	56.8 (8.4)
Cortical Target: Post-PDF	12.6 (19.3)	87.4 (19.3)	49.3 (14.5)
Extended Target: Post-PDF	22.1 (19.1)	77.9 (19.1)	54.8 (8.2)

Table 6.1: Comparison of the effect target type and probability density normalization on the proportions of central/peripheral and inferior/superior voxels, and the similarity between the topography and a pRF map. The proportion of voxels representing the central visual field in the pRF map of the LGN is 36.2%. The proportion of inferior voxels in the pRF map is 49.1%. Tractography parameters are 75% maximum streamline length, 0.5 mm steps, 0.0 curvature threshold. ±SD in parenthesis (n =12).

The results indicate that the percentage similarity between the classified DWI predicted voxels and the pRF map voxels was above chance (assuming 50%) only when using extended target masks, pre- and post-PDF for the central-peripheral topographic maps (Bonferroni corrected t-tests, Extended target Pre-PDF, $p < 0.001$, Extended target Post-PDF, $p < 0.001$, Cortical target Pre-PDF, $p = 0.35$, Cortical target Post-PDF, $p = 0.005$, similarity significantly worse than chance). For the inferior-superior topographic maps, the similarity between the predicted map and the pRF map was not significantly greater than chance for any of the conditions. The results also show that only a very small proportion of streamlines landed on central and inferior targets. For central V1 targets in particular this may be because streamlines were not reaching the central targets because of the greater distance between LGN and V1, and the greater cortical folding in humans compared with macaque brains, meaning the streamlines may have to traverse longer distances to reach their targets. To test whether this is because the maximum streamline length of 75% the brain length was terminating streamlines before they could reach the central and inferior targets, the tractography sessions were re-run with a maximum permitted streamline length 100% of the brain length. A pairwise t-test did not reveal any significant improvement in the similarity between predicted topographic maps and the pRF map (mean similarity 75% streamline length = 52.6 [21.6], mean similarity 100% streamline length = 57.3 [15.6], $p = 0.09$).

Overall, the results indicate that the topography of connectivity between the LGN and V1 could not be detected in humans with DWI and probabilistic tractography in the current form and implementation presented here. Although the similarity between the predicted maps and the pRF map was greater than chance for central-peripheral topography when using extended target masks, the proportion of centrally classified voxels was far below the expected value (36.2%). Thus, the similarity score was being driven principally by the representation of peripherally classified voxels, and because the expected proportion of peripheral voxels is much higher than that expected proportion of central voxels, this lead to a mean similarity measure significantly greater than 50%. Investigation of the topographic

maps by eye (Fig. 6.1) reveals that the predicted central-peripheral topography failed to match the topography described in the pRF map (DeSimone et al., 2015).

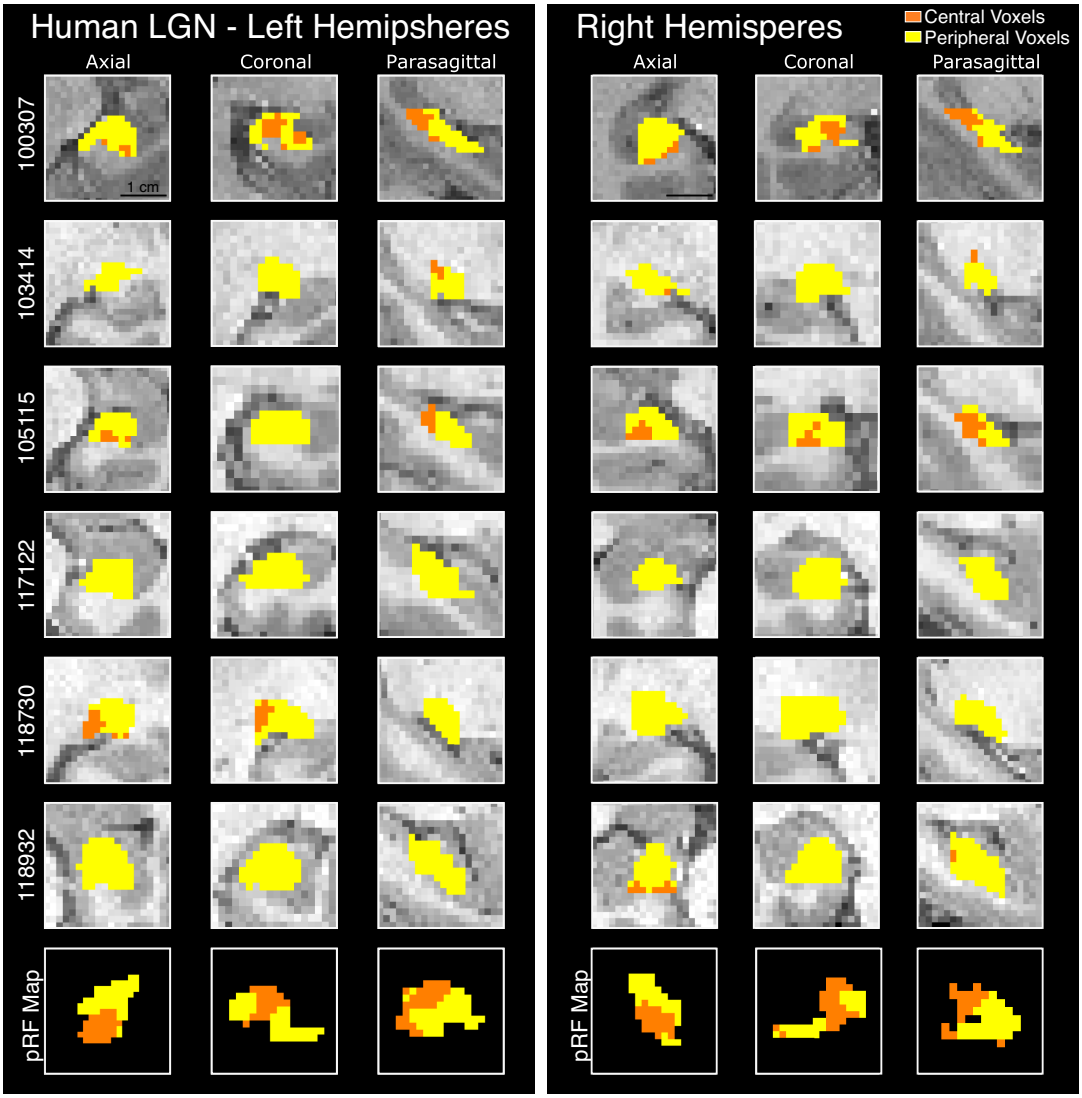

Figure 6.1: **Predicted human LGN eccentricity maps for all hemispheres (n = 12).** Midpoint slices through the LGN are shown for each brain (rows), each stereotactic plane of view (columns), and all hemispheres analysed. The bottom row shows corresponding points in the pRF map (DeSimone et al., 2015). Orange indicates the central visual field representation, and yellow indicates the peripheral visual field representation. The results show a clear over-representation of peripheral voxels in the predicted maps, and while the location of any centrally classified voxels often matches that of the pRF map, in every hemisphere there is a failure of the predicted map in matching the pRF map. Results shown are for tractography sessions run using extended targets, and post probability density normalization.

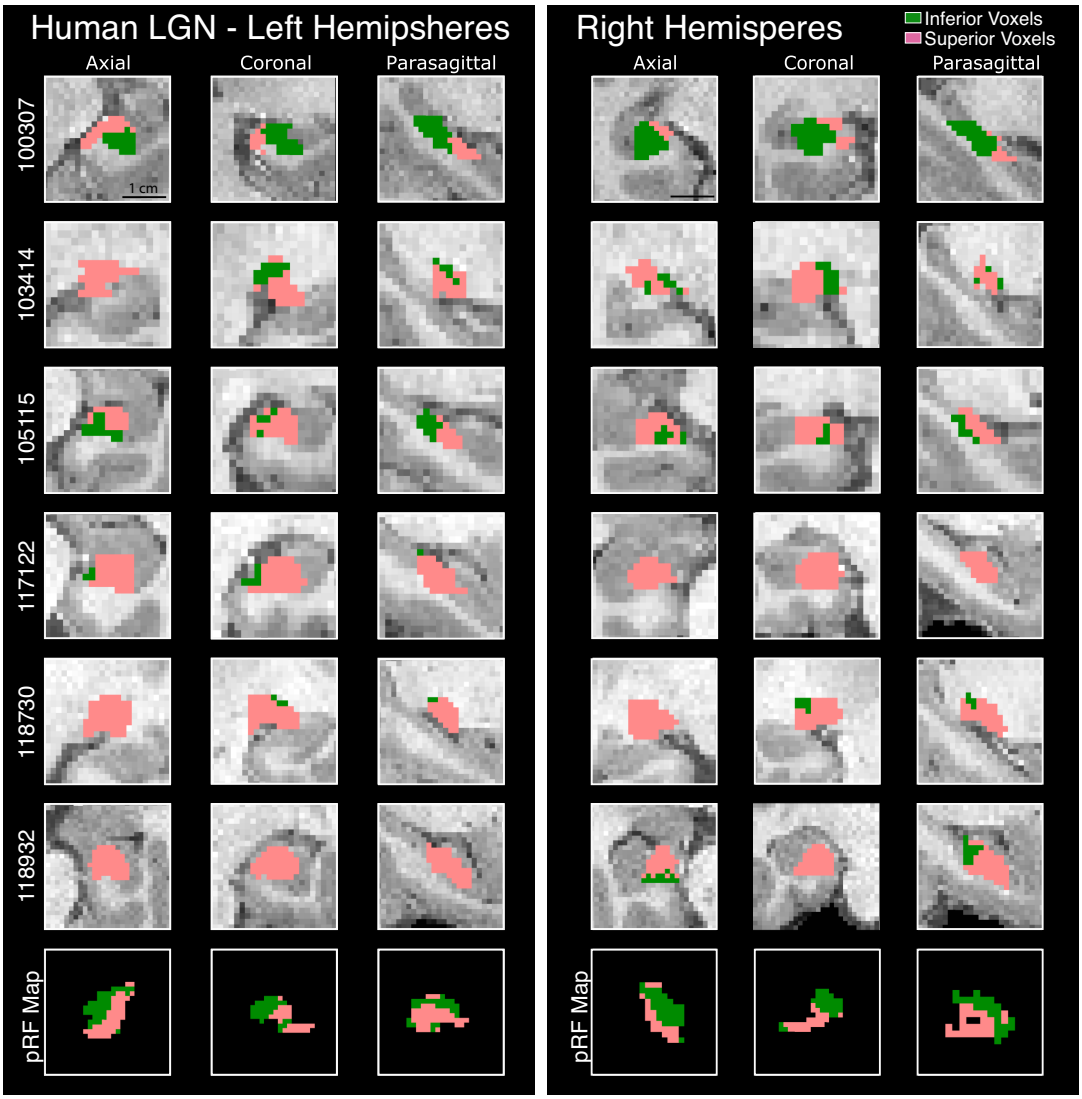

Figure 6.2: **Predicted human LGN elevation maps for all hemispheres (n = 12).** Midpoint slices through the LGN are shown for each brain (rows), each stereotactic plane of view (columns), and all hemispheres analysed. The bottom row shows corresponding points in the pRF map (DeSimone et al., 2015). Green indicates the inferior visual field representation, and pink indicates the superior visual field representation. The results show a clear over-representation of superior voxels in the predicted maps. The match between predicted topographic maps and the pRF map is extremely poor and can be regarded as a failure in every hemisphere. Results shown are for tractography sessions run using extended targets, and post probability density normalization. Black scale bars are 1cm.

6.4 Discussion

This chapter used diffusion-weighted imaging and probabilistic tractography on six human datasets obtained at 1.25 mm isotropic resolution as part of the Human Connectome Project. Overall, the similarity between the predicted topographic maps and the pRF map derived from a population receptive field model of LGN activation to checkerboard stimuli under fMRI (DeSimone et al., 2015), was poor. This could suggest that DWI and probabilistic tractography at this resolution and SNR is not capable of detecting the topography of connections between LGN and V1. However, there are several points to bear in mind before reaching this conclusion.

The first is that errors in the definition of the ROIs will inevitably lead to inaccuracies in the tractography results. In this chapter, LGN ROIs were defined on the T1-weighted anatomical MRI image, with V1 target ROIs registered onto this image from a probabilistic atlas (Wang et al., 2014). The issue here is that LGN is not easily identifiable on the T1 image, especially at this resolution, and there is also a large degree of individual variability in the size and shape of the human LGN; more so than in the macaque (Hickey & Guillery, 1979; Andrews et al., 1997). The large variability in cortical folding of area V1 (Stensaas et al., 1974) in humans also makes the definition of V1 ROIs error prone, and therefore parts of V1 defined as representing central vision may speciously include parts of V1 that actually represent peripheral vision. Furthermore, errors are more likely to be introduced during the registration of the predicted topographic LGN maps to the pRF map if these maps differ strongly in size and shape. Thus, it is not clear whether it is a case of the human *in vivo* data simply not carrying the anatomical information about topographically organised connections, or a case of errors in ROI delineation resulting in the failure of tractography to detect topographically organised connections.

Fortunately, there is a straightforward solution to determining whether errors in ROIs delineation are the cause of poor tractography results. In the DeSimone et al. (2015) fMRI study, the LGN was defined on a much higher resolution proton density image acquired

along with the other scans. A proton density image is an image produced using scan parameters designed to minimize T1 and T2 effects, producing an image primarily dependent upon the density of protons (McRobbie et al., 2003). Proton density images therefore produce a much larger contrast-to-noise ratio between the LGN and the adjacent white matter tracts, than T1 or T2-weighted scans (Fujita et al., 2001). Similarly, retinotopic mapping of V1 is a well-established way of defining regions of V1 that represent given parts of the visual field. A good extension to the work presented in this chapter would be to acquire DWI and V1/LGN retinotopic mapping, and proton density images for the same subject. The DWI could be collected using 3T and 7T MRI machines in order to compare the contributions that voxel resolution and SNR make towards detecting topographic connectivity within regions. This future work would be able to determine precisely whether *in vivo* human DWI in its current form, and using the methodology developed in this thesis, is capable of detecting topographic connectivity within regions. Indeed, in June 2016, the Human Connectome Project announced that they were releasing 7T retinotopy task fMRI data for 73 subjects that they had also acquired diffusion MRI data from. Unfortunately, the timing meant the data could not be analyzed in the present thesis, but it does offer a perfect opportunity for extending this work.

A further possibility for the failure in predicting topography is that the pRF map derived from fMRI is not a true representation of LGN organization. DeSimone et al. (2015) note in their paper that the receptive field sizes measured in the LGN are larger than would be expected, and that this misestimation is likely to arise from difficulties in imaging subcortical structures with fMRI. For example, due to the relatively low BOLD signal in deep anatomical locations, the poor signal-to-noise ratio in these areas was compensated for by stimulating a given visual field location for a longer duration with a larger stimulus, at the expense of precision of the pRF model in estimating the pRF size. Furthermore, the maps of LGN elevation and eccentricity presented in DeSimone et al. were only validated against non-human primate LGNs and previous fMRI work of lower SNR (Schneider et al., 2004). While the overall locations of central, peripheral, inferior, and superior LGN voxel

representations correspond to those locations identified in the macaque LGN and previous human LGN studies, the organization is by no means clear-cut. As can be seen in the pRF map, voxels representing central vision are often located in regions of predominantly peripheral voxels and vice versa. Thus, the pRF maps are unlikely to completely represent the ground truth, and a lack of similarity between the DWI predicted maps and the pRF map could simply be reflecting this fact. Given the lack of consistent topographic organization in the DWI predicted maps it is unlikely that this is the case, however, it is important to bear in mind in future work that quantitative assessment of DWI maps by comparison to fMRI will be inherently limited.

The alternative interpretation for the results in this chapter however, is that information about topographical connectivity between LGN and V1 is simply not carried in the human diffusion imaging data. Certainly, the resolution (1.25 mm^3) and SNR of the *in vivo* human data is poorer than the macaque DWI data collected (0.5 mm^3 *post mortem*, 1.0 mm^3 *in vivo*). To determine whether this is the case in future work, the accurate delineation of ROIs through retinotopic mapping and proton density images will need to be combined with DWI collected with high SNR and at a resolution matching that of the macaque DWI data in this thesis. Work is currently ongoing at both the Human Connectome Project and the Oxford Centre for Functional MRI of the Brain (FMRIB) to develop DWI scan sequences at 7T, giving much better SNR than the 3T scans, and nearing 1.0 mm^3 isotropic resolutions. Overall, the chapters presented in this thesis illustrate that DWI and probabilistic tractography is capable of mapping topography within non-human primate subcortical structures based on their connectivity to primary visual cortex, but that a refinement of the methodology and image quality is needed for this to be achieved for *in vivo* human data. However, this is by no means a distant goal, as the methodology and image quality that I would expect to be required to achieve this are almost certainly feasible within the near future.

Chapter 7

Task-irrelevant perceptual learning: Human psychophysics

7.1 Introduction

7.1.1 Introduction to perceptual learning

The visual system is tasked with making functional sense from the abundance of visual information coming in to the eye. It must maintain a level of stability in representing the world and not be altered by every bit of information it receives, yet simultaneously must also be able to adapt to input which has novel or salient significance so that this information can be acted upon. This conflict in demands is termed the plasticity-stability dilemma (Grossberg, 1980). How the visual system addresses this dilemma is a principal question in the field of visual neuroscience and the focus of this chapter.

Wiesel and Hubel (1963) were among the first to show that the visual system exhibited plasticity and that it could be linked to a biological substrate. They showed that temporary suturing of one eye in a kitten, in order to deprive that eye of visual information, led

to a reduction of cells in the kitten visual cortex responsive to stimuli presented to the deprived eye. In kittens deprived from birth, only 1 cell out 84 tested cells responded to the deprived eye, and that cell showed abnormal receptive fields for both eyes, having no particular orientation preference and sluggish activity. However, it was still thought that the early visual system only exhibited plasticity during early development, and that after a certain age the visual system was hard-wired. This view was substantiated by the work on critical periods by Blakemore and Van Sluyters (1974) who showed that reverse suturing of a kitten eye at 5 weeks old, caused cells to switch back to being binocularly driven after being only monocularly driven during the period of eye deprivation. At 14 weeks old, the reverse suturing had no further effect on ocular dominance, and most cells were still driven solely by the un-deprived eye. Since then, studies from a branch of visual neuroscience concerned with looking at learning in the visual system have shown that psychophysical thresholds for detection and discrimination can be altered even in adulthood, raising the question of how the visual system achieves this plasticity.

This form of plasticity is usually termed perceptual learning, and refers to the way in which repetitive training in a visual task with a specific set of visual stimuli gradually improves the ability to discriminate those stimuli, resulting in short- and long-term improvements in behavioural performance on the task (Goldstone, 1998). This perceptual learning is usually specific for the task and features learned. For instance, improvements are not seen if participants are subsequently tested with a stimulus of a different orientation, or if stimuli are presented at a different retinal- or visual- field location (Karni & Sagi, 1991). This has been taken to suggest that perceptual learning depends on local, plastic changes in early visual areas. For instance, perceptual learning that is specific to the eye of training indicates that the learning has a locus in primary visual cortex, as few cells higher up in the visual system are monocularly driven (Fahle et al., 1995). Similarly, perceptual learning effects showing retinotopic, orientation or direction specificity (e.g. Karni & Sagi, 1991; Fiorentini & Berardi, 1980; Schoups et al., 1995; Watanabe et al., 2001) are believed to involve cells in early visual cortex that have small receptive fields driven by primitive

stimulus features such as those of location, orientation and direction (Sasaki et al., 2010). The results from the studies on perceptual learning posed the question of what mechanisms acting on the visual system are responsible for gating what is to be learned. That is, what features of the stimulus are relevant and which are irrelevant, and how is this determined.

7.1.2 The role of attention in perceptual learning

Ahissar and Hochstein (1993) proposed that learning required top-down gating mechanisms, such as attention. This was based on studies such as those by Shiu and Pashler (1992), who showed that when subjects were asked to attend to the brightness of a line, performance on discriminating the orientation of the line did not improve. Performance only improved when subjects attended to the orientation of the line. In this framework, attention functions to select salient stimuli or stimulus features to be learned, and visual plasticity is gated by the attentional selection. This notion was shown to have a plausible biological basis in a single-unit recording study in macaques (Schoups et al., 2001). The orientation tuning curves of primary visual cortex neurons in this study were altered for those neurons with receptive fields representing the visual field location of the stimuli used in training, but were not altered for those neurons representing an unattended visual field location. The notion that attention is necessary and sufficient for perceptual learning has been challenged, however, by findings from human psychophysical studies showing that perceptual learning can also occur for unattended stimuli (Watanabe et al., 2001), and for task-irrelevant stimuli (Seitz et al., 2005a; Seitz & Watanabe, 2009).

7.1.3 Task-irrelevant perceptual learning

Watanabe and Seitz carried out a series of studies in which participant attention was engaged by means of a central Rapid Serial Visual Presentation (RSVP) task, while weak background motion signals were presented simultaneously in the peripheral visual field.

Despite being below the threshold of visibility and being irrelevant to the central task, performance improved specifically for the direction of the exposed motion (e.g. upwards motion direction) when later tested on a separate task. This task-irrelevant learning improved motion discrimination only for the motion direction exposed during the RSVP task, and not for the orthogonal motion direction (Watanabe et al., 2002). Tsushima et al. (2008) used the same paradigm and found that task-irrelevant perceptual learning (TIPL) occurred only when the overall motion coherence - the ratio of signal dots to noise dots - was at low, parathreshold levels (5% and 15% coherence). They proposed that the weak stimuli were not 'noticed' by an attentional-inhibitory system and so were consequently not suppressed. The phenomenon of TIPL raises several questions regarding the mechanisms of perceptual learning. It is not yet clear, for example, whether TIPL exhibits the same level of orientation or visual field specificity as has been shown with task-relevant perceptual learning.

Gutnisky et al. (2009) report that for an orientation discrimination task, improvements in performance along the presented axes are seen for stimuli in an attended location, but that the capacity for orientation discrimination away from the presented axes improves when the exposure stimuli are unattended and task-irrelevant. In this study, participants were trained with a Gabor patch at a single orientation, then required to discriminate target orientations away from the trained orientation at attended and unattended locations. As expected, the discrimination performance decreased with increasing difference between the trained and tested orientations. However, contrary to expectation, performance at the unattended location showed a higher degree of generalisation than performance at the attended location despite higher performance at the trained orientation for the attended location. In other words, the capacity to perform discriminations away from the exposed orientation was enhanced for the unattended location. Gutnisky et al. went on to confirm this finding of greater generalisation at the unattended location by using complex, natural image stimuli containing a range of orientations. Discrimination performance for determining whether these natural image stimuli were oriented with respect to a standard

non-oriented version of the stimuli was greater for the unattended location than for the attended location. This demonstrates a form of task-irrelevant perceptual learning for unattended visual field locations. The authors propose that attention serves to enhance low-level feature plasticity, but impairs generalisation of learning to new stimuli. When the findings of this study are taken together with findings from Tsushima et al. (2008) of task-irrelevant perceptual learning only for low, parathreshold stimuli, it appears that attention might be increasing local inhibition to neuronal populations tuned away from the trained stimulus feature. For example, increased inhibition due to attention could enhance discrimination of a trained orientation and impair discrimination of untrained orientations, while stimulus exposure at the unattended location decreases location inhibition for cells tuned away from the trained orientation, and improves discrimination and plasticity away from the trained orientation (Gutnisky et al., 2009).

However, this account of attention gating task-relevant and irrelevant perceptual learning is insufficient to account for other results obtained with perceptual learning paradigms. For example, Seitz and Watanabe (2003) presented task-irrelevant subthreshold motion stimuli for which a single direction of motion was consistently temporally paired with the presentation of target in a central task. If learning is the result of simple exposure to the motion, then subsequent motion discrimination performance should improve for all directions of motion presented. However, they found that motion discrimination performance improved only for the motion direction that was temporally linked to the task target. In another study, Tsuchiya and Koch (2005) presented Gabor patches to one eye of water-deprived subjects. The Gabor patches were masked from perception using a technique known as contrast flash suppression (CSF) in which randomly placed coloured patches were flashed at around 10 Hz to the other eye. Gabor patches of a certain orientation were paired with water as a reward, while the orientations were not. Subsequent testing on an orientation discrimination task revealed improvement only for the orientation previously paired with the water. These studies indicate that reward also plays a role in mediating perceptual learning, and may be the underlying mechanism driving learning in instances

where attention does not seem to be necessary.

7.1.4 The role of reward in task-irrelevant perceptual learning

Seitz and Watanabe (2005) proposed a model in which perceptual learning is the result of a bottom-up stimuli signal being boosted by a reinforcement signal related to reward. Specifically they propose that in the context of task-irrelevant learning, when stimulus-driven signals (task-irrelevant) and task-driven signals temporally coincide, it results in task-irrelevant perceptual learning. Thus, plasticity is restricted by the temporal timing of the two-signals. The model is analogous to models of conditioning and reinforcement learning. It is also important to remember that even for instances of task-irrelevant perceptual learning where no explicit reward is given, the internal motivation of participants to do well and make correct responses can serve as a reinforcer (Herzog & Fahle, 1998; Herzog & Fahle, 1999).

The emerging picture from recent literature on perceptual learning and TIPL is that reward plays a significant role and has a complex interaction with attention. For example, Wang et al. (2014) found that the level of reward directly affects the extent of inhibitory suppression and attentional focus in terms of visual field distance. While the Gutnisky et al. (2009) study demonstrated the role of attention in TIPL, more recent studies have shown that that type of attention can differentially affect learning. Mukai et al. (2011) demonstrated that both exogenous and endogenous attention improved Gabor patch orientation discrimination performance to a greater extent at attended versus unattended locations, but that only exogenous attention resulted in improved contrast detection thresholds. The findings suggest that these two types of attention may be mediated by different neural mechanisms. Attempts at characterising the interaction of reward and exogenous attention have been made, but investigation into the role of endogenous attention and reward on TIPL has so far been lacking.

7.1.5 Investigating the role of both reward and attention in TIPL

Reward has traditionally been investigated assuming that it exerts long-term effects on sensory systems and processing, and as a factor that has its effect on the later stages of information processing, close to decision-making models (Glimcher & Rustichini, 2004; Hampton et al., 2008) and to visual-motor transformations (Schultz et al., 2000). This is in contrast to the way in which attention is typically studied, which is generally in regards to effects exerted on early visual areas (e.g. McAdams & Maunsell, 1999). Clearly the framework for exploring the role of attention and reward needs updating. Schuler and Bear (2006) have found evidence of reward-based modulation of learning in early visual areas in rats, while Della Libera and Chelazzi (2006) demonstrated that reward mediates perceptual performance through its effects on the attentional system. Indeed, there are multiple possibilities for the way in which reward could influence attention. It may act as a type of incentive motivation for the strategic control of attention, or it could have its effect by altering the processing of specific stimuli by increasing their attentional priority (Chellazzi et al., 2013).

Part of the difficulty in investigating the factors affecting perceptual learning lies in teasing apart the appropriate effects of attention and reward. Reward often represents a key facet of perceptual learning paradigms, and so its effects cannot easily be disentangled from the attentional effects. TIPL represents a useful paradigm to explore the impact of reward on perceptual learning as it allows a degree of control over attention. TIPL psychophysical paradigms, in which attention is engaged in a central task while task-irrelevant Gabor stimuli are presented in the periphery, allow the testing of hypotheses of whether neuronal adaptation requires active attentional processes, and also the extent to which TIPL differs from, or is similar to, task-relevant perceptual learning. For example, does TIPL exhibit the same level of orientation or visual field specificity that task-relevant perceptual learning exhibits? Because the task-irrelevant peripheral stimuli can be temporally linked to the targets in the central attentional task, and can be associated with reward, the relationship

between reward, on one hand, and attention and learning, on the other hand can be assessed. Are active attentional processes required? To what extent can learning occur through reward-stimuli pairing independent of attention? A TIPL paradigm designed to adapt neuronal elements in early visual areas and determine the level of orientation and visual field specificity is the focus of this study.

A challenging, unanswered question in the field of perceptual learning, is how learning can occur in early sensory areas, which are remote from areas where perceptual decisions are thought to be computed (see Gold & Shadlen, 2007 for review). Theories of perceptual learning must explain where, when, and how neural changes that support perceptual learning occur. This study attempts to resolve some of these questions. It is useful first to examine the current literature on the neural mechanisms of perceptual learning at both the system-wide and individual neuronal level in order to establish a framework for addressing these questions.

7.1.6 Biological substrates for perceptual learning

Perhaps unsurprisingly, given the vast array of studies on perception, a wide range of cortical and subcortical locations have been proffered as being involved in perceptual learning. Primary visual cortex (V1) has been found to show BOLD signal changes in response to intensive monocular training on visual texture discrimination. These signal changes were specific to the V1 region corresponding to the visual field location of the training stimulus (Schwartz et al., 2002). Changes to receptive fields of V1 cells have also been identified with electrophysiology (Schoups et al., 2001). Cells in the middle visual area V4 of macaques were also found to show altered tuning properties after orientation discrimination training, despite no such tuning changes being found for V1 cells (Yang & Maunsell, 2004; Raiguel et al., 2006). V4 cells have similarly been shown to exhibit increased mean firing rate and decreased response variability after orientation discrimination training (Adab & Vogels, 2011). Other neurophysiological studies have observed that training on a dot motion task

did not alter the properties of cells in middle temporal area V5/MT, a region known to be strongly activated by motion, but did change the responses of cells in lateral intraparietal area (LIP), a region responsible for translating motion information into responses by saccadic eye movements to represent a perceptual decision (Law & Gold, 2008). This result suggests that performance improvements result from the improved interpretations by decision-making areas from lower area stimulus representations. The notion that the specificity of perceptual learning is indicative of an early visual area locus has also been challenged by findings showing transfer of learning to other locations after double training (Xiao et al., 2008). In this study they used a double-training paradigm where training on contrast discrimination was carried out at one location, along with additional training with an irrelevant orientation at a second location, either simultaneously or at a different time. They found that the additional training location enabled a complete transfer of the contrast perceptual learning to the second location, and suggests that non-retinotopic higher brain areas involved in attention and decision making are critical for perceptual learning. Given the abundance of feedback connections in the visual cortex, even to V1 (e.g. Felleman & Van Essen, 1991), it should be unsurprising that top-down activity might modulate perceptual learning.

Attention related signals have been identified in the visual processing hierarchy as early as LGN (McAlonan et al., 2008; O'Connor et al., 2002), and the superior colliculus (SC), as well as in striate and extrastriate cortical areas (V1, V4, IT and V5/MT). These signals have been proposed to exert stronger modulatory effects further up the visual processing hierarchy (Buffalo et al., 2010), and have been linked to effects such as heightened gain and sharpened tuning (Baluch & Itti, 2011). The attentional inhibitory effects in the Tsushima et al. (2008) study described previously, where learning occurred only for subthreshold stimuli that failed to be suppressed, has been linked to the role of the lateral prefrontal cortex (LPFC), a region involved in attentional selection (Knight et al., 1995). Reward too has been proposed to exert its effects on early visual cortex. Schuler and Bear (2006) carried out an experiment in which rats had to lick a water tube to obtain a water reward

in response to a visual stimulus. For rats inexperienced with task, V1 neurons were driven by the physical aspects of the visual stimulus, whereas V1 neurons of rats proficient in the task began to show activity that predicted the temporal delivery of the reward.

One theory of perceptual learning is that it results from a task-specific selective re-weighting of neural connections between the low-level visual stages selective for the feature to be learned, and a higher-level decision stage (Petrov et al., 2005). Support for this theory comes from a monkey physiology study by Chowdhury and DeAngelis (2008) who reversibly inactivated area MT in monkeys with muscimol before a disparity discrimination task. The inactivation impaired coarse disparity discrimination (which is carried by MT signals), but not if subjects had training on fine disparity discrimination before the testing on coarse discrimination was carried out. Fine disparity discrimination is believed to be carried by ventral pathway regions such as V4 and not in MT (Uka & DeAngelis, 2006; Umeda et al., 2007), and therefore suggests that ventral pathway regions are recruited in the case of MT inactivation to mediate the coarse depth discrimination. In other words, there is a selective re-weighting of the neural connections mediating learning. However, it is still unclear how the wide array of results proposing different sites of cortical plasticity can be reconciled. Ahissar and Hochstein (2004) put forward a reverse hierarchy theory (RHT) of perceptual learning, which proposes that the neuronal effects of perceptual learning transition from higher to lower areas with increasing task difficulty. As task difficulty increases, initial changes to higher level 'read-out' connections become saturated, necessitating changes to lower level representations in order to improve performance. However, Dosher and Lu (2007) have challenged this theory on the grounds that the time course of perceptual learning is not compatible with RHT. In their study, perceptual improvements in contrast threshold for an orientation discrimination task were best accounted for by an exponential form of improvement with practice. This simple exponential path of learning would not be compatible with a multi-stage process, and therefore goes against RHT of perceptual learning. A coherent mechanism for perceptual learning has evidently yet to be achieved by using a macroscopic framework. To better understand the process of vi-

sual system plasticity, a significant body of work has focused on the role of modulatory neurotransmitters in learning.

7.1.7 Modulatory neurotransmitters in perceptual learning

A large number of studies have indicated the importance of diffusely released modulatory neurotransmitters in perceptual learning (Seitz & Watanabe, 2005). Dopamine release in the ventral tegmental area (VTA) and acetylcholine release in the nucleus basilis of the basal forebrain have both been separately associated with altered auditory tone representations in primary auditory cortex (Bao et al., 2001; Kilgard & Merzenich, 1998a), while norepinephrine released from locus coeruleus has been implicated in learning at the behavioural and neuronal level (Dalley et al., 2001; Gordon et al., 1988). Neuromodulator release is likely to be responsible for gating perceptual learning, and therefore identification of the brain regions and circuits involved in their release are important in understanding the process of perceptual learning.

Of particular note is that the neuromodulators described previously, have also been suggested to underlie attention and reward. The orienting attentional system is known to drive activation in the parietal cortex (Corbetta et al., 2000), and is believed to be mediated by the acetylcholine system (Davidson & Marocco, 2000), while the attentional alerting system is thought to be mediated by the norepinephrine system (Coull et al., 1996; Marrocco et al., 1994; Witte & Marrocco, 1997). Nagano-Saito et al. (2008) used an fMRI-tyrosine depletion study to probe the role of dopamine in perceptual decision making for a dot motion discrimination task. Under normal conditions, subjects responded more slowly on rewarded trials by increasing the threshold to decision, and subjects showed increased ventral striatal and prefrontal cortex activity predicting increased decision threshold. By decreasing dopamine transmission, using a tyrosine-depleting amino acid mixture, this reward-related corticostriatal activation was reduced, and the correlation with decision threshold was eliminated. Although this study does not employ a learning paradigm,

there is clear indication that dopamine activity is engaged when stimuli are perceived as associated with reward, and that the corticostriatal pathway is key to this.

Dinse et al. (2003) showed evidence that glutamatergic neural transmission governs plasticity in perception. In an exposure-based paradigm, they showed that tactile discrimination was improved under placebo, but when human participants were given an N-methyl-D-aspartate (NMDA) receptor blocker (blocking the NMDA receptor subtype of glutamate receptors), the performance improvements disappeared. Conversely, tactile discrimination improvements were doubled when participants were given amphetamine. Dinse et al. propose that the modulatory role of amphetamine is related to its effect in increasing the levels of dopamine, serotonin and noradrenaline in the brain. Modulation of perceptual learning by glutamatergic neural transmission is further supported by work from Beste et al. (2012) who used a human model of excitotoxic neurodegeneration in Huntington's disease gene mutation carriers. Excitotoxic neurodegeneration in Huntington's disease has been thought to result from the neurotoxic effects of glutamate by excessive neuronal excitation (Olney, 1994), and therefore Huntington's disease gene mutation carriers may represent a human model of increased glutamatergic transmission. In the study by Beste et al. premanifest Huntington's carriers showed faster perceptual learning for a luminance change detection task than controls, and the effect of faster learning was correlated positively with genetic disease load. Glutamatergic neural transmission has previously been shown to be important in long-term potentiation protocols (i.e. LTP-like learning) (Delanoy et al., 1983), therefore suggesting that exposure-based perceptual learning effects are mediated by typical LTP mechanisms.

7.1.8 Synaptic modification as the neural basis for perceptual learning

Long-term potentiation (LTP) is operationally defined as a persistent, experience-dependent strengthening in the efficacy of synaptic transmission resulting from high levels of recent activity. Long-term depression (LTD) by contrast is defined as synaptic efficiency decreases

in response to low rates of stimulation. Modification of synaptic transmission efficiency is widely acknowledged as a neural substrate for learning. Beste et al. (2011) carried out a study linking behavioural perceptual learning to LTP/LTD-like protocols. In this study, subjects were presented with visual bars either side of a fixation cross. LTP/LTD like stimulation was induced by changing the bar luminance by different rates (i.e. 20 Hz with 5 seconds on and 5 seconds off for LTP, and 1 Hz for LTD). The idea is that this is analogous to direct electrical stimulation of neurons in electrophysiological studies of LTP/LTD (Bliss & Collingridge, 1993). Participants performed a luminance change detection task before and after a stimulation/training period. During the stimulation period participants passively viewed the bars while performing a task at central fixation. Participants who received LTP-like 20 Hz stimulation showed improved performance in luminance change detection. By contrast, LTD-like stimulation decreased luminance change detection performance. Using unilateral and bilateral stimulation conditions, this study also showed that the effects of LTP-like stimulation were specific to the visual field location where stimulation occurred, and thus is indicative of changes in early visual cortex. The importance of this study is that it demonstrates that using protocols that induce plasticity at the neuronal level can result in behavioural performance changes for task-irrelevant paradigms. Spike-timing-dependent plasticity (STDP) mechanisms in which synaptic modification occurs in response to correlated spiking of pre- and post-synaptic neurons, and so are dependent on the temporal order of spiking (see Markram et al., 2011 for review), have also been proposed to underlie task-irrelevant learning. This is particularly relevant in the studies of Seitz and Watanabe (2005) described earlier where task-irrelevant learning only occurs if stimulus-driven signs and task-driven signals temporally coincide. Overall these studies strongly suggest that local synaptic changes are mediating behavioural perceptual changes.

7.1.9 Relating synaptic plasticity to task-irrelevant perceptual learning

Performance on standard contrast discrimination tasks frequently show stable performance when repeated, indicating this task may have reached optimal performance during normal

development, or within the time frame of processes operating during the initial testing session (Karni & Sagi, 1993). However, this was later shown not to be the case, as training on contrast Gabors with flanking stimuli showed that the contrast discrimination threshold could be further improved (Adini et al., 2002). No such improvement was observed for conditions without flankers present. This effect was deemed to result from changes in early visual areas triggered by additional inputs provided by lateral interactions between early visual area neurons. Interestingly however, this threshold improvement is only observed for low, subthreshold contrast targets, whereas detection threshold is degraded for high-contrast targets. This result may be explained by assuming inhibitory processes that dominate the high contrast regime and excitatory processes at low contrast (Stemmler et al., 1995; Usher et al., 1999).

Regan and Beverly (1983) reported a series of findings in which adaptation to a sine-wave grating increased thresholds for spatial-frequency discrimination and contrast detection. Spatial-frequency thresholds were most elevated at a test frequency of about twice the frequency of the adapted grating, and not elevated at test frequencies the same as the adapted grating frequency. By comparison, contrast detections were elevated only for gratings with spatial-frequency the same as the adapted grating. This implies that detection and discrimination changes are dissociated along the frequency dimension (Regan & Beverly, 1983). This does not fit the notion that the most active channels determine discrimination, and instead indicates that discrimination is determined by the relative activities of channels or neurons.

Further support for the idea that orientation discrimination is the result of inhibitory interactions between different neuronal populations comes from Regan and Beverly (1985). They showed that adapting to a grating improved orientation discrimination for test gratings parallel to the adapting grating, but degraded orientation discrimination for test gratings inclined 10-20 degrees away from the adapting grating. The theoretical underpinnings for why discrimination thresholds are worse for gratings inclined away from the adapting grating, rather than parallel, are explained by assuming that orientation discrim-

ination is determined by elements whose excitations are comparatively weak (Regan et al., 1985). For example, if the notional excitation pattern of an oriented grating is represented over many orientation-tuned elements as a bell-shaped curve, then the greatest difference in excitation for another grating with a peak close to the original oriented grating, occurs for elements that are substantially displaced from the peaks of the excitation curves. Adaptation then, is proposed to distort the pattern of subsequent excitation by neuronal populations, such that a larger difference between the weighted means of two orientations to be discriminated is produced. In accordance with these findings, Regan and Beverly propose a model in which contrast detection is determined by the most excited orientation-tuned neural elements, whereas supra-threshold orientation discrimination is determined by difference signals between these elements. To elaborate, this means that for detecting a change in stimulus orientation, the most important elements involved in making this discrimination are those elements who relative activity changes most, even though these elements may have comparatively weak excitation. The literature described here provide substantial evidence that perceptual learning is mediated by neuronal processes occurring at the local level, and provide plausible models for how this might be achieved.

7.1.10 Aim of study

Perceptual learning represents an important tool for understanding neuronal processes at the level of the primary visual cortex, as it can be quantified with relative accuracy under tightly controlled experimental conditions. Furthermore, the literature described here provides substantial evidence that behavioural perceptual learning effects reflect actual changes at the neuronal level. The purpose of this study is therefore to use a task-irrelevant perceptual learning (TIPL) paradigm designed to adapt neuronal elements in early visual areas and determine the level of orientation and visual field specificity. This allows testing the hypothesis of whether neuronal adaptation requires active attentional processes, and also the extent to which TIPL differs from, or is similar to, task-relevant perceptual learning.

Previous studies, such as the Gutnisky et al. (2009) study, which investigated task-irrelevant perceptual learning for unattended visual field locations, did not examine the role of reward effects in the improvements observed for orientation discrimination. Furthermore, in the Gutnisky et al task, both the attended and unattended locations during the exposure/training phase were located in the peripheral field, with participants then shifting attention to the attended location to carry out the training task. This is an important point as overt and covert attention are believed to be mediated by different systems (Posner & Peterson, 1990), as well as exogenous and endogenous attention also being reported to have a different neural basis (Mukai et al., 2011). Thus, it is not clear from this paradigm what the extent of any inhibitive effects of selective attention are, and whether or not task-irrelevant stimuli are actually breaking through this inhibitive effect or not. Additionally, the 'unattended' location may have received some attentional allocation during the process of shifting gaze from central fixation to the attended target location. A more appropriate paradigm, which is what will be used here, is for participants to carry out a task at central fixation, while presenting task-irrelevant stimuli in the peripheral field. This is more analogous to the task-irrelevant motion dot studies of Seitz and Watanabe (2005). These motion dot studies however were not designed to adapt early V1 neurons. Given the wealth of studies outlined here indicating both neural plasticity of V1 neurons and effects of reward and attention in V1 (mechanisms proposed to underlie perceptual learning), the paradigm set out here is designed specifically to look at task-irrelevant learning in early visual areas. This allows assessment of the orientation and visual field specificity of learning which is important in interrogating the underlying mechanisms.

Finally, by using a task-irrelevant learning paradigm in which attention can be controlled during exposure training, the role of reward can be manipulated independently of attention. Based on Regan et al.'s previous work on orientation tuning changes of V1 neurons after adaptation, I hypothesise an effect of task-irrelevant learning such that grating orientation discrimination improves when participants are exposed to gratings at 45°, but not gratings 15° away from 45°. I would expect no such improvement for a control condition in which no

task-irrelevant grating is present during the training phase, and I would also not predict an improvement in orientation discrimination at visual field locations other than the location used during training. Furthermore, I would hypothesise that rewarding trials during the training phase would bring about a more dramatic improvement in perceptual learning as the task-irrelevant stimuli break through the inhibitory attentional surround. In summary, this study represents a novel way of illustrating how attention and reward interact in perception and learning in early sensory areas, and the extent to which perceptual learning can occur for task-irrelevant stimuli.

7.2 Methods: TIPL for orientation discrimination (No reward)

7.2.1 Participants

Twenty-four human volunteers (14 female, 10 male, age mean 24.1 years ± 3.4, range 19–30 years) gave written informed consent as approved by the Oxford Central University Research Ethics Committee (CUREC). All subjects had normal or corrected-to-normal visual acuity and no known neurological deficits. All volunteers were remunerated equally for their participation.

7.2.2 Apparatus

Stimuli were presented on a 13.4" CRT monitor (Eizo FlexScan T961) at a resolution of 1440 x 900 with a refresh rate of 60 Hz (non-interlaced). The mean background luminance was 80 cd/m^2, mean stimulus luminance was 115 cd/m^2. Custom experimental software was written in MATLAB (The Mathworks, Inc., version 8.0.0.783); the Psychophysics Toolbox extensions were utilized (Brainard, 1997; Pelli, 1997). The monitor was viewed at a distance of 50 cm. Stimuli were viewed binocularly in a darkened room. Any corrective lenses or contacts normally worn by the participants were worn during the experiment.

7.2.3 Design and stimuli

The study followed a test-training-retest design over the course of 5 days. On Day 1, participants experienced a 30-minute test-phase followed by a 15-minute training-phase. On each of Days 2-4, participants underwent the same 15 minutes of training-phase trials as on Day 1. On Day 5, participants experience the same training-phase trials, followed by the test-phase trials from Day 1. Performance on pre-training and post-training trials was

then compared and analysed. Participants were given an 80-trial practice session before the initial test-phase on Day 1 to familiarize them with the task.

7.2.3.1 Test Phase

Participants performed 8 blocks (80 trials/block) of an orientation discrimination task in which they were required to press the appropriate keyboard arrow key depending on whether the orientation of the presented grating was rotated clockwise or anti-clockwise relative to the standard orientation. The standard orientation was dependent on the block type. There were two block types, a *positive orientations* block, for which the standard orientation was +45° relative to vertical, and a *negative orientations* block, for which the standard orientation was -45° relative to vertical. For trials in the *positive orientations* block type, participants had to press the left arrow key for gratings oriented anti-clockwise from +45°, and the right arrow key for gratings oriented clockwise from +45°. For trials in the *negative orientations* block type, participants had to press the left arrow key for gratings oriented anti-clockwise from -45°, and the right arrow key for gratings oriented clockwise from -45°. No accuracy feedback was given to the subjects (See Appendix B for example instruction sheet).

Sixteen different orientations of gratings were used, divided among the two block types. The orientations used in the *positive orientations* group were: 35°, 39°, 42°, 44°, 46°, 48°, 51°, 55°. The orientations used in the *negative orientations* group were: -35°, -39°, -42°, -44°, -46°, -48°, -51°, -55°. Block type was altered sequentially with the starting block type varied pseudorandomly. Break screens for participants to refresh their eyes were presented at the end of each block. These were grey screens with black writing instructing participants to take a minimum of 10 seconds break.

At the beginning of each trial a central white fixation cross is presented. After a variable stimulus onset asynchrony (SOA) between 100-600 ms, a single grating of one of the eight

possible orientations from within the current block type was presented at one of four peripheral visual field locations (at 6° eccentricity). The fixation cross remained on during this time and subjects were instructed not to break fixation from the fixation cross. The fixation cross and grating were presented together for 150 ms against a mid-grey background, after which time the grating was removed and the central fixation cross was replaced by a question mark, prompting the participant for a response (500ms delay between trials) (Fig. 7.1).

The grating stimuli were Gabor patch gratings at 25% Michelson contrast, 2 cycles per degree (subtending 2.5° visual angle in diameter) of fixed phase, Gaussian mask radius = 1.5 cycles. All participants experienced 40 practice trials prior to commencement of the study, 20 of each block type. The post-training re-test phase was the same as the pre-training test phase, but the starting block type was altered to the opposite starting block type from that of the pre-training phase.

7.2.3.2 Training Phase

Participants performed a Rapid Serial Visual Presentation (RSVP) task at central fixation against a mid-grey background, while a task-irrelevant grating was presented in a single peripheral field location (Upper-Right - '*Location 1*'). During each trial (100 trials/day for 5 days), a series of fourteen randomly chosen letters from the alphabet are presented sequentially for 150 ms per letter. Each letter was presented pseudo-randomly as either black or white. Each trial lasted for 2100 ms. A response screen was presented 150 ms after the final letter in each trial and then a trial feedback screen for 2000 ms following the participants response. Participants responded with a left arrow key if there was an even number of white letters presented during that trial, or a right arrow key if there was an odd number of white letters. Between 300-1800 ms during the trial, a single grating, of size and contrast as in the test-phase, was presented for 1500 ms in the Upper-Right (*Location 1*) visual-field location at 6° eccentricity. The orientation of the grating was

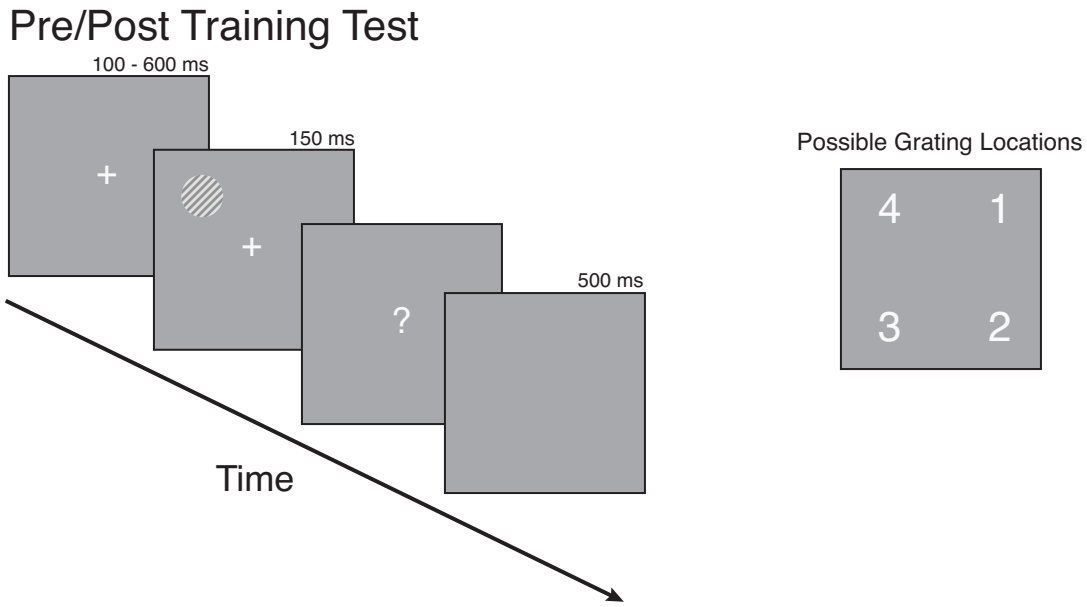

Figure 7.1: **Test/Re-Test Phase task design.** A fixation cross and a grating with pseudo-random orientation were presented together for 200 ms after SOA 100-600 ms. The grating appeared pseudo-randomly in one of four visual field locations (at 6° eccentricity): Location1 = Upper-Right, Location 2 = Lower-Right, Location 3 = Lower-Left, Location 4 = Upper-Left (grating in Location 4 shown here above). A response screen with a '?' symbol was then displayed until the participant made a response regarding whether the grating was oriented clockwise or counter-clockwise from +45° or -45°. There were 640 trials in total for both the Pre-Training Test Phase and the Post-Training Test Phase.

either +45°, or trial-alternating +30° and +60° (corresponding to 15° either side of 45°) depending on the training condition. There were three different training conditions: +45° group, +30°/+60°, and a No-Grating control group with 8 participants in each condition. The grating was irrelevant to the task the subjects were performing (Fig. 7.2).

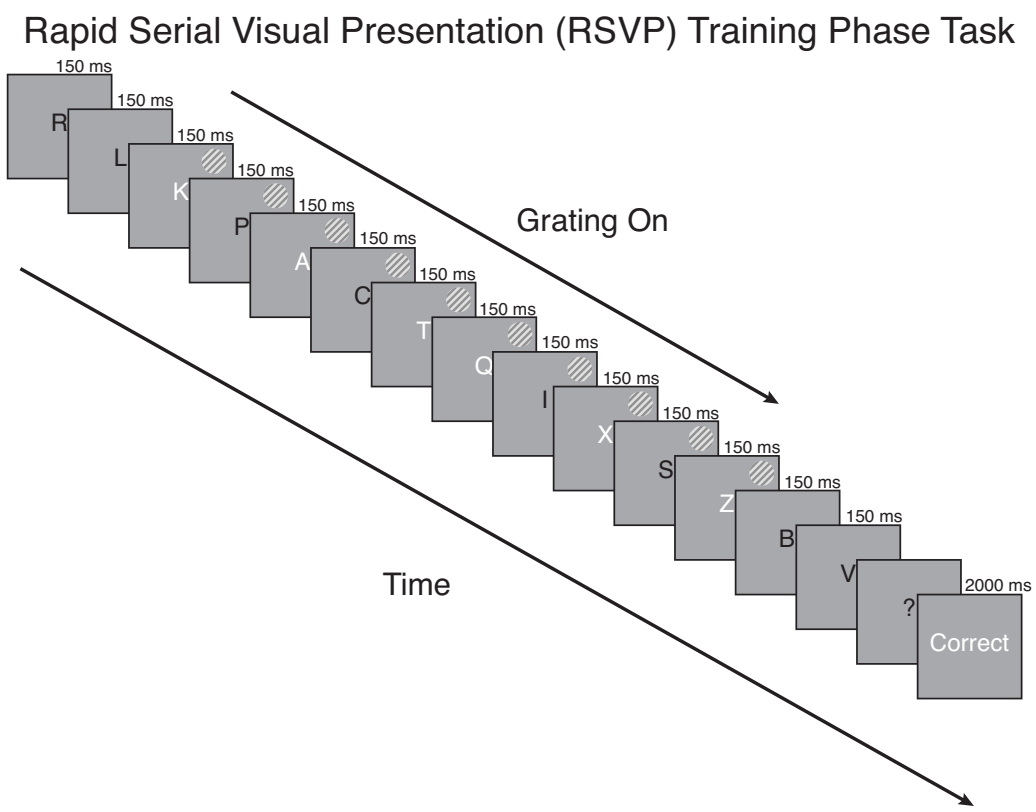

Figure 7.2: **Training phase design.** Participants experienced a Rapid Serial Visual Presentation (RSVP) task. During each trial (100 trials, one block per day), a series of fourteen randomly chosen letters were presented sequentially for 150 ms per letter. Each letter was presented randomly as either black or white. A response screen is presented 150 ms after the final letter in each trial. Participants responded with a left arrow key if there was an even number of white letters presented during that trial, or a right arrow key if there was an odd number of white letters. Between 300-1800 ms during the trial, a single Gabor patch grating, of size and contrast as during the test phase, was presented for 1500 ms in the Upper-Right (Location 1) 6° eccentricity visual-field location. The grating was irrelevant to the RSVP task the subjects were performing.

7.2.4 Analysis procedures

Accuracy and reaction times were recorded for each participant for both pre-training and post-training trials. Individual psychometric functions (PMFs) for each participant, for both pre-training and post-training trials, were fit with cumulative normal distributions. The shape of the psychometric function depicts the relationship between degrees of orientation of the grating away from 45° (stimulus strength), and the proportion of rightward responses (participants choice to press the right arrow key). Sensory threshold, measured in degrees away from 45°, was taken as 1 standard deviation of the fitted curve. A significantly lower threshold therefore indicates better orientation discrimination. Each participant's overall pre-training and post-training thresholds were recorded, as well as their orientation-specific and location-specific thresholds.

7.3 Results: TIPL for orientation discrimination (No reward)

7.3.1 Effect of perceptual learning

The mean discrimination thresholds at pre-training and post-training are shown in Figure 7.3 for the three groups on all tested orientations. A 2 x 3 mixed effects ANOVA was carried out on the results (pre/post training thresholds x training condition). There was a significant difference in thresholds before and after the training phase ($F(1,2) = 16.375$, $p < 0.001$). There was no significant difference in thresholds across groups ($F(2,21) = 0.380$, $p = 0.689$), nor was there any significant interaction ($F(2,21) = 0.635$, $p = 0.540$). The results indicate that orientation discrimination was no different across groups before training, and that orientation discrimination improved similarly for all conditions after training. Thus, there was an improvement in discrimination thresholds irrespective of the training condition, including for the No grating 'dummy training' control condition in which no grating was present during the RSVP training task. This suggests that there is a general performance related improvement as a result of practice or familiarity with the test-task (see Appendix A for pre/post-training psychometric functions for each individual).

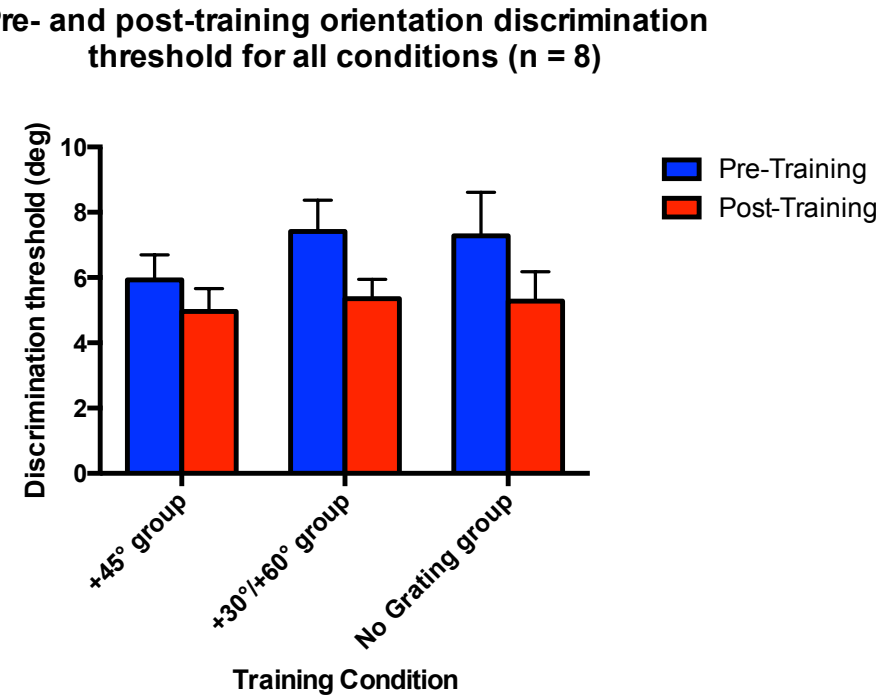

Figure 7.3: Mean orientation discrimination thresholds for each of the 3 groups before and after training (each group n = 8). Errors bars show standard error of the mean (SEM).

7.3.2 Effect of perceptual learning specific to trained orientation

The +45° and +30°/+60° training conditions only presented gratings in a positive orientation, however, participants are tested before and after training for their ability to discriminate both positive and negative oriented gratings. To determine whether any training effect that is specific to the exposed orientation is being obscured by the general practice related effect, analyses were carried out for thresholds computed from only positively oriented gratings. A 2 x 3 mixed effects ANOVA was carried out. There was again a significant difference in thresholds before and after training ($F(1,2) = 14.864$, $p < 0.001$). But no significant difference in thresholds across groups ($F(2,21) = 0.673$, $p = 0.521$), nor any significant interaction ($F(2,21) = 1.721$, $p = 0.203$). If there was an orientation specific perceptual learning effect that is being masked by a general practice related improvement, then we would expect a significantly larger improvement in orientation discrimination for the +45° and +30°/+60° training conditions compared with the

No grating control condition, as participants in the +45° and +30°/+60° were exposed to positively oriented gratings during the RSVP training task. These results here do not indicate that there is an effect of perceptual learning specific to grating orientation.

7.3.3 Effect of perceptual learning specific to trained location

The results already presented combine data from all the tested locations, and thus may be obscuring a location-specific effect of the perceptual learning. To investigate whether perceptual learning effects may have been specific to the single location trained during the training phase, thresholds were analyzed separately for each location. To simplify the analysis, the change in threshold between the pre-training discrimination threshold, and the post-training discrimination threshold was computed for each participant to give a single 'threshold change' value. The post-training threshold was subtracted from the pre-training threshold. Therefore, a positive value indicates an improvement in orientation discrimination performance.

Figure 7.4 plots the mean change in threshold for each group at each location. Location 1 is the trained location, i.e. the location (Upper-Right) at which a grating appeared during the RSVP training phase for the +45° and +30°/+60° groups. No grating was present at any location during the 'dummy training' phase for the No grating group. Thus, we might expect discrimination thresholds to improve similarly at each location in the No grating control group, but to improve significantly more at Location 1 for the +45° and +30°/+60° groups. Figure 7.4 shows that on average orientation discrimination improved for each condition at every location. A 3 x 4 mixed ANOVA for group x location was carried out. There was no significant main effect of location ($F(3,63) = 1.40$, $p = 0.25$), nor was there a significant main effect of group ($F(2,21) = 0.47$, $p = 0.069$). The interaction between group and location was also not significant ($F(6,63) = 0.45$, $p = 0.84$). The results therefore suggest that the perceptual learning effect is independent of location and the training condition. However, again these results do not examine effects specific to both

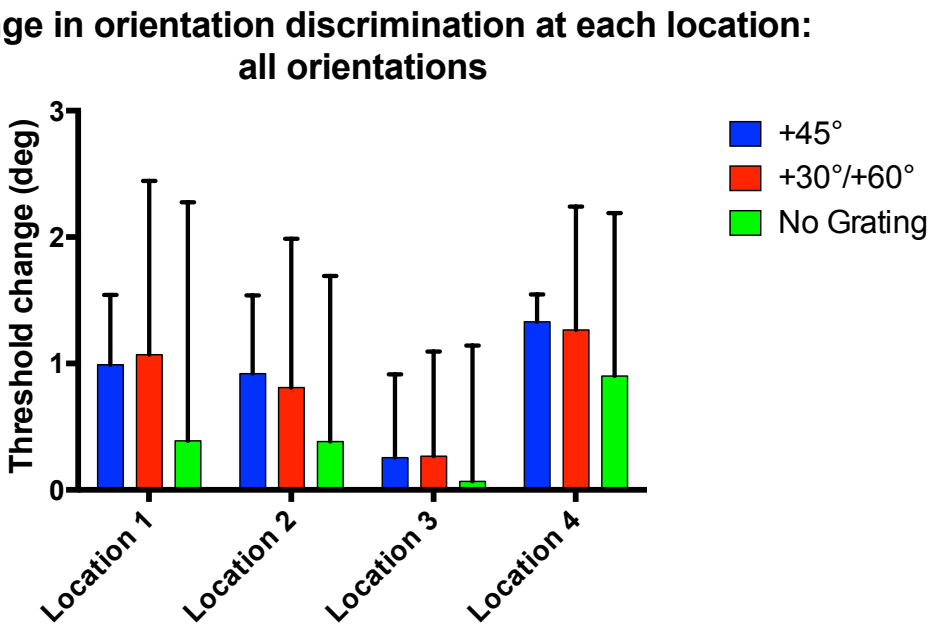

Figure 7.4: Mean change in orientation discrimination thresholds for each of the 3 groups from before and after training at each location (each group n = 8, trials at each location = 160). Change in threshold is post-training threshold subtracted from pre-training threshold, therefore a positive value indicates an improvement in orientation discrimination. Threshold is measured in degrees and is the ability to discriminate orientation away from 45°. Location 1 is the trained location (Upper-Right visual field). Location 2 is Lower-Right visual field, Location 3 is Lower-Left visual field, Location 4 is the Upper-Left visual field. Error bars show SEM.

location and orientation, as test trials for both positive and negative orientations have been averaged together for each participant. Therefore to investigate the presence of perceptual learning effects specific to location and orientation, the change in discrimination threshold for only positive orientations at each location are analyzed in the following section.

7.3.4 Effect of perceptual learning specific to trained location and trained orientation

As described previously the results looking at location specific effects of perceptual learning might also be obscured by the averaging of positive and negative orientation data. Thus, the change in threshold between pre-training and post-training was computed for each participant for only positive orientations that were tested, at each location, for each group. Figure 7.5 plots the mean change in threshold for each group at each location for positive orientations only. As before, Location 1 is the trained location. No grating was present at any location during training for the No grating group. Thus, we might expect discrimination thresholds to improve similarly at each location in the No grating control group, but to improve significantly more at Location 1 for the +45° and +30°/+60° groups. The results shown in Figure 7.5 show that for all groups there was a mean improvement in orientation discrimination thresholds at Location 1 (trained location) and Location 4, however, there was no such improvement at Location 2 or Location 3.

A 3 x 4 mixed ANOVA for group x location was carried out. There was no significant effect of location ($F(3,6) = 1.93$, $p = 0.13$), nor was there a significant effect of group ($F(2,21) = 1.29$, $p = 0.30$. However, there was a significant interaction ($F(6,63) = 2.70$, $p = 0.048$). This means there were significant differences between the groups depending on the location. To determine any differences between the groups at each location, a one-way between-subjects ANOVA (groups) was carried out separately for each location.

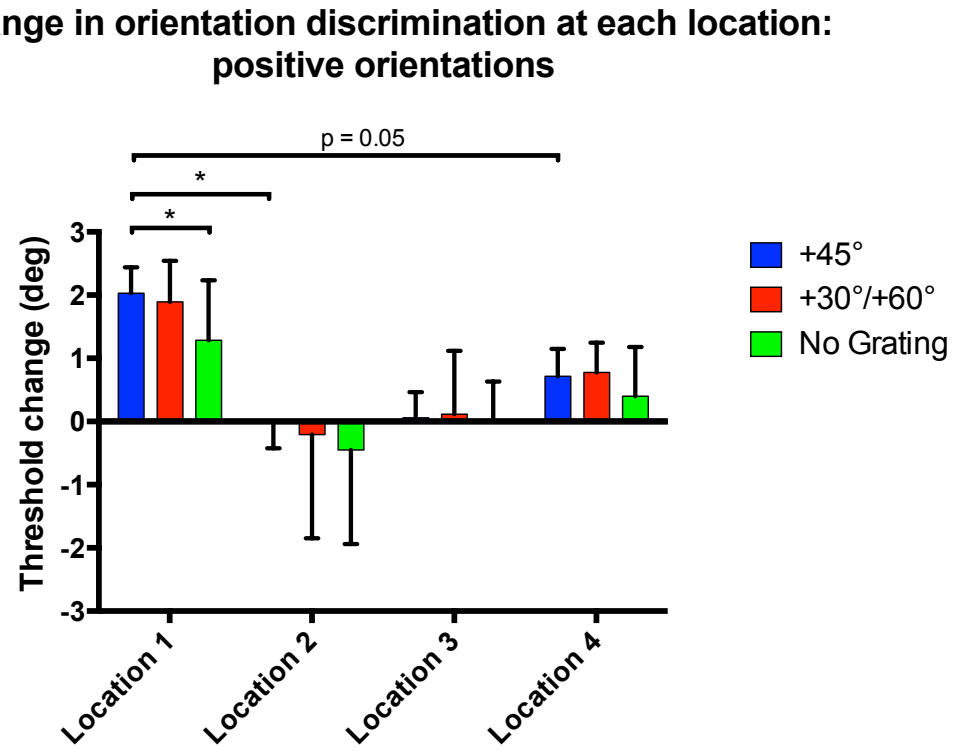

Figure 7.5: Mean change in orientation discrimination thresholds for each of the 3 groups from before and after training at each location (each group n = 8, trials at each location that were positive orientations = 80). Change in threshold is post-training threshold subtracted from pre-training threshold, therefore a positive value indicates an improvement in orientation discrimination. Threshold is measured in degrees, and is the ability to discriminate orientation away from 45°. Location 1 is the trained location (Upper-Right visual field). Location 2 is Lower-Right visual field, Location 3 is Lower-Left visual field, Location 4 is the Upper-Left visual field. A 3 x 4 mixed ANOVA revealed a significant interaction for group x location. To isolate the effect a one-way between-subjects ANOVA (group effect) was carried out at each location. Tukey's post-hoc test was used to test for pairwise comparisons of the between-subjects ANOVA. A one-way within subjects ANOVA (location effect) was also carried out for each group to look at the effect of location. Bonferroni corrected comparisons were carried out for the within-subjects ANOVA pairwise comparisons. * denotes significance at $p < .05$. Error bars show SEM.

There was a significant difference between the groups at Location 1 ($F(2,23) = 4.27$, $p = 0.028$). Tukey's HSD post-hoc tests revealed that that difference between the +45° and +30°/+60° groups was not significant ($p = 0.91$), nor was the difference between the +30°/+60° and the No Grating group significant ($p = 0.08$). However, the difference between the +45° and the No Grating group was significant ($p = 0.03$). There was no significant difference between the groups at Location 2 ($F(2,23) = 1.63$, $p = 0.22$). There was also no significant difference between the groups at Location 3 ($F(2,23) = 0.18$, $p = 0.85$). Finally, there was also no significant difference between the groups at Location 4 ($F(2,23) = 2.45$, $p = 0.11$) (Fig. 7.5).

To determine any differences between the locations for each group separately, a one-way repeated measures ANOVA (location) was carried out comparing the threshold change at each location for each group in turn. There was a significant difference across locations for +45° ($F(3,21) = 5.86$, $p = 0.005$). Bonferroni corrected pairwise comparisons revealed a significant difference in threshold change for Location 1 vs. Location 2 ($p = 0.018$), while the significance of Location 1 vs. Location 4 was $p = 0.05$. The pairwise comparisons for Location 1 vs Location 3 was not significant ($p = 0.07$). No other pairwise comparisons were significant (Location 2 vs Location 3, $p = 1.00$; Location 2 vs Location 4, $p = 1.00$; Location 3 vs Location 4, $p = 1.00$). There were no significant differences across location for the +30°/+60° group ($F(3,21) = 1.44$, $p = 0.26$). There were also no significant differences across location for the No Grating group ($F(3,21) = 2.192$, $p = 0.12$) (Fig. 7.5).

7.4 Discussion: TIPL for orientation discrimination (No reward)

The results presented here indicate a number of findings that need to be examined. The first of these is that orientation discrimination improved significantly at the second time of testing, five days after the initial testing phase, for all groups. The unexpected finding was that there was significant improvement even in the No Grating control group (Fig. 7.3). This suggests that there may have been a general performance related improvement as result of practice or familiarity with the test task. Participants were given an 80-trial practice session before testing on Day 1 to allow for any practice effects to stabilise, but this may not have been enough. It is not clear from just these initial results whether the improvement in performance reflects perceptual learning, or forms of cognitive learning, strategy selection, or motor learning.

Improvements in performance on perceptual tasks do not necessarily indicate perceptual learning. On the other hand, improvements in performance for the No Grating control condition also do not preclude the presence of perceptual learning effects. There are three possible interpretations of the initial results from Figure 7.3: The first is that no perceptual learning occurred, and the improvements in performance were due to 'higher order' forms of learning, such as cognitive learning, establishing of task rules, associations and strategies, and motor learning. The second interpretation is that although the presentation of the grating during the RSVP training did not appear to have any effect, the act of performing the RSVP task itself may have contributed to perceptual learning through mechanisms such as external noise exclusion or internal noise suppression (Lu & Dosher, 1998a). Thus, in this interpretation the improvements in orientation discrimination are the result of perceptual learning. The third interpretation is that there was a task-irrelevant perceptual learning effect as a result of the simultaneous grating presentation during the RSVP task, but that this perceptual learning effect was masked by the presence of higher-order, cognitive/practice related learning effects.

An extension of this work could be to have a condition in which participants perform the test and re-test phase five days apart with no training tasks in between. This would help determine more precisely what the effect of the RSVP training task was. However, this is not strictly necessary as the key point is that improvements in orientation discrimination can more unambiguously be attributed to perceptual learning if the improvements show specificity to either stimulus features (e.g. orientation) or to visual field/retinal location (Dosher & Lu, 1999). Therefore, in order to determine whether the third interpretation of the initial results is the correct one, I went on to analyse orientation discrimination thresholds specific to orientation and location (Fig. 7.4. & 7.5). The results here give a more genuine measure of whether task-irrelevant perceptual learning occurred (although there is evidence from studies described in the introduction of this chapter that do suggest perceptual learning can be transferred to different locations, e.g. Xiao et al., 2008).

The results from investigating the effect of TIPL specific to orientation and location are slightly more confusing at first glance. When only discrimination thresholds for positive orientations are analysed, the only significant differences between the groups was between the +45° group and the control group at Location 1, and the only significant difference between locations was between Location 1 and Location 4 for the +45° group. This appears to suggest that there is an orientation and location specific effect of perceptual learning that is the result of task-irrelevant passive training with a +45° grating presented during an RSVP task at central fixation. This result is a key finding of the study, and is evidence in support of the hypothesis that perceptual learning can occur for task-irrelevant stimuli designed to adapt neurons in early visual areas. However, there are several outstanding questions. Firstly, why was there no difference between the +45° group and the +30°/60° group, and why there was no difference between the +30°/60° and the No Grating control group.

The purpose of the +30°/+60° group was to present gratings during training that were 15° either side of +45°. During the test phase the task was to discriminate gratings based on their orientation away from +45° (either less than +45° or more than +45°). Based on

Regan et al.'s work (1985), it was predicted that orientation discrimination would improve when trained with gratings at +45° but not for +30° or +60° gratings. As described in the introduction, this is because orientation discrimination is proposed to be the result of inhibitory interactions between different neuronal populations. Regan & Beverly (1985) showed that adapting to a grating improved orientation discrimination for test gratings parallel to the adapting grating, but degraded orientation discrimination for test gratings inclined 10-20 degrees away from the adapting grating. The results of the current study do not appear to either match or contradict Regan & Beverly's findings, as there was no difference between to +30°/+60° groups vs. + 45° which we might have expected, but there was also no difference between the +30°/+60° and the No Grating control group which would match the idea that perceptual learning does occur for gratings inclined 10-20 degrees from the adapted gratings (+30°/+60°). The most appropriate interpretation of these results is that there was not enough statistical power to determine either way whether perceptual learning occurred for the +30°/+60°.

The other significant effect found in this study was for Location 1 vs Location 4 in the +45° group. Again this result is slightly confusing as the difference between improvement at Location 1 and Location 2 suggests a location specific effect of perceptual learning that does not transfer to the lower visual field if trained with gratings in the upper visual field. The difference between Location 1 and Location 4 almost reached significance ($p = 0.05$), suggesting that the perceptual learning also does not transfer to the contralateral visual hemifield. However, the fact that there was no significant difference between Location 1 and Location 3, which is also contralateral and in the lower visual hemifield, means no unambiguous conclusions can be drawn. Again, it would appear that the study lacks sufficient statistical power to distinguish the presence and/or extent of location specificity. Overall, the results of this analysis indicate that this paradigm induces a form of task-irrelevant perceptual learning, the effect of which is masked by practice related effects, but can be uncovered by analyzing orientation and location specific effects. The fact that the improvements were greatest for the trained orientation and location suggests

perceptual learning, and that the locus of perceptual learning is early on in the visual stream of processing, as the stimuli were designed to adapt neuronal elements in primary visual cortex (V1). However, the results are not straightforward as participants in the control condition also exhibited a significant improvement in performance, thus it is hard to determine whether practice effects masked out orientation/location specific effects, or whether task-irrelevant perceptual learning exhibits a degree of transferability to different locations or orientations.

It is important to note that there were no reward conditions involved in the present analyses (although TIPL could theoretically be gated by the reward signal provided during the RSVP task via the accuracy feedback). Previous literature indicates that TIPL effects occur only for rewarded conditions, as reward has a modulatory effect on attention Wang et al. (2014). Wang et al. showed that task-irrelevant reward-associated stimuli could capture attention even when presented within the inhibitory surround of attentional capture. When the task-irrelevant stimuli were not rewarded, no interference of attention occurred. Their study is based on theories that propose there is an inhibitory region around attended objects, and that distractors in this region fail to capture attention or cause interference (Cutzu & Tsotsos, 2003; Hopf et al., 2006a; Mounts, 2000). In my study, the task-irrelevant stimuli were not previously associated with any reward, and so are likely to be inhibited by attention on the central RSVP task. A monetary reward during the RSVP training task might facilitate the learning of task-irrelevant stimuli presented concurrently with reward-paired targets. The next phase of this study introduces a reward conditions in which performance during the RSVP task is rewarded.

7.5 Methods: TIPL for orientation discrimination (Reward study)

7.5.1 Participants

Ten human volunteers (5 female, 5 male, mean age 24.4 years ± 2.7, range 22–30 years) gave written informed consent as approved by the Oxford Central University Research Ethics Committee (CUREC). All subjects had normal or corrected-to-normal visual acuity and no known neurological deficits. All volunteers were remunerated equally for their participation.

7.5.2 Design and stimuli

The design and stimuli in the reward study were the same as in the non-rewarded perceptual learning paradigm described previously, except that participants were informed that for every trial they got correct during the RSVP training phase, £0.05 would be added to their payment for participating in the study. Thus, there was a monetary reward available on RSVP task. Only two conditions were tested here, a +45° (n = 6) and a No grating condition (n = 4).

7.6 Results: TIPL for orientation discrimination (Reward study)

The mean discrimination thresholds at pre-training and post-training are shown in Figure 7.6 for the two groups on all tested orientations. A 2 x 2 mixed effects ANOVA was carried out on results (pre/post training thresholds x training condition). There was a significant difference in thresholds before and after training ($F(1,8) = 24.22$, $p < 0.001$). There was no significant difference in thresholds across groups ($F(1,8) = 4.67$, $p = 0.06$), nor was there any significant interaction ($F(1,8) = 4.41$, $p = 0.07$). The results indicate that orientation discrimination was no different across groups before training, and that orientation discrimination improved similarly for all conditions after training. Thus, there was again an improvement in discrimination thresholds irrespective of the training condition.

The change in threshold between the pre-training discrimination threshold, and the post-training discrimination threshold was computed for each participant to give a single 'threshold change' value. The mean threshold change for each group was then plotted for each group at each visual location (Fig. 7.7) to investigate location specific effects.

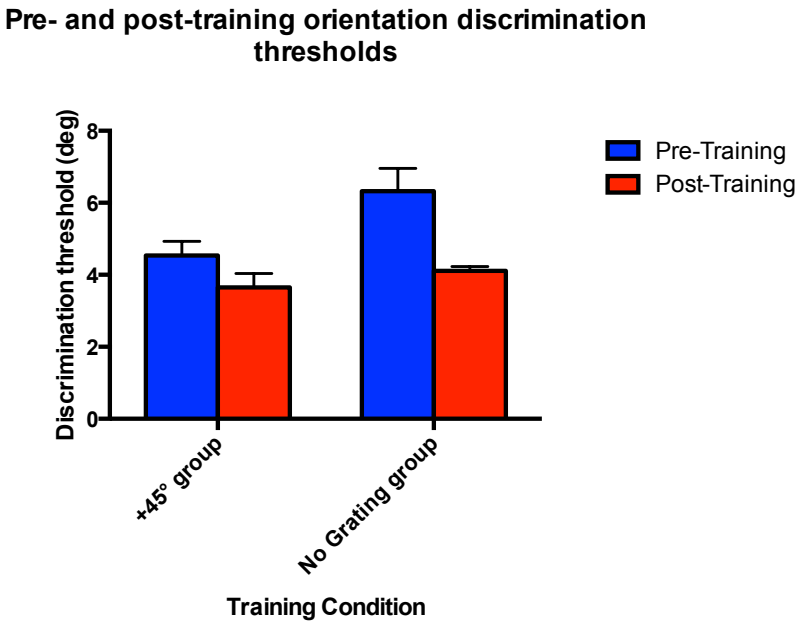

Figure 7.6: Mean orientation discrimination thresholds for both groups before and after training (+45° group: n = 6, No grating group: n = 4). Error bars show SEM.

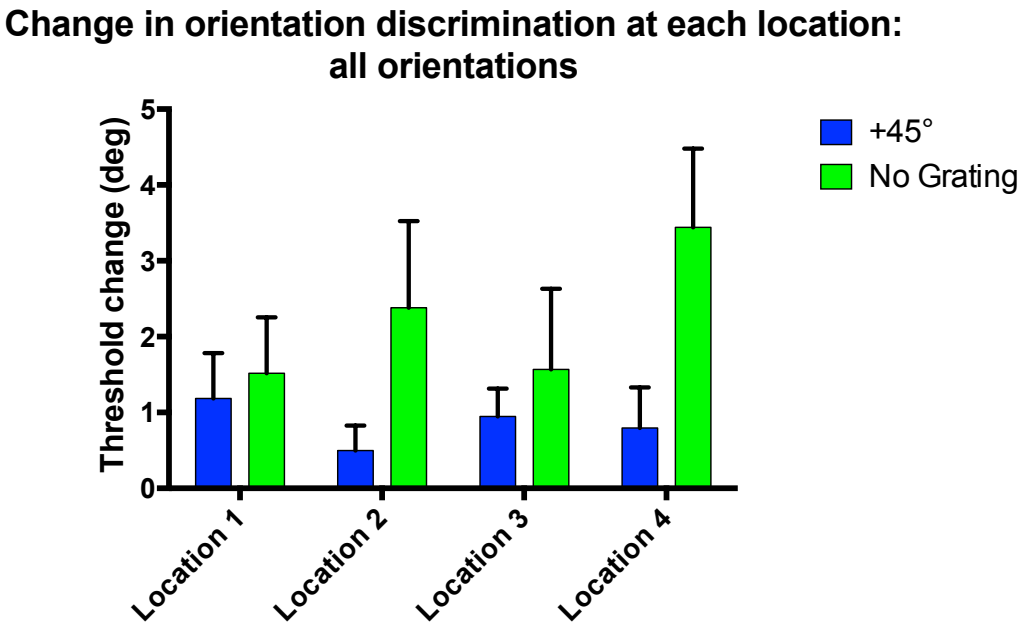

Figure 7.7: Mean change in orientation discrimination thresholds for both groups from before and after training at each location (+45° group, n = 6; No grating group, n = 4). Change in threshold is post-training threshold subtracted from pre-training threshold. Positive value indicates an improvement in orientation discrimination. Threshold is measured in degrees and is the ability to discriminate orientation away from 45°. Location 1 is the trained location (Upper-Right visual field). Location 2 is Lower-Right visual field, Location 3 is Lower-Left visual field, Location 4 is the Upper-Left visual field. Error bars show SEM.

A 2 x 4 mixed ANOVA for group x location was carried out. There was no significant main effect of location ($F(3,24) = 0.73$, $p = 0.54$), nor was there a significant main effect of group ($F(1,8) = 5.32$, $p = 0.05$). The interaction between group and location was also not significant ($F(3,24) = 1.40$, $p = 0.27$). The results therefore suggest that the perceptual learning effect is independent of location and the training condition. The mean change in threshold is higher on average at each location for the No Grating control than the mean change in threshold for +45° group, however, this difference was not significant. Again, these results do not examine effects specific to both location and orientation, as test trials for both positive and negative orientations have been averaged together for each participant. Therefore to investigate the present of a perceptual learning effect specific to location and orientation, the change in discrimination threshold for only positive orientations at each location were then analyzed in the following section.

The change in threshold between pre-training and post-training was computed for each participant, for only positive orientations that were tested, at each location. Figure 7.7 plots the mean change in threshold for each group at each location for positive orientations only. As before, Location 1 was the trained location. A 2 x 4 mixed ANOVA for group x location was carried out. There was no significant main effect of location ($F(3,24) = 1.03$, $p = 0.40$), nor was there a significant main effect of group ($F(1,8) = 1.77$ $p = 0.22$). The interaction between group and location was also not significant ($F(3,24) = 1.25$, $p = 0.32$).

An independent t-test on the change in orientation discrimination threshold revealed no significant difference between the reward vs non-reward +45° groups for positive orientations at Location 1 ($p = 0.96$), nor at any other locations. Finally, additional analyses were carried out on RSVP task performance, and compared with performance on the RSVP task during the non-rewarded version of the study. Mean RSVP task accuracy was significantly higher for non-reward groups (mean accuracy = 0.80, SD ± 0.19, n = 24) vs. reward groups (mean accuracy = 0.76, SD ± 0.15, n = 10; independent t-test, p = 0.004). However, if only +45° groups are compared then there is no significant difference between RSVP accuracy scores (reward +45° group mean accuracy = 0.68, SD ± 0.12 vs.

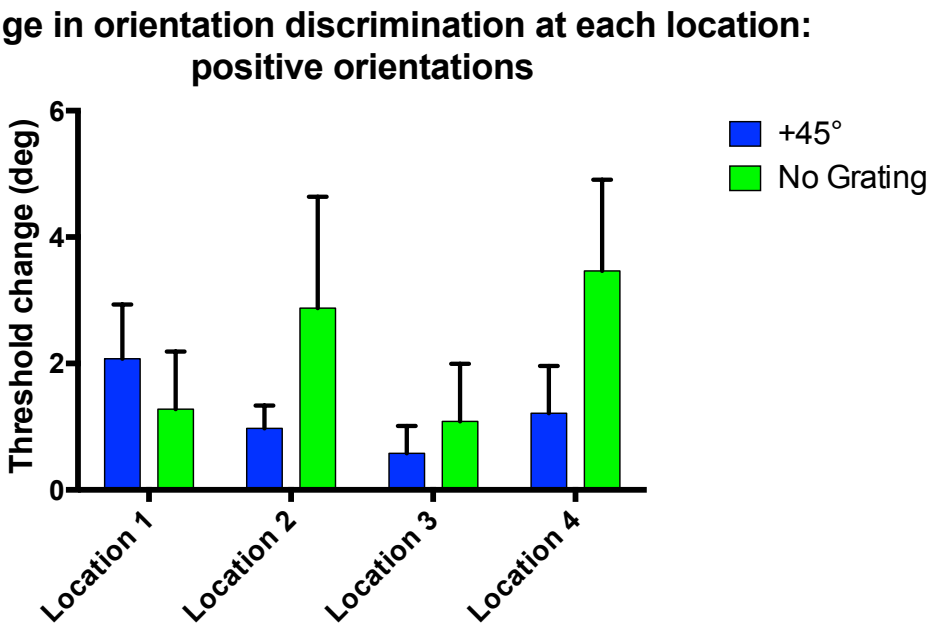

Figure 7.8: Mean change in orientation discrimination thresholds for each of the 3 groups from before and after training at each location (each group n = 8, trials at each location that were positive orientations = 80). Change in threshold is post-training threshold subtracted from pre-training threshold, therefore a positive value indicates an improvement in orientation discrimination. Threshold is measured in degrees, and is the ability to discriminate orientation away from 45°. Location 1 is the trained location (Upper-Right visual field). Location 2 is Lower-Right visual field, Location 3 is Lower-Left visual field, Location 4 is the Upper-Left visual field.

non-reward +45° group mean accuracy = 0.76, SD ± 0.07; independent t-test = 0.17).

7.7 Discussion: TIPL for orientation discrimination (Reward study)

Overall, the results of the reward study indicate that despite an improvement in orientation discrimination after training, this improvement is not specific to training group, orientation, or location, and therefore most likely reflects practice-related effects. Although this was not the predicted finding, the finding that no perceptual learning occurred when the RSVP task was rewarded fits with the work of Wang et al. (2014). In their study they showed that that task-irrelevant reward-associated stimuli could capture attention when presented within the inhibitory surround of attentional capture. When the task-irrelevant stimuli were not rewarded, no interference of attention occurred. Their study is based on theories that propose there is an inhibitory region around attended objects, and that distractors in this region fail to capture attention or cause interference (Cutzu & Tsotso, 2003; Hopf et al., 2006; Mounts, 2000). In the current study, it is actually the alphanumeric stimuli of the RSVP task that is paired with reward as opposed to the gratings, so there is no reason that the task-irrelevant grating stimuli should break the inhibitory surround of the RSVP stimuli.

In conclusion, rewarding the RSVP task did not facilitate the expression of any task-irrelevant perceptual learning effects. It is not possible to conclude, however, that reward abolished the orientation and location specific perceptual learning effect that was present in the non-reward version, as the improvement in threshold was no different at Location 1 for the reward +45° vs. the non-reward +45° group (positive orientations only). This is likely to be due to the fact that the gratings presented during the RSVP training were not appropriately paired with the reward; the reward instead being paired with the alphanumeric RSVP stimuli. In future work, what would be required to ensure that the task-irrelevant stimuli is paired with reward, would be to have a preliminary task that trains participants to associate the presence of a grating with a reward. It was thought that in the current setup, the fact that presentation of the grating is temporally linked to

the rewarded RSVP stimuli would be enough to enhance perceptual learning, however, this does not appear to be the case. Together the results of this chapter highlight a common phenomenon in studies of perceptual learning but one that is not often discussed, which is that perceptual learning is likely to be the result of distributed learning, with some aspects of learning occurring in low-level sensory areas, and other aspects the result of changes in higher-level areas concerned with aspects such as attention, decision-making, and strategy selection. In the current results I find evidence to suggest that the task-irrelevant perceptual learning paradigm induces perceptual learning effects in addition to practice-related effects. However if, as some studies have shown, perceptual learning effects are transferable and generalizable (Xiao et al., 2008; Wang et al., 2012; Green & Seitz, 2015), then distinguishing between the mechanisms involved in perceptual learning, from those involved in more cognitive learning becomes increasingly difficult. This is a complex and interesting question that will certainly require much further work to resolve, however, task-irrelevant paradigms that can separate attention, reward, and stimulus presentation aspects involved in learning offer a promising route for investigating the mechanisms of perceptual learning.

Chapter 8

Conclusions and future directions

Diffusion-weighted imaging with probabilistic tractography is a technique that is still in its relative infancy when compared to the more established techniques for studying the brain such as tract tracing, electrophysiology, and even fMRI. As a result, no consensus has emerged on the best methods for analysing diffusion imaging, nor for how best to carry out tractography. A range of models exists for representing the anisotropy in each brain voxel, such as diffusion tensor imaging (DTI, Basser et al., 1994a), Q-ball (Tuch, 2004), constrained spherical deconvolution (CSD, Tournier et al., 2007), and ball and stick models (B&S, Behrens, et al., 2007). Furthermore, the fibre-tracking algorithm employed can be either deterministic or probabilistic. While probabilistic tractography incorporates the expected uncertainty into the tracking, and therefore accounts for the reproducibility of tracking trajectories, deterministic methods are still widely employed and are shown to accurately reproduce white matter tracts (Thomas et al., 2014). Studies have generally focussed on comparing different diffusion models and tractography techniques. Relatively few studies have systematically evaluated how the parameters concerning streamline length and streamline curvature influence the outcome of tractography. Some studies have explored the effect of step size (Parizel et al., 2007; Tournier et al., 2011; Côté et al., 2013) and streamline curvature (Tournier et al., 2002; Côté et al., 2013; Takemura et al., 2016).

However, these studies usually involve deterministic tractography as opposed to probabilistic tractography, do not explore the overall effect of streamline length, and are often modelled on simulated data.

In the first part of this thesis I investigated the quantitative impact of these parameters on a real-world application of probabilistic tractography – the prediction of a topographic map in the LGN and V5/MT based on connections to different parts of V1 in a single brain. A similar analysis was also carried out for the comparison between using cortical target masks and extended target masks, and for using probability density normalization. These are two novel techniques that were developed in this thesis. Overall, the topographic maps in the LGN and V5/MT were best predicted when using 0.5 mm steps (matching the voxel dimension), 0.0 curvature threshold, and a maximum permitted streamline length equating to 75% of the total brain length. The results showed that the maximum streamline length has a significant impact on topographic map accuracy. A maximum streamline length that is too short terminates streamlines before they reach the target, but allowing very long streamlines also reduces the accuracy of tractography, most likely due to the inclusion of spurious streamlines that loop around the brain implausibly. To the best of my knowledge, the finding that the maximum streamline length parameter is critical in topographic map prediction has not been reported previously in any of the probabilistic tractography literature. The results also indicated that the topographies of both LGN and V5/MT seed regions were best predicted when probability density normalization was applied. Although there is no significant difference when using extended target masks, on average, using extended masks resulted in a more qualitatively realistic match between the LGN and the atlas.

Following on from this work, I investigated the capability of DWI and probabilistic tractography in mapping topological connectivity between the LGN and V1 for visual elevation representations as well as for eccentricity representations, and across multiple *post mortem* brains. The results showed that these topological maps can be reliably predicted, and that the level of accuracy can be validated qualitatively and quantitatively. This is in large

part due to the high-resolution and high signal-to-noise ratio afforded by *post mortem* macaque preparations. However, using the methodology and techniques developed here, I also demonstrated that DWI and probabilistic tractography are sensitive and accurate enough to reveal ordered connectivity, not just within small subcortical regions (LGN), but also within weakly-connected sensory cortical regions (V5/MT), and for *in vivo* macaque datasets. Previous studies have successfully used diffusion tractography to parcellate the thalamus into regions purportedly corresponding to different nuclear groups (Behrens et al., 2003a), and also to parcellate the human amygdala into its distinct nuclear groups (Saygin et al., 2011). The results in the thesis are the first to show diffusion tractography can be used to make within-area segmentations based on connectivity, demonstrating a level of accuracy in diffusion tractography previously not thought possible. Indeed, the fact that this could be achieved *in vivo* was unexpected, but likely relies on the fact that the seed and target ROIs were defined first on the higher resolution *post mortem* images, and therefore with greater precision and confidence, before being registered onto the *in vivo* brains.

This thesis did not find evidence that DWI and probabilistic tractography were capable of mapping the same type of topological connectivity in human *in vivo* data. However, it is not currently clear whether this is because information about LGN to V1 topographical connectivity is not carried in the diffusion-imaging data, or because errors accumulated in the delineation of ROIs and the comparison of the predicted map to the atlas account for the poor validation measures. Further work in which regions of interest are defined retinotopically and with proton-density images, as well as diffusion-images collected at higher resolution, will be able to answer this question more concretely. A potential future study would be to collect diffusion-imaging data at 7T (affording higher SNR), on *in vivo* human subjects, along with population receptive field mapping of V1 (to functionally define the V1 targets) and high-resolution proton-density images (to define LGN). Using Human Connectome Project scan sequences, and scan sequences developed at Oxford's FMRIB, these scans could easily be obtained in a single session. This would then allow

the testing of whether *in vivo* human scans of approximately $1mm^3$ voxel resolutions are of sufficient quality to detect topographic organizations within cortical or subcortical areas. Based on the results in this thesis, the use of extended target masks and probability density normalization to account for inherent biases in tractography are recommended in any future implementations of tractography. Overall, the work in this thesis provides a benchmark for the *in vivo* clinical applications of DWI, and is an important step forward in the validation of DWI for *in vivo* work, and cross-species comparison work. The ability to perform probabilistic segmentation within areas raises new possibilities for the study of the brain in disease, for example, changes in the LGN have been observed in Alzheimer's disease, but not for dementia with Lewy bodies (Erskine et al., 2016). Reliably mapping structural connectivity also allows structure and function to be directly correlated within the same living human subjects (cf. Johansen-Berg et al., 2005).

The analyses presented in this thesis also have important implications for implementations of DWI that are aimed at investigating proposed pathways in the brain that have no 'gold standard' comparison. The results indicating that pathway accuracy is strongly affected by the maximum streamline length parameter mean that when investigating novel pathways, the expected length of the pathway should be considered and appropriately accounted for in the fibre-tracking algorithm. The centre of gravity analyses presented here also provide a useful approach for determining whether connectivity-labelled voxels in a seed region represent spatially distinct clusters in the absence of a gold standard atlas, and therefore whether a region contains structurally distinct subregions. The high-resolution *post mortem* datasets themselves exhibited in this thesis could also be beneficial for testing new analysis methods of DWI data, and for investigating novel pathways in other datasets. For example, given the high level of confidence in the pathways determined in this thesis it could be possible to implement a Bayesian inference-like approach in which voxels or pathways with a high level of connectivity as determined from these data are registered *a priori* onto a new set of data, in order to update the connectivity probability of pathways in an entirely new dataset. The potential for these kinds of approaches highlight the

flexibility and repeatability of DWI analyses, and this thesis offers a pathway to move from gold standard histology, to the exploration of new pathways *in vivo*.

In the latter part of this thesis, I developed and investigated a novel task-irrelevant perceptual learning paradigm designed to adapt neuronal elements early on in visual processing. Previous studies have reported direction specific task-irrelevant learning for motion-dot stimuli (e.g. Tsushima et al., 2008), while other studies have shown that the tuning properties of neurons in V1 change as a result of training on orientation discrimination tasks (e.g. Sasaki et al., 2010). However, few if any studies have explored the mechanisms of task-irrelevant learning by investigating TIPL in the early visual system. There is evidence from the task developed in this thesis, although not clear-cut, to suggest that the TIPL paradigm elicits task-irrelevant perceptual learning, but that these effects only emerge when practice-related effects are accounted for. When orientation and location specific effects on perceptual performance are examined, the largest improvement occurs at the trained location, however, there is also significant improvement at one other 'untrained' location, and there is also a significant improvement in performance for a control group that did not receive any training at any location. When trained stimuli were temporally paired with a reward, the location and orientation specific perceptual learning effects disappeared. However, it was not possible to conclude that this was due to the reward condition, as the difference in performance between rewarded and unrewarded conditions was not significant at any location. Even though a good number of subjects were included in the study, there was a high degree of individual variability, with subjects often showing a significant difference in their own performance between different visual field locations even before training. The inclusion of more subjects to account for the variability in subject performance is recommended in extensions of this study. The work highlights inherent difficulties in investigating perceptual learning, which relate to the fact that learning likely takes place at both lower and higher levels of processing.

Studies reporting that training on a specific stimulus feature does not transfer to other locations or to other stimulus features are usually taken to show that perceptual learning

has neural basis early on in sensory processing. However, this possibly reflects the bias in publishing studies that show non-transferable, specific effects, as any improvements in performance can easily be attributed to perceptual learning. Given that several studies have shown that perceptual improvements can be transferred or are generalizable, and that learning is affected by attention and reward, it is more likely that perceptual learning involves mechanisms occurring at both lower and higher levels of processing. Indeed, it makes sense that humans would have a range of mechanisms at their disposal for learning, but it makes investigating the mechanisms all the more complicated. Task-irrelevant perceptual learning paradigms offer a promising way of disentangling the effects of attention and reward from stimulus presentation effects; unfortunately the results presented in this thesis were not able to demonstrate clearly whether the behavioural improvements in orientation discrimination were the result of perceptual learning or more high-level order cognitive changes. While this likely due in large part to the low statistical power of the investigation, the notion that learning involves a range of mechanisms should not be overlooked. More work in this field is certainly needed to understand the neural mechanisms underlying perceptual learning, but the task-irrelevant perceptual learning paradigm developed here offers a promising avenue of investigation.

Appendix A

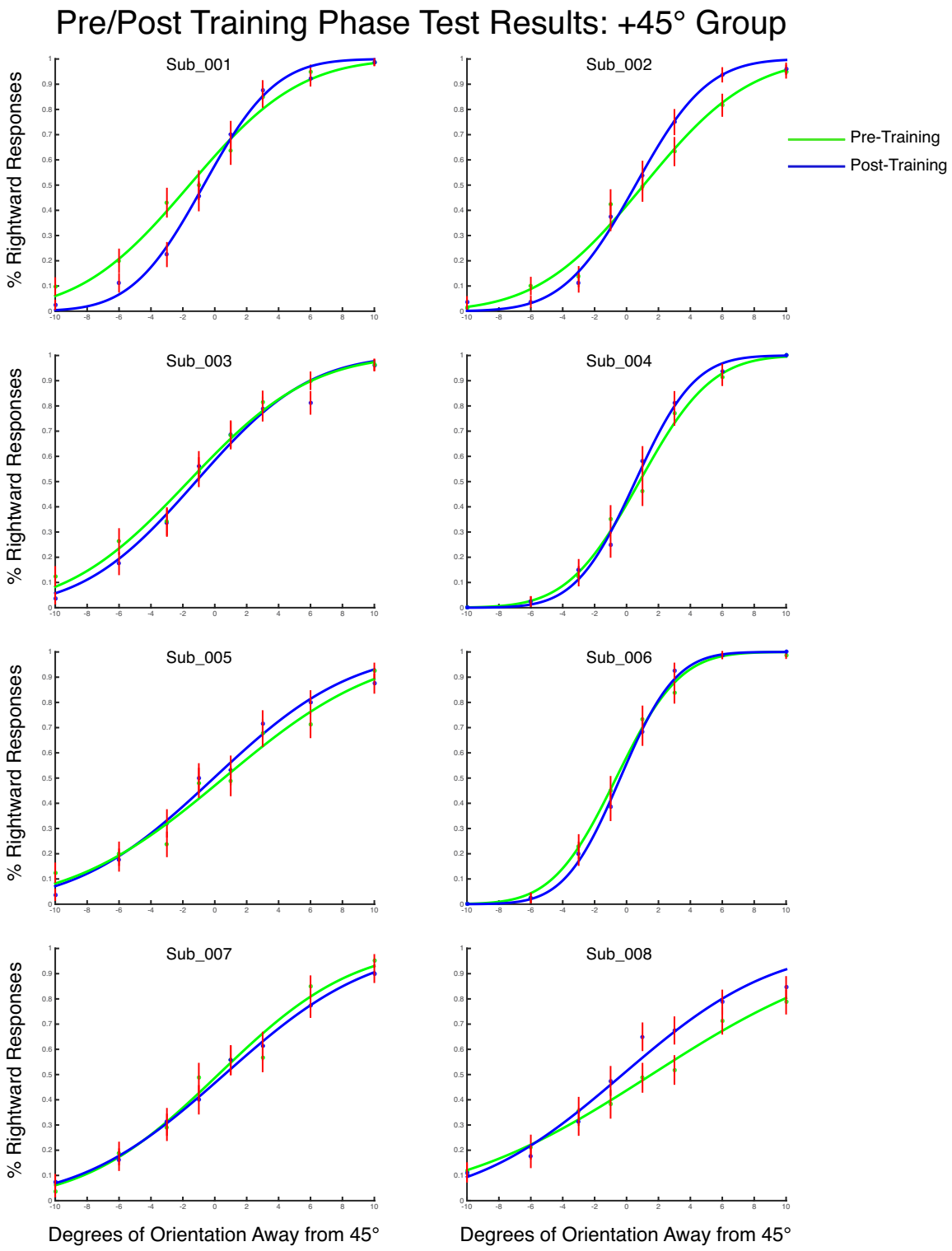
Pre/Post Training Phase Test Results: +45° Group
Sub_001
Sub_002
Sub_003
Sub_004
Sub_005
Sub_006
Sub_007
Sub_008
% Rightward Responses
Degrees of Orientation Away from 45°
Pre-Training
Post-Training

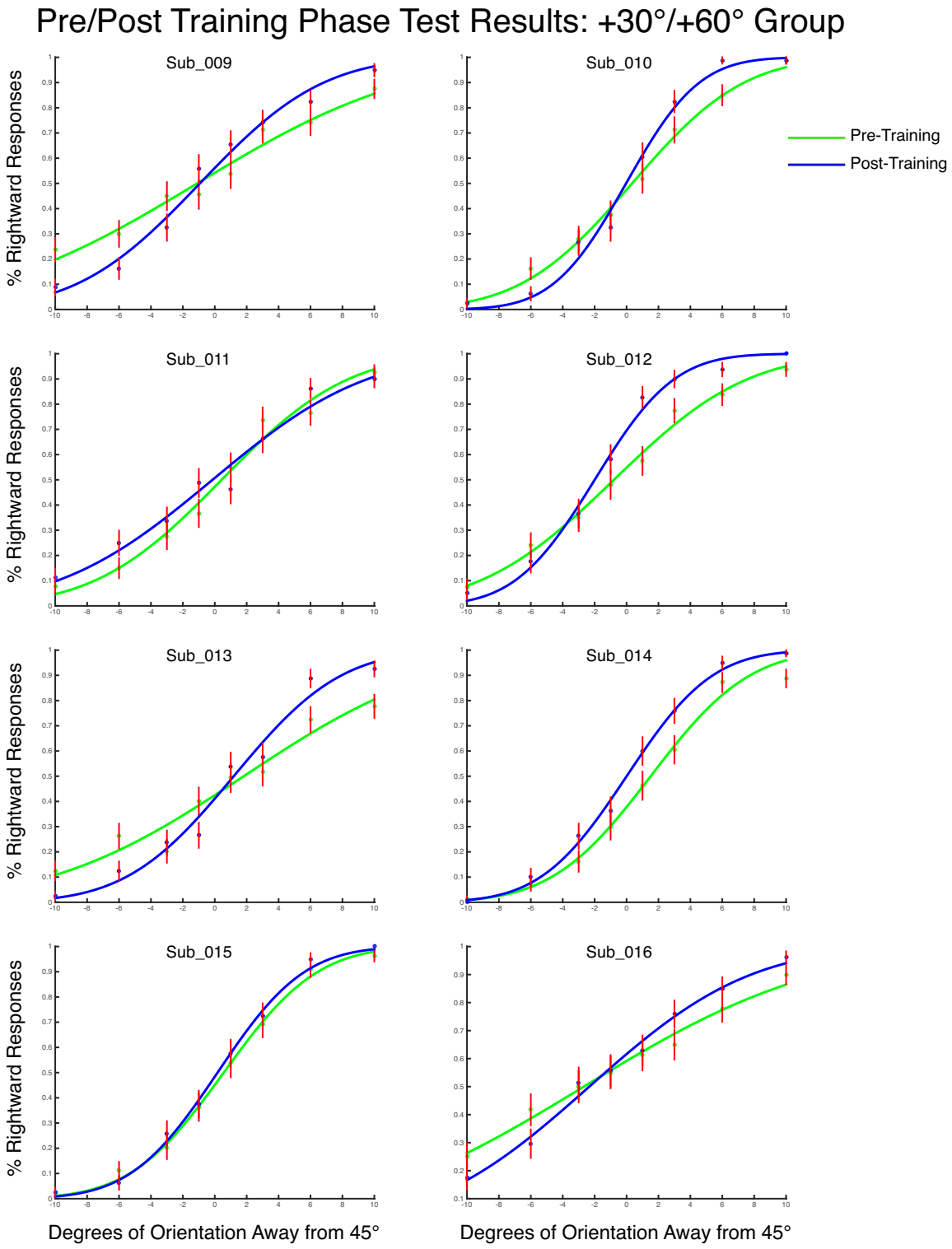
Pre/Post Training Phase Test Results: +30°/+60° Group
Sub_009
Sub_010
Sub_011
Sub_012
Sub_013
Sub_014
Sub_015
Sub_016
% Rightward Responses
Degrees of Orientation Away from 45°
Pre-Training
Post-Training

Pre/Post Training Phase Test Results: No Grating Control Group

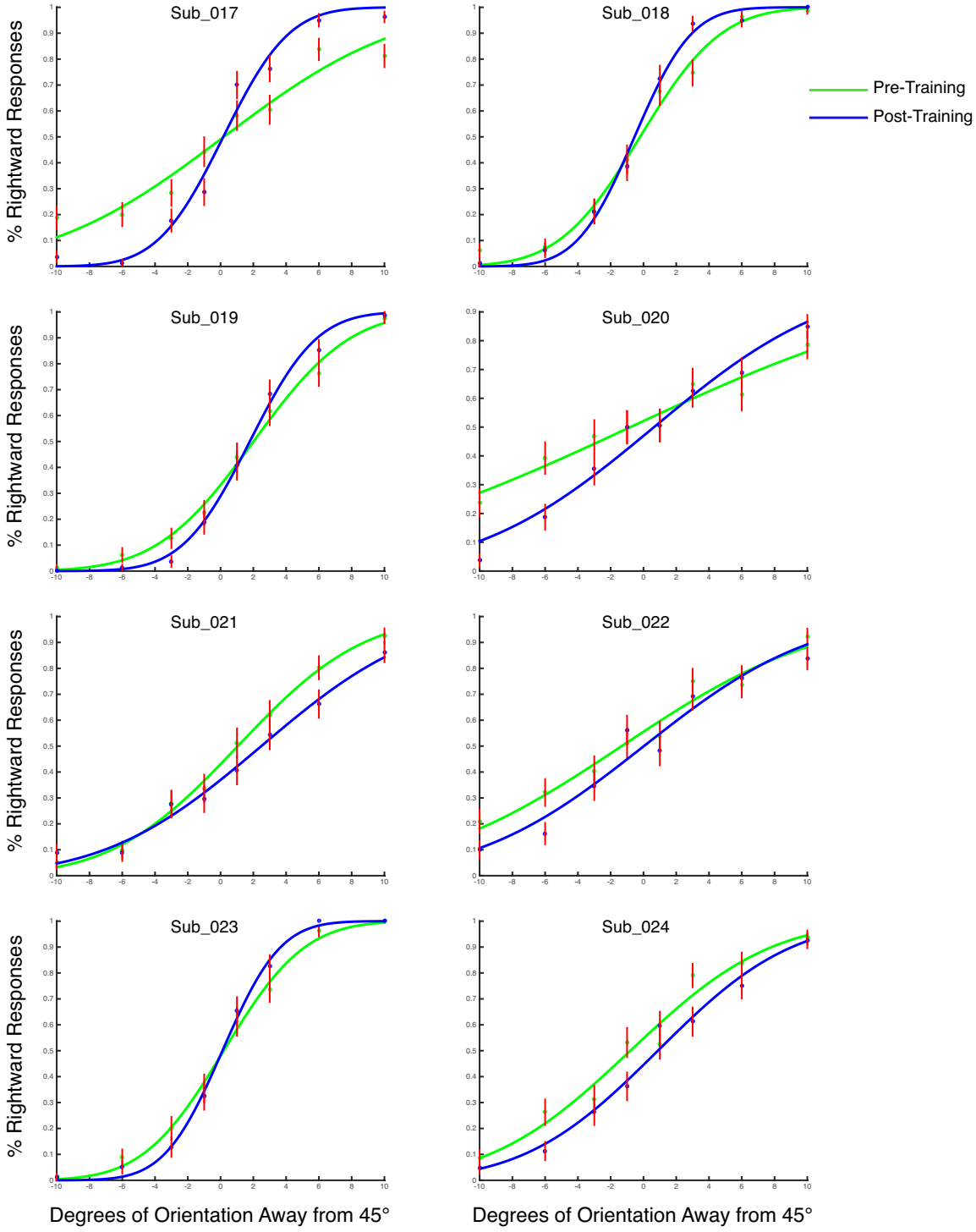

Appendix B

Orientation Discrimination Task Instructions

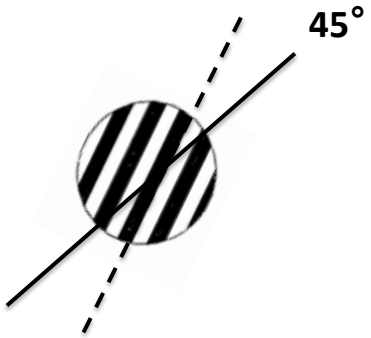

If grating orientation is to the **LEFT** of 45**°** (less than 45°) **= Press the LEFTARROW key.**

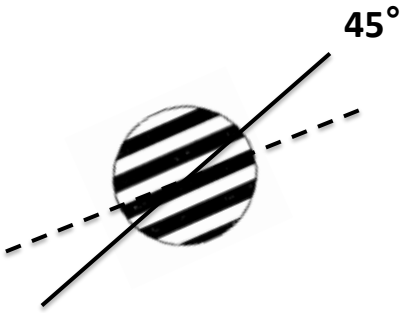

If grating orientation is to the **RIGHT** of 45**°** (more than 45°) **= Press the RIGHTARROW key.**

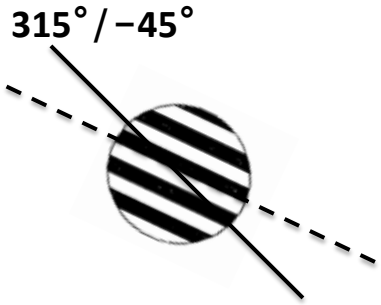

If grating orientation is to the **LEFT** of 315°/-45° (less than 315°/-45°) **= Press the LEFTARROW key.**

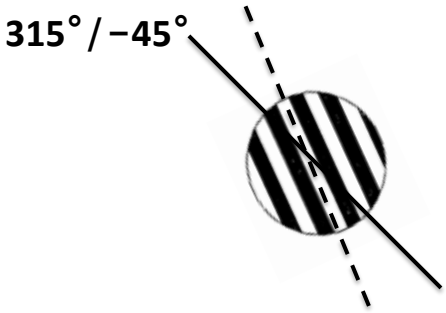

If grating orientation is to the **RIGHT** of 315°/-45° (less than 315°/-45°) **= Press the RIGHTARROW key.**

References

Adab, H. Z. and Vogels, R. (2011) Practicing coarse orientation discrimination improves orientation signals in macaque cortical area V4. *Curr. Biol., 21*, 1661-1666.

Adelson, E. H. and Movshon, J. A. (1982) Phenomenal coherence of moving visual patterns. *Nature, 300*, 523-525.

Adini, Y., Sagi, D. and Tsodyks, M. (2002) Context-enabled learning in the human visual system. *Nature, 415*, 790-793.

Ahissar, M. and Hochstein, S. (1993) Attentional control of early perceptual learning. *Proc. Natl. Acad. Sci. USA, 90*, 5718-5722.

Ahissar, M. and Hochstein, S. (1994) The reverse hierarchy theory of visual perceptual learning. *Trends Cogn. Sci., 8*, 457-464.

Ahmed, B., Cordery, P. M., McLelland, D., Bair, W. and Krug, K. (2012) Long-range clustered connections within extrastriate visual area V5/MT of the rhesus macaque. *Cereb. Cortex, 22*, 60-73.

Allman, J. M. and Kaas, J. H. (1971) A representation of the visual field in the caudal third of the middle temporal gyrus of the owl monkey. *Brain Res., 31*, 85-105.

Andersson, J. L. R., Skare, S. and Ashburner, J. (2003) How to correct susceptibility distortions in spin-echo echo-planar images: application to diffusion tensor imaging. *Neuroimage, 20*(2), 870-888.

Andersson, J. L. R., Jenkinson, M. and Smith, M. (2010) Non-linear registration aka spatial normalization: FMRIB technical report TR07JA2. Unpublished Technical Report.

Andrews, T. J., Halpern, S. D. and Purves, D. (1997) Correlated size variations in human visual cortex, lateral geniculate nucleus and optic tract. *J. Neurosci., 17*, 2859-2868.

Azzopardi, P. and Cowey, A. (1993) Preferential representation of the fovea in the primary visual cortex. *Nature, 361*, 719-720.

Azzopardi, P. and Cowey, A. (1996) The overrepresentation of the fovea and adjacent retina in the striate cortex and dorsal lateral geniculate nucleus of the macaque monkey. *Neuroscience, 72*, 627-639.

Azzopardi, P., Fallah, M., Regenbogen, S. E., Gross, C. G. and Rodman, H. R. (1999) Response latencies of neurons in cortical areas MT and MST in monkeys with striate cortex lesions. *Investigative Opthalmology and Visual Science, 40*, S640.

Baluch, F. and Itti, L. (2011) Mechanisms of top-down attention. *Trends Neurosci., 34*, 210-224.

Bao, S., Chan, V. T. and Merzenich, M. M. (2001) Cortical remodelling induced by activity of ventral tegmental dopamine neurons. *Nature, 412*(6842), 79-83.

Basser, P. J., Mattiello, J. and Le Bihan, D. (1994) Estimation of the effective self diffusion tensor from the NMR spin echo. *J. Magn. Reson. B., 103*(3), 247-254.

Basser, P. J., Pajevic, S., Pierpaoli, C., Duda, J., Aldroubi, A., (2000) In vivo fiber tractography using DT-MRI data. *Magn. Reson. Med., 4*, 625-632.

Behrens, T. E. J., Johansen-Berg, H., Woolrich, M. W., Smith, S. M. Wheeler-Kingshott, C. A. M., Boulby, P. A., Barker, G. J., Sillery, E. L., Shehan, K., Ciccarelli, O., Thompson, A. J., Brady, J. M., Matthews, P. M. (2003a) Non-invasive mapping of connections between human thalamus and cortex using diffusion imaging. *Nat. Neurosci., 6*(7), 750-757.

Behrens, T. E. J., Woolrich, M. W., Jenkinson, M., Johansen-Berg, H., Nunes, R. G., Clare, S., Matthews, P. M., Brady, J. M., Smith, S. M. (2003b) Characterization and propagation of uncertainty in diffusion-weighted MR imaging. *Magn. Reson. Med., 50*, 1077-1088.

Behrens, T. E. J., Johansen-Berg, H. J., Jbabdi, S., Rushworth, M. F., Woolrich, M. W. (2007) Probabilistic diffusion tractography with multiple fibre orientations: What can we gain? *Neuroimage, 34*, 144-155.

Behrens, T. E. J. and Jbabdi, S. (2009) MR diffusion tractography, in *Diffuion MRI*. 331-351. San Diego: Academic Press.

Beste, C., Wascher, E., Güntürkün, O., Dinse, H. R. (2011) Improvement and impairment of visually guided behaviour through LTP- and LTD-like exposure-based visual learning. *Curr. Biol., 21*, 876-882.

Beste, C., Wascher, E., Dinse, H. R. and Saft, C. (2012) Faster perceptual learning though excitotoxic neurodegeneration. *Curr. Biol., 22*, 1-4.

Blakemore, C. B. and Van Sluyters, R. E. (1947a) Reversal of the physiological effects of monocular deprivation in kittens; further evidence for a sensitive period. *J. Physiol., 237*, 195-216.

Blakemore, C. B. and Van Sluyters, R. E. (1947b) Experimental analysis of amblyopia and strabismus. *Br. J. Ophthal., 58*, 176-183.

Bliss, T. V. and Collingridge, G. L. (1993) A synaptic model of memory: long-term potentiation in the hippocampus. *Nature, 361*, 31-39.

Brainard, D. H. (1997) The psychophysics toolbox. *Spatial Vision, 10*, 433-436.

Buffalo, E. A., Fries, P., Landman, R., Liang, H. and Desimone, R. (2010) A backward progression of attentional effects in the ventral stream. *Proc. Natl. Acad. Sci. USA, 107*, 361-365.

Casagrande, V. A. (1994) A third parallel visual pathway to primate area V1. *Trends Neurosci., 17*, 305-310.

Casagrande, V. A. and Kaas, J. H. (1994) The afferent, intrinsic, and efferent connections of primary visual cortex in primates. In A. Peters & K. Rockland (Eds.), *Cereb. Cortex, 10*, 201-259. New York: Plenum Press.

Casagrande, V. A., Yazar, F., Jones, K. D. and Ding, Y. (2007) The morphology of the koniocellular axon pathway in the macaque monkey. *Cereb. Cortex, 17*, 2334-2345.

Catani, M. and Thiebaut de Schotten, M. (2008) A diffusion tensor imaging tractography atlas for in vivo dissections. *Cortex, 44*, 1105-1132.

Chelazzi, L., Perlato, A., Santandrea, E. and Della Libera, C. (2013) Rewards teach visual selective attention. *Vision Res., 85*, 58-72.

Chen, W., Zhu, X. H., Thulborn, K. R. and Ugurbil, K. (1999) Retinotopic mapping of lateral geniculate nucleus in humans using functional magnetic resonance imaging. *Proc. Natl. Acad. Sci. USA, 96*, 2430-2434.

Chen, C. and Regehr, W. G. (2003) Presynaptic modulation of the retinogeniculate synapse. *J. Neurosci., 23*, 3130-3125.

Chowdhury, S. A. and DeAngelis, G. C. (2008) Fine discrimination training alters the causal contribution of macaque area MT to depth perception. *Neuron, 60*, 367-77.

Conley, M. and Fitzpatrick, D. (1989) Morphology of retinogeniculate axons in the macaque. *Vis. Neurosci., 2*, 287-296.

Connolly, M., and Van Essen, D. C. (1984) The representation of the visual field in parvicellular and magnocellular laminae of the lateral geniculate nucleus in the macaque monkey. *J. Comp. Neural., 266*, 544-564.

Corbetta, M., Kincade, J. M., Ollinger, J. M., McAvoy, M. P. and Shulman, G. L. (2000) Voluntary orienting is dissociated from target detection in human posterior parietal cortex. *Nat. Neurosci., 3*, 292-297.

Côté, M. -A., Girard, G., Boré, A., Garyfallidis, E., Houde, J. -C., Descoteaux, M. (2013) Tractometer: towards validation of tractography pipelines. *Med. Image Anal., 17*, 844-857.

Coull, J. T., Frith, C. D., Frackowiak, R. S. J. and Grasby, P. M. (1996) A fronto-parietal network for rapid information processing: a PET study of sustained attention and working memory. *Neuropsychologia, 34*, 1085-1095.

Cowey, A. (1964) Projection of the retina on to striate prestriate cortex in the squirrel monkey, Saimiri sciureus. *J. Neurophysiol., 27*, 366-393.

Cowey, A. and Rolls, E. T. (1974) Human cortical magnification factor and its relation to visual acuity. *Exp. Brain Res., 21*, 447-454.

Cutzu, F. and Tsotsos, J. K. (2003) The selective tuning model of attention: psychophysical evidence for a suppressive annulus around an attended item. *Vision Res., 43*(2), 205-219.

Dalley, J. W., McGaughy, J., O'Connell, M. T., Cardinal, R. N., Levita, L. and Robbins, T. W. (2001) Distinct changes in cortical acetylcholine and noradrenaline efflux during contingent and noncontingent performance of a visual attentional task. *J Neurosci., 21*(13), 4908-14.

Daniel, P. M. and Whitteridge, D. (1961) The representation of the visual field on the cerebral cortex in monkeys. *J. Physiol., 159*, 203-221.

Davidson, M. C. and Marrocco, R. T. (2000) Local infusion of scopoplamine into intraparietal cortex slows cover orienting in rhesus monkeys. *J. Neurophysiol., 83*, 1536-49.

Delanoy, R. L., Tucci, D. L. and Gold, P. E. (1983) Amphetamine effects on long term potentiation in dentate granule cells. *Pharmacol. Biochem. Behav., 18*, 137-139.

Della Libera, C. and Chelazzi, L. (2006) Visual selective attention and the effects of monetary rewards. *Psychological Science, 17*, 222-227.

Denison, R. N., Vu., A. T., Yacoub, E., Feinberg, D. A. & Silver, M. A. (2014) Functional mapping of the magnocellular and parvocellular subdivisions of human LGN. *Neuroimage, 102*, 358-369.

DeSimone, K. K., Viviano, J. D. and Schneider, K. A. (2015) Population receptive field estimation reveals new retinotopic maps in human subcortex. *J. Neurosci., 35*(27), 9836-9847.

Dinse, H. R., Ragert, P. Pleger, B., Schwenkreis, P. and Tegenthoff, M. (2003) Pharmocological modulation of perceptual learning and associated cortical reorganization. *Science, 301*, 91-94.

Dosher, B. A. and Lu, Z. L. (1999) Mechanisms of perceptual learning. *Vision Res., 39*, 3197-3221.

Dosher, B. A. and Lu, Z. L. (2007) The functional form of performance improvements in perceptual learning: learning rates and transfer. *Psycho. Sci., 18*, 531-539.

Dougherty, D. M., Mathias, C. W., Marsh, D. M. and Jagar, A. A. (2005) Laboratory behavioural measures of impulsivity. *Behav. Res. Methods, 37*, 82-90.

Dow, B. M., Snyder, A. Z., Vautin, R. G. and Bauer, R. (1981) Magnification factor and receptive field size in foveal striate cortex of the monkey. *Exp. Brain. Res., 44*, 213-228.

Dubnet, R. and Zeki, S. M. (1971) Response properties and receptive fields of cells in an anatomically defined region of the superior temporal sulcus in the monkey. *Brain Res., 35*, 528-532.

Dyrby, T. B., Sogaard, L. V., Parker, G. J., Alexander, D. C., Lind, N. M., Baaré, W. F. C., Hay-Schmidt, A., Eriksen, N., Pakkenberg, B., Paulson, O. B. and Jelsing, J. (2007) Validation of in vitro probabilistic tractography. *Neuroimage, 37*, 1267-1277.

Dyrby, T. B., Baaré, W. F. C., Alexander, D. C., Jelsing, J., Garde, E., and Søgaard, L. V. (2011) An ex vivo imaging pipeline for producing high-quality and high-resolution diffusion-weighted imaging datasets. *Hum. Brain. Mapp., 32*, 544-563.

Efron, B. and Tibshirani, R. J. (1993) *An introduction to the bootstrap.* New York: Chapman & Hall.

Erwin, E., Baker, F. H., Busen, W. F. and Malpeli, J. G. (1999) Relationship between laminar topology and retinotopy in the rhesus lateral geniculate nucleus: results from a functional atlas. *J. Comp. Neurol., 407*, 92-102.

Fahle, M., Edelman, S. and Poggio, T. (1995) Fast perceptual learning in hyperacuity. *Vision Res., 35*(21), 3003-3013.

Felleman, D. J. and Van Essen, D. C. (1991) Distributed hierarchical processing in primate visual cortex. *Cereb. Cortex, 1*, 1-47.

Fiorentini, A. and Berardi, N. (1980) Perceptual learning specific for orientation and spatial frequency. *Nature, 287*(5777), 43-44.

Fishman, R. S. (1997) Gordon Holmes, the cortical retina, and the wounds of war. The seventh Charles B. Snyder Lecture. *Doc. Opthal-mol., 93*, 9-28.

Fitzpatrick, D., Lund, J. S. and Blasdel, G. G. (1985) Intrinsic connections of macaque striate cortex: afferent and efferent connections of lamina 4C. *J. Neurosci., 5*, 3329-3349.

Frey, S., Pandya, D. N., Chakravarty, M. M., Bailey, L., Petrides, M., Collins, D. L. (2011) An MRI based average macaque monkey stereotaxic atlas and space (MNI monkey space). *Neuroimage, 55*, 1435-1442.

Fries, W., Keizer, K., Kuypers, H. G. (1985) Large layer V1 cells in macaque striate cortex (Meynert cells) project to both superior colliculus and prestriate visual area V5. *Exp. Brain Res., 58*, 613-616.

Fujita, N., Tanaka, H., Takanashi, M., Hirabuki, N., Abe, K., Yoshimura, H., Nakamura, H. (2001) Lateral geniculate nucleus: anatomic and functional identification by use of MR imaging. *Am. J. Neuroradiol., 22*, 1719-1726.

Gallyas, F. (1979) Silver staining of myelin by means of a physical development. *Neurol. Res., 1*, 203-209.

Glasser, M. F. and Rilling, J. K. (2008) DTI tractography of the human brain's language pathways. *Cereb. Cortex, 18*, 2471-2482.

Glasser, M. F. and Van Essen, D. C. (2011) Mapping human cortical areas in vivo based on myelin content as revealed by T1 –and T2-weighted MRI. *J. Neurosci., 31*, 11597-11616.

Glasser, M. F., Sotiropoulos, S. N., Wilson, J. A., Coalson, T. S., Fischl, B., Andersson, J. L., Xu, J., Jbabdi, S., Webster, M., Polimeni, J. R., Van Essen, D. C., Jenkinson, M.; WU-Minn HCP Consortium. (2013) The minimal preprocessing pipelines for the Human Connectome Project. *Neuroimage, 80*, 105-124.

Glasser, M. F., Coalson, T. S., Robinson, E. C., Hacker, C. D., Harwell, J, Yacoub, E., Ugurbil, K., Andersson, J., Beckmann, C. F., Jenkinson, M., Smith, S. M. and Van Essen, D. C. (2016) A multi-modal parcellation of human cerebral cortex. *Nature, 536*(7615), 171-178.

Glimcher, P. W. and Rustichini, A. (2004) Neuroeconomics: the consilience of brain and decision. *Science, 306*(5695), 447-52.

Gold, J. I. and Shadlen, M. N. (2007) The Neural Basis of Decision Making. *Annu. Rev. Neurosci., 30*, 535-574.

Goldstone, R. L. (1998) Perceptual learning. *Annu. Rev. Psychol., 49*, 585-612.

Gordon, B., Allen, E. E. and Trombley, P. Q. (1988) The role of norepinephrine in plasticity of visual cortex. *Prog. Neurobiol., 30*, 171-191.

Grossberg, S. (1980) How does the brain build a cognitive code? *Psychological Review, 87*, 1-51.

Gur, M. Beylin, A., Snodderly, D. M. (1997) Response variability of neurons in primary visual cortex (V1) of alert monkeys. *J. Neurosci., 17*, 2914-2920.

Gutnisky, D. A., Hansen, B. J., Iliescu, B. F. and Dragoi, V. (2009) Attention alters visual plasticity during exposure-based learning. *Curr. Biol., 19*(7), 555-560.

Hampton, A. N., Bossaerts, P. and O'Doherty, J. P. (2008) Neural correlates of mentalizing-related computations during strategic interactions in humans. *Proc. Natl. Acad. Sci. USA, 105*, 6741-6746.

Hendry, S. H. C. and Yoshioka, T. (1994) A neurochemically distinct third channel in macaque dorsal lateral geniculate nucleus. *Science, 264*, 757-577.

Herzog, M. H. and Fahle, M. (1998) Modeling perceptual learning: Difficulties and how they can be overcome. *Biological Cybernatics, 78*, 107-117.

Herzog M. H. and Fahle, M. (1999) Effects of biased feedback on learning and deciding in a vernier discrimination task. *Vis. Res., 39*(25), 4232-4243.

Hickey, T. L. and Guillery, R. W. (1979) Variability of laminar patterns in the human lateral geniculate nucleus. *J. Comp. Neurol., 183*, 221-246.

Holmes, G. (1918) Disturbances of vision by cerebral lesions. *Bre. J. Opthal., 2*, 353-384.

Hopf, J-M., Boehler, C. N., Luck, S. J., Tsotsos, J. K., Heinze, H-J. and Schoenfeld, M. A. (2006a) Direct neurophysiological evidence for spatial suppression surrounding the focus of attention in vision. *Proc. Natl. Acad. Sci. USA, 103*, 1053-1058.

Hubel, D. H. and Wiesel, T. N. (1974) Uniformity of monkey striate cortex: a parallel relationship between field size, scatter, and magnification factor. *J. Comp. Neurol., 158*, 295-305.

Jbabdi, S. and Johansen-Berg, H. (2011) Tractography: where do we go from here? *Brain Connect, 1*, 169-183.

Jbabdi, S., Lehman, J. F., Haber, S. N. and Behrens, T. E. J. (2013) Human and monkey ventral prefrontal fibers use the same organizational principles to reach their targets: tracing versus tractography. *J. Neurosci., 33*(7), 3190-3201.

Jenkinson, M., Beckmann, C., Behrens, T., Woolrich, M. and Smith, S. (2012) FSL. *Neuroimage, 62*, 782-790.

Johansen-Berg, H. and Rushworth, M. F. (2009) Using diffusion imaging to study human connectional anatomy. *Annu. Rev. Neurosci., 32*, 75-94.

Jones, D. K., Horsfield, M. A. and Simmons, A. (1999) Optimal strategies for measuring diffusion in anisotropic systems by magnetic resonance imaging. *Magn. Reson. Med., 42*, 515-525.

Jones, D. K. (2010) *Diffusion MRI: theory, methods, and applications*. New York: Oxford University Press.

Jones, D. K., Knösche, T. R. and Turner, R. (2013) White matter integrity, fiber count, and other fallacies. The do's and don'ts of diffusion MRI. *Neuroimage, 73*, 239-254.

Kaas, J. H. (1997) Topographic maps are fundamental to sensory processing. *Brain Research Bulletin, 44*, 107-112.

Karni, A. and Sagi, D. (1991) Where practice makes perfect in texture discrimination: Evidence for primary visual cortex plasticity. *Proc. Nat. Acad. Sci. USA, 88*(11), 4966-4970.

Karni, A. and Sagi, D. (1993) The time course of learning a visual skill. *Nature, 365*, 250-252.

Kier, E. L., Staib, L. H., Davis, L. M. and Bronen, R. A. (2004) MR imaging of the temporal stem: anatomic dissection tractography of the uncinate fasciculus, inferior occipitofrontal fasciculus, and Meyer's loop of the optic radiation. *Am. J. Neuroradiol., 25*, 677-691.

Kilgard, M. P. and Merzenich, M. M. (1998a) Cortical map reorganization enabled by nucleus basalis activity. *Science, 279*, 1714-1718.

Knight, R. T., Grabowecky, M. F. and Scabini, D. (1995) Role of human prefrontal cortex in attention control. *Adv. Neurol., 66*, 21-34.

Knösche, T. R., Anwander, A., Liptrot, M. and Dyrby, T. B. (2015) Validation of tractography: comparison with manganese tracing. *Hum. Brain. Mapp., 36*(10), 4116-4134.

Kolster, H., Mandeville, J. B., Arsenault, J. T., Ekstrom, L. B., Wald, L. L. and Vanduffel, W. (2009) Visual field map clusters in macaque extrastriate visual cortex. *J. Neurosci., 29*, 7031-7039.

Kolster, H., Janssens, T., Orban, G. and Vanduffel, W. (2014) The retinotopic organization of macaque occipitotemporal cortex anterior to V5 and caudoventral to the middle temporal (MT) cluster. *J. Neurosci., 34*, 10168-10191.

Krug, K., Cumming, B. G. and Parker, A. J. (2004) Comparing perceptual signals of single V5/MT neurons in two binocular depth tasks. *J. Neurophysiol., 92*, 1586-1596.

Krug, K., Cicmil, N., Parker, A. J. and Cumming, B. G. (2013) A causal role for V5/MT neurons coding motion-disparity conjunctions in resolving perceptual ambiguity. *Curr. Biol., 23*, 1454-1459.

Kupfer, C. (1962) The projection of the macula in the lateral geniculate nucleus of man. *Am. J. Opthalmol., 54*, 597-609.

Large, I., Bridge, H., Ahmed, B., Clare, S., Kolasinski, J., Lam, W. W., Miller, K. L., Dyrby, T. B., Parker, A. J., Smith, J. E., Daubney, G., Sallet, J., Bell, A. H. and Krug,

K. (2016) Individual differences in the alignment of structural and functional markers of the V5/MT complex in primates. *Cereb. Cortex, 26*, 3928-3944.

Larsson, J. and Heeger, D. J. (2006) Two retinotopic visual areas in human lateral occipital cortex. *J. Neurosci., 26*, 13128-13142.

Law C. T. and Gold, J. I. (2008) Neural correlates of perceptual learning in a sensory-motor, but not a sensory, cortical area. *Nat. Neurosci., 11*, 505-513.

Le Bihan, D., Breton, E., Lallemand, D., Grenier, P., Cabanis, E. and Laval Jeantet, M. (1986) MR imaging of intravoxel incoherent motions: application to diffusion and perfusion in neurologic disorders. *Radiology, 161*, 401-407.

Le Bihan, D., Poupon, C., Amadon, A. and Lethimonnier, F. (2006) Artifacts and pitfalls in diffusion MRI. *J. Magn. Res. Imaging, 24*, 478-488.

Le Gros Clark, W. E. and Penman, G. G. (1933) The projection of the retina in the lateral geniculate body. *Proc. Roy. Soc., 114*, 291-313.

Liptrot, G., Sidaros, K. and Dyrby, T. (2014) Addressing the path-length dependency confound in white matter tract segmentation. *PLoS One*, 9:e96247.

Liu, F., Maggu, A. R., Lau, J. C. Y. and Wong, P. C. M. (2015) Brainstem encoding of speech and musical stimuli in congenital amusia: evidence from Cantonese speakers. *Front. Hum. Neurosci., 8*, 1029.

Livingstone, M. S. and Hubel, D. (1988) Segregation of form, color, movement and depth: anatomy, physiology, and perception. *Science, 240*, 740-749.

Lozsadi, D. A., Gonzalez-Soriano, J. and Guillery, R. W. (1996) The course and termination of corticothalamic fibres arising in the visual cortex of the rat. *Eur. J. Neurosci., 8*, 2416-2427.

Lu, Z. L. and Dosher, B. (1998) External noise distinguishes attention mechanisms. *Vision Res., 38*, 1183-1198.

Lund, J. S., Lund, R. D., Hendrickson, A. E., Bunt, A. H. and Fuchs, A. F. (1975) The origin of efferent pathways from the primary visual cortex (area 17) of the macaque monkey as shown by retrograde transport of horse-radish peroxidase. *J. Comp. Neurol., 164*, 287-304.

Mai, J. K., Paxinos, G. and Assheuer, J. (2004) *Atlas of the Human Brain, 2nd ed.* San Diego, CA: Academic Press.

Malpeli, J. G. and Baker, F. H. (1975) The representation of the visual field in the lateral geniculate nucleus of Macaca mulatta. *J. Comp. Neurol., 161*, 569-594.

Malpeli, J. G., Lee, D. and Baker, F. H. (1996) Laminar and retinotopic organization of the macaque lateral geniculate nucleus: magnocellular and parvocellular magnification functions. *J. Comp. Neurol., 375*, 363-377.

Markram, H., Gerstner, W. and Sjöström, P. J. (2011) A history of spike-timing-dependent plasticity. *Front. Synaptic Neurosci., 3*, 4.

Markov, N. T., Ercsey-Ravasz, M. M., Lamy, C., Ribeiro Gomes, A. R., Magrou, L., Misery, P., Giroud, P., Barone, P., Dehay, C., Toroczkai, Z., Knoblauch, K., Van Essen, D. C. and Kennedy, H. (2013) The role of long-range connections on the specificity of the macaque interareal cortical network. *Proc. Nat. Acad. Sci. USA, 110*, 5187-5192.

Marrocco, R. T., Witte, E. A. and Davidson, M. C. (1994) Arousal systems. *Curr. Opin. Neurobiol., 4*, 166-170.

Mars, R. B., Jbabdi, S., Sallet, J., O-Reilly, J. X., Croxson, P. L., Olivier, E., Noonan, M. P., Bergmann, C., Mitchell, A. S., Baxter, M. G., Behrens, T. E., Johansen-Berg, H., Tomassini, V., Miller, K. L. and Rushworth, M. F. (2011) Diffusion-weighted imaging

tractography-based parcellation of the human parietal cortex and comparison with human and macaque resting-state functional connectivity. *J. Neurosci, 31*, 4087-4100.

Mars, R. B., Sallet, J., Neubert, F. –X. and Rushworth, M. F. S. (2013) Connectivity profiles reveal the relationship between brain areas for social cognition in human and monkey temporoparietal cortex. *Proc. Natl. Acad. Sci. USA, 110*, 10806-10811.

Maunsell, J. H. R. and Van Essen, D. C. (1983c) The connections of the middle temporal visual area (MT) and their relationship to a cortical hierarchy in the macaque monkey. *J. Neurosci., 3*, 2563-2586.

Maunsell, J. H. and Van Essen, D. C. (1987) Topographic organization of the middle temporal visual area in the macaque monkey: representational biases and the relationship to callosal connections and myeloarchtectonic boundaries. *J. Comp. Neurol., 266*(4), 535-555.

McAdams, C. J. and Maunsell, J. H. R. (1999) Effects of attention on orientation-tuning functions of single neurons in macaque cortical area V4. *J. Neurosci., 19*(1), 431-441.

McAlonan, K., Cavanaugh, J. and Wurtz, R. H. (2008) Guarding the gateway to cortex with attention in visual thalamus. *Nature, 456*, 391-394.

McLaren, D. G., Kosmatka, K. J., Oakes, T. R., Kroenke, C. D., Kohama, S. G., Matochik, J. A., Ingram, D. K. and Johnson, S. C. (2008). A population-average MRI-based atlas collection of the rhesus macaque. *Neuroimage, 45*(1), 52-59.

McRobbie, D. W., Moore, E. A., Graves, M. J. and Prince, M. R. (2003) *MRI – from picture to proton.* New York: Cambridge University Press.

Merigan, W. H. and Maunsell, J. H. R. (1990) Macaque vision after magnocellular lateral geniculate lesions. *Vis. Neurosci., 5*, 347-352.

Michael, C. R. (1988) Retinal afferent arborisation patterns, dendritic field orientations, and the segregation of functional in the lateral geniculate nucleus of the monkey. *Proc. Natl. Acad. Sci. USA, 85*, 4914-4918.

Miller, K. L., McNab, J. A., Jbabdi, S. and Douaud, G. (2012) Diffusion tractography of post-mortem human brains: optimization and comparison of spin echo and steady-state free precession techniques. *Neuroimage, 59*, 2284-2297.

Molnar, A., Adams, R. and Blakemore, C. (1998a) Mechanisms underlying the establishment of topographically ordered early thalamocortical connections in the rat. *J. Neurosci., 18*, 5723-5745.

Mori, S., Crain, B. J., Chacko, V. P. and van Zijl, P. C. (1999) Three-dimensional tracking of axonal projections in the brain by magnetic resonance imaging. *Ann. Neurol., 45*(2), 265-269.

Morris, D. M., Embleton, K. V. and Parker, G. J. (2008) Probabilistic fibre tracking: differentiation of connections from chance events. *Neuroimage, 42*, 1329-1339.

Mounts, J. R. W. (2000a) Evidence for suppressive mechanisms in attentional selection: Feature singletons produce inhibitory surrounds. *Perception and Psychophysics, 62*(5), 969-983.

Mounts, J. R. W. (2000b) Attentional capture by abrupt onsets and feature singletons produces inhibitory surrounds. *Perception and Psychophysics, 62*(7), 1485-1493.

Movshon, J. A. and Newsome, W. T. (1984) Functional characteristics of striate cortical neurons projecting to MT in the macaque. *Soc. Neurosci. Abstr., 10*, 933.

Mukai, I., Bahadur, K., Kesavabhotla, K. and Ungerleider, L. G. (2011) Exogenous and endogenous attention during perceptual learning differentially affect post-training target thresholds. *Journal of Vision, 11*(1), 1-15.

Nagano-Saito, A., Leyton, M., Monchi, O., Goldberg, Y. K., He, Y. and Dagher, A. (2008) Dopamine depletion impairs frontostriatal functional connectivity during a set-shifting task. *J. Neurosci., 14*, 3697-3706.

Nealey, T. A. and Maunsell, J. H. R. (1994) Magnocellular and parvocellular contributions to the responses of neurons in macaque striate cortex. *J. Neurosci., 14*, 2069-2079.

Nelson, S. B. and LeVay, S. (1985) Topographic organization of the optic radiation of the cat. *J. Comp. Neurol., 240*, 322-330.

Neubert, F. –X., Mars, R. B., Thomas, A. G., Sallet, J. and Rushworth, M. F. S. (2014) Comparison of human ventral frontal cortex areas for cognitive control and language with areas in monkey frontal cortex. *Neuron, 81*, 700-713.

Newsome, W. T. and Wurtz, R. H. (1981) Response properties of single neurons in the middle temporal visual area (MT) of alert macaque monkeys. *Soc. Neurosci. Abstr., 7*, 832.

Nichols, T. E. and Holmes, A. P. (2002) Nonparametric permutation tests for functional neuroimaging: a primer with examples. *Hum. Brain Mapp., 15*, 1-25.

O'Connor, D. H., Fukui, M. M., Pinsk, M. A. and Kastner, S. (2002) Attention modulates responses in the human lateral geniculate nucleus. *Nat. Neurosci., 5*, 1203-1209.

Olney, J. W. (1994) New mechanisms of excitatory transmitter neurotoxicity neurodegeneration. *J. Neural Transm., 43*(43), 47-51.

Parizel, P. M., Rompaey, V. V., Loock, N., Hecke, W. V., Goethem, J. W. V., Leemans, A. and Sijbers. J. (2007) Influence of user-defined parameters on diffusion tensor tractography of the corticospinal tract. *J. Neuroradiology, 20*, 139-147.

Pelli, D. G. (1997) The VideoToolbox software for visual psychophysics: Transforming numbers into movies. *Spatial Vision, 10*, 437-442.

Perry, V. H., Oehler, R. and Cowey, A. (1984) Retinal ganglion cells that project to the dorsal lateral geniculate nucleus in the macaque monkey. *Neuroscience, 12*, 1101-1123.

Pessiglione, M., Petrovic, P., Daunizeau, J., Palminteri, S., Dolan, R. J., Frith, C. D. (2008) Subliminal instrumental conditioning demonstrated in the human brain. *Neuron, 59*(4), 561-567.

Petrov, A. A., Dosher, B. A. and Lu, Z. L. (2005) The dynamics of perceptual learning: an incremental reweighting model. *Psychol. Rev., 112*, 715-43.

Posner, M. I. and Petersen, S. E. (1990) The attentional system of the human brain. *Annu. Rev. Neurosci., 13*, 25-42.

Press, W. A., Brewer, A. A., Dougherty, R. F. Wade, A. R. and Wandell, B. A. (2001) Visual areas and spatial summation in human visual cortex. *Vision Res., 41*, 1321-1332.

Raiguel, S., Vogel, R., Mysore, S. G. and Orban, G. A. (2006) Learning to see the difference specifically alters the most informative V4 neurons. *J. Neurosci., 26*, 6589-6602.

Ramnani, N., Behrens, T. E., Johansen-Berg, H., Richter, M. C., Pinsk, M. A., Andersson, J. L., Rudebeck, P., Ciccarelli, O., Richter, W., Thompson, A. J., Gross, C. G., Robson, M. D., Kastner, S. and Matthews, P. M. (2006) The evolution of prefrontal inputs to the corticopontine system: diffusion imaging evidence from macaque monkeys and humans. *Cereb. Cortex, 16*, 811-818.

Reese, T., Weisskoff, R. and Wedeen, V. (2003) Reduction of eddy-current induced distortion in diffusion MRI using a twice-refocused spin echo. *Magn. Res. Med., 49*, 177-182.

Regan, D. and Beverly, K. I. (1983) Spatial-frequency discrimination and detection: comparison of postadaptation thresholds. *J. Opt. Soc. Am., 73*, 1684-1690.

Regan, D. and Beverly, K. I. (1985) Postadaption orientation discrimination. *J. Opt. Soc. Am., 2*, 147-155.

Rockland, K. S. (1989) Bistratified distribution of terminal arbors of individual axons projecting from area V1 to middle temporal area (MT) in the macaque monkey. *Vis. Neurosci., 3*, 155-170.

Rockland, K. S. (1995) The morphology of individual axons projecting from area V2 to MT in the macaque. *J. Comp. Neurol., 355*, 15-26.

Rolls, E. T. and Cowey, A. (1970) Topography of the retina and striate cortex and its relationship to visual acuity in rhesus monkeys and squirrel monkeys. *Exp. Brain Res., 10*, 298-310.

Rönne, H. (1910) Pathologisch-anatomische untersuchungen über alkoloische intoxikation-samblyopie. *Arch. Ophthalmol., 77*, 1-95.

Rönne, H. (1914) Die anatomische projektion der macula im corpus geniculatum. *Arch. Psychiatr. Nervenkr. Z. Gesamte. Neurol. Psychiatr., 22*, 469-485.

Rushworth, M. F. S., Behrens, T. and Johansen-Berg, H. (2006) Connection patterns distinguish three regions of the human parietal cortex. *Cereb. Cortex, 16*, 1418-1430.

Saenz, M. and Fine, I. (2010) Topographic organization of V1 projections through the corpus callosum in humans. *Neuroimage, 52*, 1224-1229.

Saleem, K. S. and Logothetis, N. K. (2007) *A combined MRI and histolohy atlas of the rhesus monkey brain in stereotaxic coordinates*. San Diego: Elsevier/Academic Press.

Sasaki, Y., Nanez, J.E and Watanabe, T. (2010) Advances in visual perceptual learning and plasticity. *Nat. Rev. Neurosci., 11*(1), 53-60.

Saygin, Z. M., Osher, D. E., Augustinack, J., Fischl, B. and Gabrieli, J. D. E. (2011) Connectivity-based segmentation of human amygdala nuclei using probabilistic tractography. *Neuroimage, 56*, 1353-1361.

Schien, S. J. and de Monasterio, F. M. (1987) Mapping of retinal and geniculate neurons onto striate cortex of macaque. *J. Neurosci., 7*, 996-1009.

Schluppeck, D., Glimcher, P. and Heeger, D. J. (2005) Topographic organization for delayed saccades in human posterior parietal cortex. *J. Neurophysiol., 94*, 1372-1384.

Schmahmann, J. D., Pandya, D. N., Wang, R., Dai, G., D'Arceuil, H. E., de Crespigny, A. J. et al. (2007) Association fibre pathways of the brain: parallel observations from diffusion spectrum imaging and autoradiography. *Brain, 130*, 630-653.

Schneider, K. A., Richter, M. C. and Kastner, S. (2004) Retinotopic organization and functional subdivisions of the human lateral geniculate nucleus: a high-resolution functional magnetic resonance imaging study. *J. Neurosci., 24*, 8975-8985.

Schoups, A. A., Vogels, R. and Orban, G. A. (1995) Human perceptual learning in identifying the oblique orientation: Retinotopy, orientation specificity and monocularity. *J. Physiol., 483*(3) 797-810.

Schoups, A., Vogels, R., Qian, N. and Orban, G. (2001) Practising orientation identification improves orientation coding in V1 neurons. *Nature, 412*, 549-553.

Schultz, W., Tremblay, L., and Hollerman, J. (2000) Reward processing in primate orbitofrontal cortex and basal ganglia. *Cereb. Cortex, 10*, 272-284.

Schwartz, E. L. (1977) Spatial mapping in the primate sensory projection: Analytic structure and relevance to perception. *Biol. Cybern., 25*, 181-194.

Schwartz, S., Maquet, P. and Frith, C. (2002) Neural correlates of perceptual learning: a functional MRI study of visual texture discrimination. *Proc. Natl. Acad. Sci. USA, 99*(26), 17137-42.

Seitz, A. R. and Watanabe, T. (2003) Is subliminal learning really passive? *Nature, 422*, 36.

Seitz, A. R., Nanez, J. E., Holloway, S. R., Koyama, S., and Watanabe, T. (2005a) Seeing what is not there shows the costs of perceptual learning. *Proc. Natl. Acad. Sci. USA, 102*(25), 9080-9085.

Seitz, A., Yamagashi, N., Werner, B., Goda, N., Kawato, M., Watanabe, T. (2005) Task-specific disruption of perceptual learning. *Proc. Nat. Acad. Sci. USA, 102*, 14895-14900.

Seitz, A. R. and Watanabe, T. (2009) The phenomenon of task-irrelevant perceptual learning. *Vision Res., 49*(21), 2604-2610.

Sereno, M. I., Pitzalis, S. and Martinez, A. (2001) Mapping of contralateral space in retinotopic coordinates by a parietal cortical area in humans. *Science, 294*, 1350-1354.

Shepherd, T., Thelwall, P. E., Stanisz, G. J. and Blackband, S. J. (2005) Chemical fixation alters the water microenvironment in rat cortical brain slices - implications for MRI contrast mechanisms. *Proc. Intl. Soc. Mag. Reson. Med., 13*, 619.

Shuler M. G. and Bear M. F. (2006) Reward timing in the primary visual cortex. *Science, 311*, 1606-1609.

Shiu, L. P. and Pashler, H. (1992) Improvement in line orientation discrimination is retinally local but dependent on cognitive set. *Perception and Psychophysics, 52*, 582-588.

Smith, S. M., Jenkinson, M., Woolrich, M. W., Beckmann, C. F., Behrens, T. E. J., Johansen-Berg, H., Banniester, P. R., De Luca, M., Drobnjak, I., Flitney, D. E., Niazy, R., Saunders, J., Vickers, J., Zhang, Y., De Stefano, N., Brady, J. M. and Matthews, P. M. (2004) Advances in functional and structural MR image analysis and implementation as FSL. *Neuroimage, 23*(1), 208-221.

Sotiropoulos, S. N., Jbabdi, S., Xu, J., Andersson, J. L., Moeller, S., Auerbach, E. J., Glasser, M. F., Hernandez, M., Sapiro, G., Jenkinson, M., Feinberg, D., Yacoub, E., Lenglet, C., Van Essen, D.C., Ugurbil, K., Behrens, T.E., - for the WU-Minn HCP Con-

sortium. (2013) Advances in diffusion MRI acquisition and processing in the Human Connectome Porject. *NeuroImage, 80*, 125-143.

Sotiropoulos, S.N., Moeller, S., Jbabdi, S., Xu, J., Andersson, J.L., Auerbach, E.J., Yacoub, E., Feinberg, D., Setsompop, K., Wald, L.L., Behrens, T.E., Ugurbil, K. and Lenglet, C. (2013d) Effects of image reconstruction on fiber orientation mapping from multichannel diffusion MRI: reducing the noise floor using SENSE. *Magn. Reson. Med., 70*, 1682–1689.

Stejskal, E. O. and Tanner, J. E. (1965) Spin diffusion measurements: spin echoes in the presence of time-dependent field gradient. *J. Chem. Phys., 42*, 288.

Stemmler, M., Usher, M. and Niebur, E. (1995) Lateral interaction in primary visual cortex: a model bridging physiology and psychophysics. *Science, 269*, 1887-1880.

Stensaas, S. S., Eddington, D. K., Dobelle, W. H. (1974) The topography and variability of the primary visual cortex in man. *J. Neurosurg., 40*, 755.

Stepniewska, I., Qi, H. X. and Kaas, J. H. (1999) Do superior colliculus projection zones in the inferior pulvinar project to MT in primates? *Eur. J. Neurosci., 11*(2), 469-480.

Steriade, M., Jones, E. G. and McCormick, D. A. (1997) *Thalamus*. Amsterdam: Elsevier.

Takemura, H., Caiafa, C. F., Wandell, B. A. and Pestilli, F. (2016) Ensemble tractography. *PLoS Comput. Biol., 12*(2), e1004692.

Talbot, S. and Marshall, W. (1941) Physiological studies on neural mechanisms of visual localization and discrimination. *Am. J. Opthal-mol., 24*, 1255-1263.

Thomas, C., Ye, F. Q., Irfanoglu, M. O., Modi, P., Saleem, K. S., Leopold, D. A. et al. (2014) Anatomical accuracy of brain connections derived from diffusion MRI tractography is inherently limited. *Proc. Natl. Acad. Sci. USA, 111*, 16574-16579.

Tournier, J. D., Calamante, F., King, M. D., Gadian, D. G. and Connelly, A. (2002) Limitations and requirements of diffusion tensor fiber tracking: an assessment using simulations. *Magn. Reson. Med., 474*, 701-708.

Tournier, J. D., Mori, S. and Leemans, A. (2011) Diffusion tensor imaging and beyond. *Magn. Reson. Med., 65*(6), 1532-1556.

Tsuchiya, N. and Koch, C. (2005) Continuous flash suppression reduces negative afterimages. *Nat. Neurosci., 8*(8), 1096-1101.

Tsushima, Y., Seitz, A. R. and Watanabe, T. (2008) Task-irrelevant learning occurs only when the irrelevant feature is weak. *Curr. Biol., 18*(12), 516-517.

Tuch, D. (2004) Q-ball imaging. *Magn. Reson. Med., 52*, 1358-1372.

Ugurbil, K., Xu, J., Auerbach, E. J., Moeller, S., Vu, A. T., Duarte-Carvajalino, J. M., Lenglet, C., Wu, X., Schmitter, S., van de Moortele, P. F., Strupp, J., Sapiro, G., de Martino, F., Wang, D., Harel, N., Garwood, M., Chen, L., Feinberg, D. A., Smith, S. M., Miller, K. L., Sotiropoulos, S. N., JBabdi, S., Andersson, J. L. R., Behrens, T. E. J., Glasser, M. F., van Essen, D. C. and Yacoub, E. (2013) Pushing spatial and temporal resolution for functional and diffusion MRI in the Human Connectome Project. *Neuroimage, 80*, 80-104.

Uka, T. and DeAngelis, G. C. (2006) Linking neural representation to function in stereoscopic depth perception: Roles of the middle temporal area in coarse versus fine disparity discrimination. *J. Neurosci., 26*, 6791-6802.

Umeda, K., Tanabe, S. and Fujita, I. (2007) Representation of stereoscopic depth based on relative disparity in macaque area V4. *J. Neurophysiol., 98*(1), 241-52.

Ungerleider, L. G. and Mishkin, M. (1979) The striate projection zone in the superior temporal sulcus Macaca mulatta: location and topographic organization. *J. Comp. Neurol., 188*, 347-466.

Usher, M., Cohen, J. D., Servan-Schreiber, D., Rajkowski, J. and Aston-Jones, G. (1999) The role of the locus coeruleus in the regulation of cognitive performance. *Science, 283*(5401), 549-54.

Van Essen, D. C., Maunsell, J. H. R. and Bixby, J. L. (1981) The middle temporal visual area in the macaque: myeloarchitecture, connections, functional properties and topographic organization. *J. Comp. Neurol., 199*, 292-326.

Van Essen, D. C., Newsome, W. T. and Maunsell, J. H. R. (1984) The visual field representation in striate cortex of the macaque monkey: Asymmetries, anisotropies, and individual variability. *Vision Res., 24*, 429-448.

Van Essen, D. C. (2013) Cartography and connectomes. *Neuron, 80*(3), 775-790.

Van Essen, D. C., Jbabdi, S., Sotiropoulos, S., Glasser, M. F. (2014) Mapping connections in humans and non-human primates: aspirations and challenges for diffusion imaging. In *Diffusion MRI, 2nd edition* (Eds. Johansen-Berg, H. & Behrens, T. E. J) 337-358 (Academic Press, 2014).

Wakana, S., Caprihan, A., Panzenboeck, M. M., Fallon, J. H., Perry, M., Gollub, R. L., Hua, K., Zhang, J., Jiang, H., Dubey, P., Blitz, A., van Zijl, P. and Mori, S. (2007) Reproducibility of quantitative tractography methods applied to cerebral white matter. *Neuroimage, 36*(3), 630-44.

Walker, L., Chang, L-C., Koay, C. G., Sharma, N., Cohen, L., Verma, R. and Pierpaoli, C. (2011) Effects of physiological noise in population analysis of diffusion tensor MRI data. *Neuroimage, 54*, 1168-1177.

Wandell, B. A., Dumoulin, S. O. and Brewer, A. A. (2007) Visual field maps in human cortex. *Neuron, 56*, 366-383.

Wang, R., Zhang, J. Y., Klein, S. A., Levi, D. M. and Yu, C. (2014) Vernier perceptual learning transfers to completely untrained retinal locations after double training: A "piggybacking" effect. *J. Vis., 14*(12), 1-10.

Wang, L., Mruczek, R. E. B., Arcaro, M. J. and Kastner, S. (2015) Probabilistic maps of visual topography in human cortex. *Cereb. Cortex, 25*, 3911-3931.

Watanabe, T., Nanez, J.E. and Sasaki, Y. (2001) Perceptual learning without perception. *Nature, 413*(6858), 844-848.

Watanabe, T., Nanez, J. E., Sr., Koyama, S., Mukai, I., Liederman, J., and Sasaki, Y. (2002) Greater plasticity in lower-level than higher-level visual motion processing in a passive perceptual learning task. *Nat. Neurosci., 5*(10), 1003-1009.

Westheimer, G. (1975) Visual acuity and hyperacuity. *Invest. Opthalmol., 14*, 570-572.

Wiesel, T. N. and Hubel D. H. (1963a) Effects of visual deprivation on morphology and physiology of cells in the cats lateral geniculate body. *Neurophysiol., 26*, 978-993.

Wiesel, T. N. and Hubel, D. H. (1963b) Single-cell responses in striate cortex of kittens deprived of vision in one eye. *Neurophysiol., 26*, 1003-1017.

Witte, E. A. and Marrocco, R. T. (1997) Alteration of brain noradrenergic activity in rhesus monkeys affects the alerting component of covert orienting. *Psychopharmacology (Berl), 132*, 315-323.

Woolrich, M. W., Jbabdi, S., Patenaude, B., Chappell, M., Makni, S., Behrens, T., Beckmann, C., Jenkinson, M. and Smith, S. M. (2009) Bayesian analysis of neuroimaging data in FSL. *Neuroimage, 45*, 173-186.

Xiao, L. Q., Zhang, J. Y., Wang, R., Klein, S. A., Levi, D. M. and Yu, C. (2008) Complete transfer of perceptual learning across retinal locations enabled by double training. *Curr. Biology, 18*(24), 1922-1926.

Yamamoto, A., Miki, Y., Urayama, S., Fushima, Y., Okada, T., Hanakawa, T. et al. (2007) Diffusion tensor fiber tractography of the optic radiation: analysis with 6-, 12-, 40-, and 80-directional motion-probing gradients, a preliminary study. *Am. J. Neuroradiol., 28*, 92-96.

Yang, T. and Maunsell, J. H. (2004) The effect of perceptual learning on neuronal responses in monkey visual area V4. *J. Neurosci., 24*, 1617-1626.

Zeki, S. (1976) The projections to the superior temporal sulcus from areas 17 and 18 in the rhesus monkey. *P. Roy. Soc. Lond. B., 193*, 199-207.

Zhang, P., Zhou, H., Wen, W. and He, S. (2015) Layer-specific response properties of the human lateral geniculate nucleus and superior colliculus. *Neuroimage, 111*, 159-166.